

AD-A089 064

SCRIPPS INSTITUTION OF OCEANOGRAPHY LA JOLLA CA

F/G B/7

ONE-CENTIMETER STRATIGRAPHY IN FORAMINIFERAL OOZE: THEORY AND P--ETC(U)

AUG 80 R F JOHNSON

N00014-75-C-0152

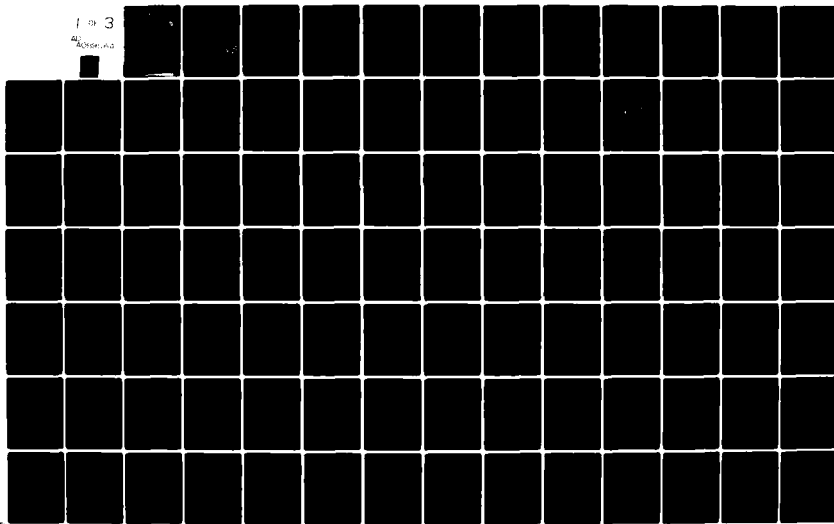
UNCLASSIFIED

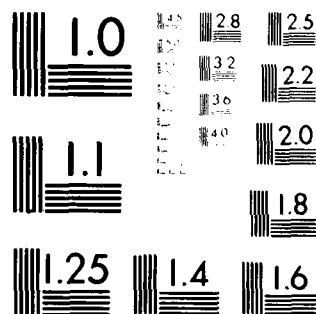
SIO-REF-80-18

NL

1 of 3

40
80000000





MICROCOPY RESOLUTION TEST CHART
NATIONAL BUREAU OF STANDARDS-1963-A

AD A089064

LEVEL

8

DTIC
SELECTED
SEP 11 1980

SIO REFERENCE SERIES

80-18

ONE-CENTIMETER STRATIGRAPHY IN FORAMINIFERAL OOZE:
THEORY AND PRACTICE

Richard Foster Johnson

This document has been approved
for public release and sale; its
distribution is unlimited.

University of California
7 August 1980

Scripps Institution of Oceanography
USN N00014-75-C-0152

unclassified

SECURITY CLASSIFICATION OF THIS PAGE (When Data Entered)

8

REPORT DOCUMENTATION PAGE		READ INSTRUCTIONS BEFORE COMPLETING FORM
1. REPORT NUMBER SIO Ref. 80-18	2. GOVT ACCESSION NO. AD-A089064	3. RECIPIENT'S CATALOG NUMBER
4. TITLE (and Subtitle) ONE-CENTIMETER STRATIGRAPHY IN FORAMINIFERAL OOZE: THEORY AND PRACTICE		5. TYPE OF REPORT & PERIOD COVERED
7. AUTHOR(s) Richard Foster Johnson		6. PERFORMING ORG. REPORT NUMBER SIO Ref. 80-18
9. PERFORMING ORGANIZATION NAME AND ADDRESS Scripps Institution of Oceanography La Jolla, CA 92093		8. CONTRACT OR GRANT NUMBER(s) N00014-75-C-0152
11. CONTROLLING OFFICE NAME AND ADDRESS Office of Naval Research Arlington, VA 22217		10. PROGRAM ELEMENT, PROJECT, TASK AREA & WORK UNIT NUMBERS
14. MONITORING AGENCY NAME & ADDRESS (if different from Controlling Office) LEVEL II		12. REPORT DATE August 7, 1980
		13. NUMBER OF PAGES 231
		15. SECURITY CLASS. (of this report) unclassified
		15a. DECLASSIFICATION/DOWNGRADING SCHEDULE
16. DISTRIBUTION STATEMENT (of this Report) Approved for public release: Distribution unlimited.		
17. DISTRIBUTION STATEMENT (of the abstract entered in Block 20, if different from Report)		
18. SUPPLEMENTARY NOTES		
19. KEY WORDS (Continue on reverse side if necessary and identify by block number)		
20. ABSTRACT (Continue on reverse side if necessary and identify by block number) The bug-bear of high-resolution stratigraphy in the deep sea is, sediment mixing by animals at the sea floor. Here we address several theoretical and practical problems in removing the effects of mixing. The objective of 1-cm stratigraphy is to recover a record of earth and ocean history more detailed than that known today. The research reported here concentrates on foraminiferal ooze, in which 1-cm of accumulation usually corresponds to an interval...		

DTIC
ELECTE
S

DD FORM 1473
1 JAN 73

EDITION OF 1 NOV 65 IS OBSOLETE
S/N 0102 LF 014 6601

SECURITY CLASSIFICATION OF THIS PAGE (When Data Entered)

MANADATORY DISTRIBUTION LIST
FOR UNCLASSIFIED TECHNICAL REPORTS, REPRINTS & FINAL REPORTS
PUBLISHED BY OCEANOGRAPHIC CONTRACTORS
OF THE OCEAN SCIENCE AND TECHNOLOGY DIVISION
OF THE OFFICE OF NAVAL RESEARCH
(Revised July 1978)

Department of Defense

Office of the Secretary of Defense (3)
Assistant Director of Defense Research
& Engineering
Washington, D.C. 20301

Naval Research Laboratory (6)
Library, Code 2620
Washington, D.C. 20375

U.S. Naval Oceanographic Office
Library, Code 8170
NSTL Station
Bay St. Louis, MS 39529

Navy

Office of Naval Research (3)
Code 460
Arlington, VA 22217

Office of Naval Research
Code 480
Arlington, VA 22217

Office of Naval Research
Code 102 B
Arlington, VA 22217

Office of Naval Research (6)
Code 102 DI
Arlington, VA 22217

Office of Naval Research
Commanding Officer
1030 East Green Street
Pasadena, CA 91101

Naval Ocean Research & Development
Activity
NORDA, Code 300
NSTL Station
Bay St. Louis, MS 39529

Other Government Agencies

Defense Documentation Center (12)
Cameron Station
Alexandria, VA 22314

National Oceanic & Atmospheric
Administration
National Oceanographic Data Center
Washington Navy Yard
Rockville, MD 20852

(14) SIO-REF-80-18

(8)

⑥ One-centimeter Stratigraphy in Foraminiferal Ooze:

Theory and Practice

by

(10) Richard Foster/Johnson

(11) 7 Aug 80

Sponsored by

(12) 2326
(15) Office of Naval Research
(USN N00014-75-C-0152)

University of California, San Diego
Scripps Institution of Oceanography
La Jolla, California 92093

7 August 1980
SIO Reference Number 80-18

(9) Doctoral thesis

Accession For	
NTIS	<input checked="" type="checkbox"/>
DDC 746	<input checked="" type="checkbox"/>
Unprocessed	<input type="checkbox"/>
Justification	
By	
Dist	
A	

This document has been approved
for public release and sale; its
distribution is unlimited.

A complete abstract of this report can
be found on pages iii thru v

319100

ABSTRACT

↓
The bug-bear of high-resolution stratigraphy in the deep sea is sediment mixing by animals at the sea floor. Here we address several theoretical and practical problems in removing the effects of mixing.

The objective of 1-cm stratigraphy is to recover a record of earth and ocean history more detailed than that known today. The research reported here concentrates on foraminiferal ooze, in which 1-cm of accumulation usually corresponds to an interval of less than 1000 yrs. In a later chapter, we try to construct a 1-cm stratigraphy of box cores of ooze from Ontong-Java Plateau.

The theory we use to reconstruct events recorded at 1-cm intervals has, in part, already been developed. It is based on Goldberg and Koide's model of a discrete sediment mixed layer. This report develops a number of useful formulas to account for the effects of dissolution, winnowing, fragmentation and horizontal sediment influx. The problem of finite mixing rates is also accommodated by a simplification of some results from Guinasso and Schink. Dating the reconstructed record with C^{14} is a matter of knowing contemporaneous mixed layer ages. In this light, this report describes a number of properties of mixed layer ages and the C^{14} record in general.

↑

One process unaccounted for in the Goldberg-Koide model is deep-burrowing. This report suggests a simple model of the effect of deep-burrowing on the ^{14}C record. With this we can presumably detect excessive deep-burrowing which would limit the validity of the formulas developed for reconstruction.

The practical problems of high-resolution stratigraphy are intimidating. In many cases, we need to improve measurement precision by a factor of ten or more.

For this and other reasons, I built a machine which can count, identify, and measure large numbers of foraminiferal shells automatically. The machine at present can identify 10 species of planktonic foraminifera at a rate of about 7000 shells per day. A key principle of design -- which makes programming new species easy -- is that errors in the machine's identifications are acceptable. Removing the effect of errors is merely a matter of calibration. In the identification programs so far written for planktonic foraminifera, the basic approach is one of fitting circles to shell outlines. This amounts to detecting chambers and characterizing the geometrical relationship between them.

This report tests both theory and machine on box cores from Ontong-Java Plateau. The machine performed reasonably well but it is clear that the theory cannot be applied blindly: Local effects such as slumps and erosion become more evident the more closely we look at a core.

The data from Ontong-Java Plateau also show: 1) that mixed layer thicknesses may be only 4-7 cm, 2) that mixing rates could be as low as 5 cm²/kyr, 3) that the Holocene rate of supply of fresh sediment over the plateau may exhibit a sharp change at about 2° latitude, 4) that Holocene dissolution of calcite appears to increase linearly with depth at a rate of about 1 cm/kyr/km, starting between 2500 and 3000 m, 5) that calcite dissolution at a given depth apparently decreased suddenly about 10000 yrs ago and increased again suddenly 2000-6000 yrs ago, 6) that productivity may have been low for at least 6000 yrs prior to 10000 yrs ago, at which point it may have increased sharply before settling back to its present value, and 7) that the flux of certain foraminiferal species and phenotypes appears to have changed suddenly about 8000 and 10000 yrs ago.

The conclusion is that 1-cm stratigraphy in foraminiferal ooze is feasible and worthwhile. The biggest stumbling blocks are local effects such as erosion and slumps.

Table of Contents

	page
Abstract	111
Table of Contents	vii
List of Figures	xi
List of Tables	xv
Acknowledgments	xvii
 Chapter 1: The Problem Posed by Sediment Mixing	 1
1. Statement of the problem	1
2. Importance of measurement precision	1
3. Thesis organization	3
 Chapter 2: Elaborations for Certain Complications	 5
1. The model	5
1.1 Mixing	5
1.2 Influx	9
1.3 Leaks	10
1.4 Conversion	11
2. Problem: reconstructing a non-radioactive signal	12
2.1 Solution	13
2.2 Discussion	16
2.2.1 Simple dissolution	17
2.2.2 Errors in the coefficient	19
3. Problem: dating mixed sediment	21
3.1 Solution	21
3.1.1 Age of the mixed layer	24
3.2 Discussion	25
3.2.1 Steady state	26
3.2.2 Age of material in leaks and horizontal influx	29
3.2.3 Non-steady state	31
4. Problem: effect of finite mixing rates	34
4.1 Solution	35
4.1.1 Guinasso and Schink's solution	35
4.1.2 Simplification	36
4.2 Discussion	38
5. Problem: testing for deep-burrows	41
5.1 Solution	41
6. Summary and conclusions	46
 Chapter 3: Sam, A Precision Stratigrapher	 49
1. Capabilities	49
2. How the hardware works	51
2.1 The framing mechanism	51
2.2 From image to digital intensities	55

3. How the software works	56
3.1 Control program	57
3.2 Analysis program	61
3.2.1 Chamber detection and circle-fitting	62
3.3 Identification program	63
4. Calibration	64
4.1 Method	64
4.2 Example: calibration for the Quaternary in the western equatorial Pacific	67
4.3 Holocene vs glacial calibration	69
4.4 Fragment calibration	72
5. Summary	73
 Chapter 4: Box Cores from Ontong-Java Plateau	 75
1. Introduction	75
2. Documented record of deglaciation	79
2.1 Global perspective	79
2.2 Documented record for the western equatorial Pacific	86
2.2.1 Climate and surface circulation today	86
2.2.2 Glacial climate and surface circulation	88
2.2.2.1 Evidence from land	88
2.2.2.2 Evidence from sea-floor sediment	93
2.2.2.3 Numerical simulations	95
2.2.3 Carbonate dissolution	96
2.3 Summary	99
3. Sedimentology of ERDC cores	100
3.1 Mixed layer thicknesses	101
3.2 Mixing rates	109
3.3 Sedimentation rates	110
3.3.1 s_0 from mixed layer ages	116
3.3.2 s_0 from eq (4.2)	129
3.3.3 Isochronal layers	138
3.3.4 Summary of sedimentation rates	140
4. ERDC box core stratigraphies	141
4.1 Methods and data	142
4.1.1 Sampling; grain size and carbonate analyses	142
4.1.2 Sam's data and performance	147
4.1.2.1 Sam's performance	158
4.2 Stratigraphy	161
4.2.1 The stratigraphy of dissolution	162
4.2.2 The stratigraphy of productivity	171
4.2.3 The stratigraphy of planktonic foraminifera	174
4.3 Conclusions from the stratigraphies	185
5. Summary of observations	187
 Chapter 5: Conclusions	 191

References	193
Appendix 1: Examples of Output from the Analysis Program	203
Appendix 2: Listing of Identification Program	211

LIST OF FIGURES

	page
Fig 2.1. A model of sedimentation of foraminiferal ooze based on Goldberg and Koide's (1962) concept of a discrete mixed layer	6
Fig 2.2. Nomograph of ^{14}C age of the mixed layer under certain additional assumptions	27
Fig 2.3. Proof than eq (2.10) is the impulse response of eq (2.14) and its initial conditions as $N \rightarrow \infty$	39
Fig 2.4. Result of using eq (1.1) on sediment mixed at finite rates when original unmixed input is a step function	40
Fig 2.5. Schematic diagram of a model of deep-burrowing	43
Fig 2.6. Hypothetical ^{14}C ages in the burrowed layer	45
Fig 2.7. Effect of deep-burrowing on mixed layer ages	47
Fig 3.1a. Side view of the framing mechanism	52
Fig 3.1b. Horizontal section through framing mechanism	53
Fig 3.2. Mirror geometry looking from the side with microscope to the right	54
Fig 3.3. Lighting arrangement, looking down	56
Fig 3.4. Flow of information	58
Fig 4.1a. Location of ERDC box cores	76
Fig 4.1b. Profiles of Ontong-Java Plateau	77
Fig 4.2. Four records of deglaciation	81
Fig 4.3. Zonal wind stress and 122 m subsurface temperatures at the equator at the longitude of Ontong-Java Plateau	87
Fig 4.4. Climate change on land in the tropical western Pacific	89
Fig 4.5. Low-resolution correlation of global climate and Ontong-Java's record of carbonate dissolution	97
Fig 4.6. Closely spaced ^{14}C dates for 3 ERDC cores	103

Fig 4.7. Coarse fraction in ERDC 128	107
Fig 4.8. Weight percent carbonate in the ERDC cores	108
Fig 4.9. Goldberg-Koide (1962) model of the mixed layer of ERDC 79	111
Fig 4.10. s_0 vs latitude, from mixed layer ages and eq (2.8c)	118
Fig 4.11. $s-s_0$ for the ERDC cores	128
Fig 4.12. Calculated Holocene dissolution loss vs depth at core site for the ERDC box cores	132
Fig 4.13. Calculated s_0 vs latitude, using dissolution loss from carbonate percentages and reported accumulation rates	134
Fig 4.14. ^{14}C signatures of isochronal layers of various origins	139
Fig 4.15. Comparison of grain size analyses for ERDC 79 done with two methods of disaggregation: ultrasonication and H_2O_2	143
Fig 4.16. Comparison of carbonate measurements on ERDC 79 by two different technicians at widely separated times	145
Fig 4.17. Grain size and carbonate analyses for ERDC 79	146
Fig 4.18a. Calibrated abundance of <u>G. menardii</u> and <u>P. obliquiloculata</u> in ERDC 79	149
Fig 4.18b. Calibrated abundance of <u>G. menardii</u> and <u>P. obliquiloculata</u> in ERDC 83	149
Fig 4.18c. Calibrated abundance of <u>G. dutertrei</u> and <u>G. tumida</u> in ERDC 79	149
Fig 4.18d. Calibrated abundance of <u>G. dutertrei</u> and <u>G. tumida</u> in ERDC 83	149
Fig 4.18e. Calibrated abundance of <u>G. conglomerata</u> in ERDC 79	151
Fig 4.18f. Calibrated abundance of <u>G. conglomerata</u> in ERDC 83	151
Fig 4.18g. Calibrated abundance of cold group and both phenotypes of <u>G. sacculifer</u> in ERDC 79	151
Fig 4.18h. Calibrated abundance of cold group and both	

phenotypes of <u>G. sacculifer</u> in ERDC 83	151
Fig 4.18i. Calibrated abundance of <u>G. sacculifer trilobus</u> and <u>G. sacculifer sacculifer</u> in ERDC 79	153
Fig 4.18j. Calibrated abundance of <u>G. sacculifer trilobus</u> and <u>G. sacculifer sacculifer</u> in ERDC 83	153
Fig 4.18k. Calibrated mean diameter of <u>P. obliquiloculata</u> , calibrated max diameter of <u>G. sacculifer trilobus</u> , and calibrated mean diameter of <u>G. menardii</u> in in ERDC 79	153
Fig 4.18l. Calibrated mean diameter of <u>P. obliquiloculata</u> , calibrated max diameter of <u>G. sacculifer trilobus</u> , and calibrated mean diameter of <u>G. menardii</u> in in ERDC 83	153
Fig 4.18m. Measured and calibrated fragment abundance in ERDC 79	155
Fig 4.18n. Measured and calibrated fragment abundance in ERDC 83	155
Fig 4.18o. Measured abundance of <u>G. aequilateralis</u> and ratio of radii of ultimate and penultimate chambers in kummerform <u>G. aequilateralis</u> in ERDC 79	155
Fig 4.18p. Measured abundance of <u>G. aequilateralis</u> and ratio of radii of ultimate and penultimate chambers in kummerform <u>G. aequilateralis</u> in ERDC 83	155
Fig 4.18q. Calibrated abundance of the normal form and kummerform of <u>G. aequilateralis</u> in ERDC 79	157
Fig 4.18r. Measured and calibrated number of chambers in the outline of <u>G. dutertrei</u> in ERDC 79	157
Fig 4.18s. Calibrated mean diameter of <u>O. universa</u> and calibrated mean diameter of the penultimate chamber of <u>G. sacculifer trilobus</u> in ERDC 79	157
Fig 4.19. Second interpretation of the near surface ¹⁴ C profile of ERDC 123	170
Fig 4.20. Variation of carrier fraction for species abundances in Fig 4.18	176
Fig 4.21. Reconstruction of the abundances of <u>P. obliquiloculata</u> and <u>G. menardii</u> in the interval 20-28 cm in ERDC 79	177
Fig 4.22. Like Fig 4.21, except for ERDC 83	178

Fig A1.1. Sample output from Sam for "species" 1-4	206
Fig A1.2. Sample output from Sam for "species" 5-8	208
Fig A1.3. Sample output from Sam for "species" 9-13	210

LIST OF TABLES

	page
Table 2.1. Fallout pattern of suspended particles in 5 cm/sec current	10
Table 2.2. Examples of signals and carriers	13
Table 3.1a. Species names, codes and abbreviations	64
Table 3.1b. Species currently identified by Sam and their distinctions	65
Table 3.2. Table of p_{ij} and their confidence limits for ERDC 79	68
Table 3.3. Example of measurement weights, a_{ij}	70
Table 3.4. Difference between the p_{ij} from ERDC 79, 4-5 cm, and the p_{ij} from ERDC 79, 33-34 cm	71
Table 3.5. Fragment calibration	73
Table 4.1. Data used to determine sedimentation rates for the ERDC cores	114
Table 4.2. Horizontal influx to the shallow ERDC cores	126
Table 4.3. Effect of winnowing on carbonate fractions	136
Table 4.4. Expected fragment change in ERDC 83 with no change in dissolution	165
Table 4.5. "Fluxes" of five important species in the fraction 355-840 μ	183

ACKNOWLEDGMENTS

This report is a copy of my doctoral thesis. Grants to Wolfgang H. Berger from the Office of Naval Research supported most of the work. I am grateful to ONR for this.

Furthermore, I thank Wolfgang H. Berger for making these funds available, and for samples, data, advice, and encouragement. As you will see by the number of references to his papers, many of his ideas form the framework for the report.

Next, I thank my doctoral committee for a close reading. In particular, I am grateful to Richard A. Haubrich for checking the formulas in Chapter 2, to Joseph L. Reid for providing advice and references, and to Hans R. Thierstein for many constructive criticisms of Chapter 4.

Three members of the SIO staff played key roles in developing the machine described in Chapter 3: Ronald T. LaBorde provided and maintained the minicomputer system which runs the machine; Phillip R. Mack offered encouragement and gave guidance in mechanical design; he also made a number of precision parts. David Wirth acted as godfather, giving material support and counsel. To these three men I am especially grateful.

Marvin G. Gebhardt at the upper campus machine shop did most of the machining. I thank him for a fine job.

Chapter 4 owes much to the efforts of several people. Jean Hanscom painstakingly prepared the samples from ERDC 79 and did

grain size analysis. Steven L. Vierra (whose services were kindly lent by Edith Vincent) also did grain size and carbonate analysis. David L. Ripley supervised many of the measurements of the other ERDC cores. My thanks to these individuals for their meticulous work. Thomas J. Walsh provided useful suggestions and ready access to ERDC material. Likewise, Stuart M. Smith and his group helpfully made available underway data.

In addition, I thank John S. Killingley for discussions on paleo-oceanography and for his support and assistance. For other technical discussions, I thank Helmut Erlenheuser, Edward D. Goldberg, Minoru Koide, Gary A. Meyers, Frances L. Parker, Mizuki Tsuchiya, and James A. Zampol.

Finally, I thank the UCSD Computer Center for making the CATT system available for theses; I thank Michiko Hitchcox for explaining it to me. Thanks also to Elizabeth S. Stover for a variety of help over the years.

CHAPTER 1

THE PROBLEM POSED BY SEDIMENT MIXING

1. Statement of the problem

Foraminiferal ooze results from a more or less steady accumulation of small shells. As such, it provides a faithful record of earth and ocean history (Schott, 1935; Cushman and Henbest, 1941; Phleger, 1942; Arrhenius, 1952; Emiliani, 1955). Close examination, however, shows that the ooze does not accumulate shell on top of shell. On the contrary, processes at the seafloor continually mix fresh material into deeper levels (Bramlette and Bradley, 1941).

An unanswered question -- which we address in this report -- is whether or not it is possible to resolve the historical record at intervals smaller than the time constant of the mixing (Ruddiman et al., 1976; Peng et al., 1977; Berger et al., 1977a). Success depends upon

- 1) an understanding of sedimentation and the mixing process, and
- 2) development of measuring instruments of high precision.

Most previous effort has been towards 1). The research described here tries to add to 1) but emphasizes 2).

2. Importance of measurement precision

To appreciate how critical measurement precision is, consider the difficulty of monitoring events which theoretically can be resolved at 1 cm intervals: Let $c = c(z)$ be measurements made down core at depths-in-core z . (For instance, c might be the abundance of a given species of shell, the calcium carbonate percentage of the bulk material,

or the $\delta^{18}\text{O}$ of a particular species). Let c_0 be the value of this parameter had there been no mixing. We have shown earlier (Berger et al., 1977a) that under the simplest conditions of mixing,

$$c_0 = c + Z \frac{dc}{dz}, \quad (1.1)$$

where in the deep sea Z may be 4 to 8 cm or more (Berger and Johnson, 1978; and others, see Chapters 2 and 4, below). We assume here that this equation holds and that we know Z . In terms of finite differences for two points at $z = z_1$ and $z = z_2$,

$$\begin{aligned} c_0 &= c_1 + Z \frac{c_1 - c_2}{z_1 - z_2} \\ &= (Z/\Delta z + 1)c_1 - (Z/\Delta z)c_2, \end{aligned}$$

where $c_1 = c(z_1)$ and $c_2 = c(z_2)$, and $\Delta z = z_1 - z_2$.

Now suppose that the measurements, c_1 and c_2 , have associated with them a random error with variance, $\text{var}[c] = \sigma^2$. Then, if the errors in c_1 and c_2 are independent of each other, the consequent variance, σ_0^2 , in the calculated value, c_0 , follows from the finite difference equation:

$$\begin{aligned} \sigma_0^2 &\equiv \text{var}[c_0] = \text{var}[(Z/\Delta z + 1)c_1] + \text{var}[(Z/\Delta z)c_2] \\ &= (Z/\Delta z + 1)^2 \text{var}[c_1] + (Z/\Delta z)^2 \text{var}[c_2] \\ &= \left[\frac{2Z^2}{\Delta z^2} + \frac{2Z}{\Delta z} + 1 \right] \sigma^2 \end{aligned}$$

For $\Delta z = 1$ cm and $Z = 8$ cm, this becomes

$$\sigma_0^2 = 145\sigma^2.$$

We may reduce the variance in the estimate of c_0 by repeating the measurements of c . If the mean of such replicates is the best estimate of c , then to reduce σ_0 to the same order as σ requires 145 replicates. As an alternative, we can build a new instrument which has an rms error $\frac{1}{12}$ of the old.

What I have done in the research described here is in effect that: I have built a machine which can count and measure the various species of planktonic foraminifera automatically. Its precision (but not necessarily its accuracy) is limited only by counting statistics.

For instance, take the case above where $Z = 8$ cm. Let the machine count 43,500 specimens for each cm down a perfect core. Now reconstruct the abundance of some species by means of eq (1.1). The result is a reconstruction which would be equivalent, theoretically, to the history seen by a very ancient and long-lived micropaleontologist who has counted 300 specimens from a perfect sediment trap raised once every 500 or so years.

3. Report organization

That the machine and theory can in fact replace this long-lived archivist is an open question:

First of all, sedimentation in the deep sea is known to be more complicated than that implicit in eq (1.1). Chapter 2 discusses some of the known complications and how to correct for them.

Second, the machine itself is rather imperfect. Chapter 3 describes the machine in some detail.

And finally, there may be processes at work of which we know little or nothing. For this reason, Chapter 4 will test both machine and present understanding on box cores from Ontong-Java Plateau sampled at 1 cm intervals.

CHAPTER 2

ELABORATIONS FOR CERTAIN COMPLICATIONS

1. The Model

This chapter elaborates on eq (1.1). It develops additional formulas for reconstructing the original signal from the mixed one. Our basic model is that of Goldberg and Koide (1962) as simplified by Berger and Heath (1968). Peng et al. (1977) were the first to attempt a complete reconstruction with this basic model. The present chapter includes the effects of time-varying dissolution, winnowing and fragmentation. It also suggests a simple way to date a mixed signal using a clock such as ^{14}C . Final sections of the chapter discuss the effects of finite mixing rates and deep burrowing.

Figure 2.1 shows the model we will use. The model works like this: particles fall to the seafloor and are mixed with older sediment. At the same time, certain amounts and certain kinds of this mixed surficial sediment leak away due to winnowing and dissolution. Likewise, some of the mixed material also continuously converts from one form to another, as in fragmentation. Eventually, as more sediment accumulates, the bottom of the mixed layer moves upward and leaves an output deposit which we exploit for its historical record.

1.1. Mixing

For purposes of high-resolution stratigraphy, the central feature of this model is the mixing. Goldberg and Koide (1962) were the first to guess and demonstrate that mixing on the deep-sea floor might

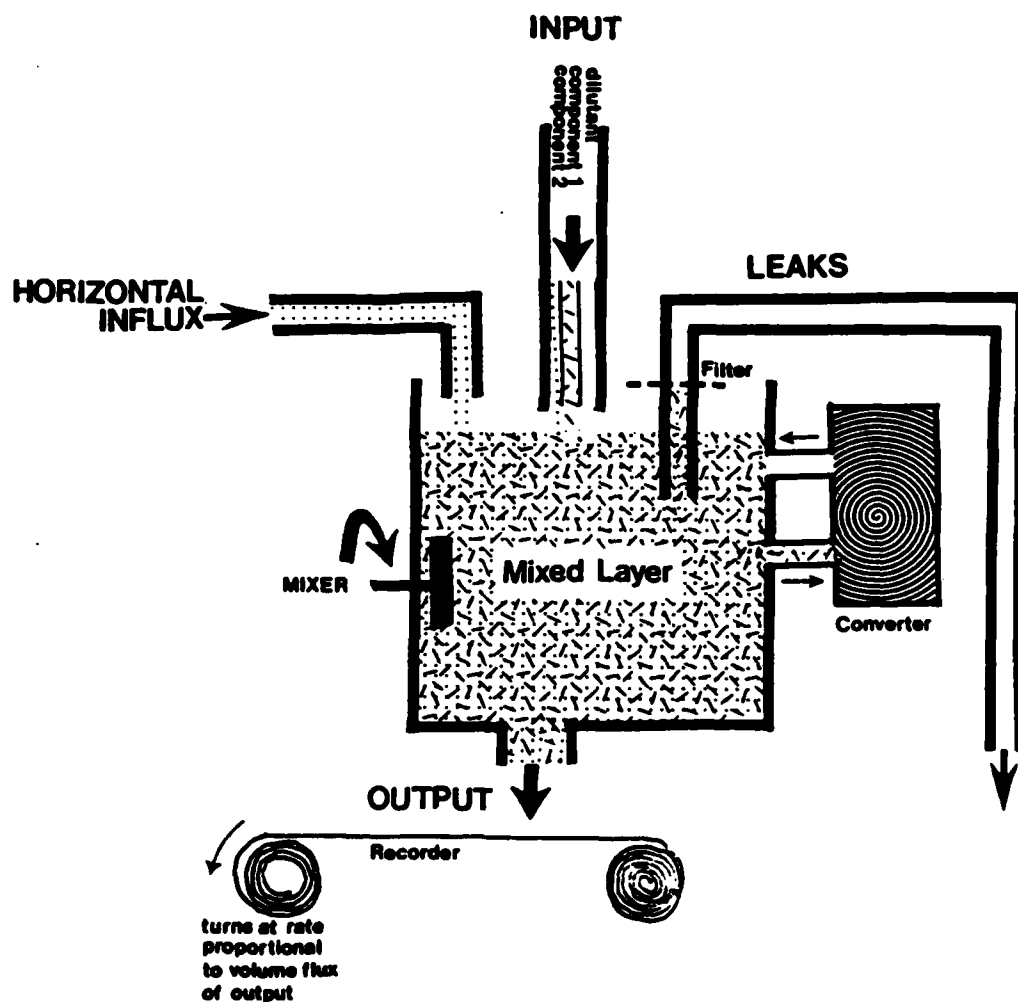


Fig 2.1. A model of the sedimentation of foraminiferal ooze based on Goldberg and Koide's (1962) concept of a discrete mixed layer. In cores of sediment, we see a record of the output. This chapter discusses how to reconstruct the input from the output. In Goldberg and Koide's model, the mixers, shown here as a single blade, work with equal vigor at all levels.

be confined to a discrete layer at the surface of the sediment. Recent data, some of which will appear Chapter 4, has confirmed that such a discrete layer exists in many areas of the deep sea (Peng et al., 1977;

Nozaki et al., 1977; Berger and Johnson, 1978; Williams et al., 1978; Cochran, 1979; DeMaster, 1979; Peng et al., 1979; Krishnamurthy et al., in press).

The cause of mixing in deep-sea sediment is not as yet clear. Early workers blamed large animals (Bramlette and Bradley, 1941; Arrhenius, 1963; Laughton, 1963; and others); some workers still do (Paul, 1977; DeMaster, 1979). Goldberg and Koide (1962) did not rule out bottom currents. However, coarsening of sediment would be diagnostic of this latter type mixing.

Recent censuses of deep-sea sediment appear to point at benthic foraminifera, nematodes, and other small animals as the mixers, at least in the deep sea (see, for instance, the censuses in: Saidova, 1971; Hessler and Jumars, 1974; Thiel, 1977; Coul et al., 1977; Bernstein et al., 1978).

The size of the animals is important for several reasons. First of all, it affects sampling strategy. If large animals at infrequent intervals do the mixing, we must use large samples to average out the effects of discrete events. Size also controls the precision of our model of the mixed layer: Does the mixed layer have a sharp bottom boundary or does the intensity of mixing gradually decay? Large animals may create boundaries of the gradual type whereas small animals are likely to create either gradual or sharp boundaries. In shallow waters, where a high food supply supports dense populations of large animals, the mixed layer boundary is apparently ragged (see figs in Rhoads, 1974; Aller and Cochran, 1976; Jumars, 1978).

In the deep sea, closely spaced ^{14}C data commonly exhibit fairly sharp boundaries at the bottom of the mixed layer (see Chapter 4, Fig 4.6). This supports the idea that small animals do much of the mixing.

On the other hand, deep-sea cores generally do show filled-in burrows greater than 5 mm in diameter. Arrhenius (1952) and Berger et al. (1979) show some striking examples. Such burrows weaken the Goldberg-Koide model since they often penetrate well below the mixed layer, where such a layer exists. The magnitude of the flux of material dug up by deep-burrowers is thus an important piece of information. For this reason, a later section looks at how to measure the magnitude of the fluxes involved. It may be that in regions of high productivity, such as the eastern equatorial Pacific -- the region of the cores in Arrhenius (1952) and Berger et al. (1979) -- that the Goldberg-Koide model breaks down due to excessive deep burrowing.

Another question of practical importance is how fast the sediment in the mixed layer mixes. When the mixing is much faster than all other processes which detectably change the sediment, the layer will be homogeneous. This simplification was introduced by Berger and Heath (1968), who also elaborated on some of the consequences.

Goldberg and Koide (1962) treated the mixing as a diffusion with constant diffusivity in the mixed layer and zero elsewhere. Recent measurements of ^{210}Pb and ^{32}Si in 10 deep-sea cores from the Atlantic, Pacific, and Antarctic Oceans have suggested diffusivities ranging from 30 to 500 cm^2/kyr (Nozaki et al., 1977; Peng et al., 1979; DeMaster, 1979; Cochran, 1979). Guinasso and Schink (1975) also found such high

rates when they analyzed the vertical distributions of bomb-produced plutonium in several deep-sea cores. But these latter two workers calculated much lower rates from the distributions of microtektites. More recently their group reported rates of 100 to 700 cm^2/kyr from the Atlantic using ^{210}Pb and ^{137}Cs (J.W. Johnson et al., 1978).

If the sediment indeed mixes at the rates indicated by the various radio-isotopes, then for our purposes mixing is virtually instantaneous. Derivations in Sections 2, 3, and 5 explicitly assume this. Section 4 discusses some possible corrections for finite mixing rates.

1.2. Influx

Influx to the mixed layer includes:

- 1) fresh, signal-carrying sediment from living or recently dead animals and plants, from wind-blown dust and from volcanoes;
- 2) older sediment from suspension and from slumps and turbidity currents;
- 3) newly precipitated minerals.

The last of these generally contributes little mass to foraminiferal ooze. The only precipitate of interest to us here is MnO_2 : According to DeMaster (1979) it may serve as a trap for ^{226}Ra and, consequently, a source for ^{210}Pb . This affects use of ^{210}Pb as a monitor of mixing rates.

In places where turbidity currents and slumps contribute sediment, the model of Fig. 2.1 may fail. So much material may arrive at once that the bottom of the mixed layer jumps upward without continuously mixing new material with old. The problem of older material

arriving from suspension is somewhat more tractable: Suspended sediment is mostly very fine (Table 2.1). Thus, any analysis of the coarser particles need only worry about the diluting effects of suspensoid.

Particle diameter	Half-distance
100 μ	2 km
50 μ	5 km
25 μ	20 km
10 μ	200 km
5 μ	1000 km
1 μ	∞

Table 2.1. Fallout pattern of suspended particles in 5 cm/sec current. After travelling distances shown, concentration of a dilute cloud of particles of given size will have fallen by one-half. The calculations are based on those of McCave and Swift (1976) but use a particle density of 1.5 gm/cm³. Benthic boundary layer is assumed to be 100 m thick.

In areas of topography, fine material apparently tends to be moved from higher levels to lower by winnowing (Bramlette and Bradley, 1941; van Andel, 1973).

1.3. Leaks

The model of Fig. 2.1 requires that all distorting effects occur in the mixed layer. In general, this is not true. For instance, overburden will eventually compact the sediment. This will cause dewatering and possibly chemical change. In this report, we ignore all these effects and assume sediment density is constant down core. For the short cores in Chapter 4 this is probably a safe assumption: T.C. Johnson et al. (1977) measured density in these cores and found less than a 3% variation down individual cores and less than 8% variation between cores.

A more relevant problem is silica dissolution, which can continue for meters into the sediment [Schink and Guinasso, 1977a; for evidence of this phenomenon on Ontong-Java Plateau, see Thompson's (1976) counts of radiolaria in core V28-238; see also, Berger, 1974, his Fig 14; Mikkelsen, 1978]. Consequently, the model of Fig. 2.1 will probably not work in reconstructing the history recorded by siliceous microfossils. However, because most silica dissolution does take place in the mixed layer in foraminiferal ooze (Schink and Guinasso, 1977a), the model should handle the effect of silica as a dilutant.

A particularly convenient assumption that we will exploit shortly is that the leaks -- winnowing and dissolution -- do not select particles by age (Schink and Guinasso, 1977a,b, and Sundquist et al., 1977, make this assumption). Evidence in support of this does not exist. Processes to the contrary may go on: Most fresh, fine carbonate material probably arrives at the seafloor cocooned in fecal pellets (Honjo, 1975). Likewise, some researchers believe that organic coatings initially protect foraminiferal shells from dissolution (Chave, 1965; Suess, 1970). On the other hand, W.H. Berger has suggested to me that much of the carbonate dissolution loss may come from weakly constructed, susceptible individuals. These individuals, as a group, would have a shorter residence time in the mixed layer; thus, their mean age would be less than that of the mixed layer as a whole. Clearly, then, the assumption of age-independent leaking is very tentative.

1.4. Conversions

In the derivations which follow, we carry along a term for

"conversion." We do this mainly to include the effects of fragmentation due to carbonate dissolution (Berger, 1973; Luz and Shackleton, 1975). However, the results apply just as well to any process which converts one type of particle into another. The only restriction is that the process be confined to the mixed layer.

We will assume in the derivations that the rate of conversion is proportional to the amount of subject material present in the mixed layer. For fragmentation, we can imagine an experiment in which we put a sample of whole shells into a bottle of undersaturated seawater: If the bottle is 1 cm^2 square and filled with $Z \text{ cm}$ of shells, then we define a decay rate, K , such that the fraction, n , of whole shells varies as $\frac{dn}{dt} = -KZn$. K need not be constant. In the deep sea, K will probably vary with sedimentation rate, dissolution rate, and faunal composition.

2. Problem: reconstructing a non-radioactive signal

Using the model of Fig 2.1, we now attack several practical problems of signal reconstruction. The problems include:

- 1) reconstructing a non-radioactive signal,
- 2) dating a reconstructed signal with radio-isotopes,
- 3) accounting for finite mixing rates,
- 4) and testing for the presence of deep-burrows.

The first problem can be stated thusly: Given a set of observations down core, $c = c(z)$, what were their corresponding values in fresh sediment, $c_0 = c_0(z)$?

In practice, $c(z)$ is usually some concentration within a certain fraction of the sediment. This fraction may itself vary in time. As a consequence, to reconstruct observations within any fraction, we must first reconstruct variations of the fraction. In what follows, we let $n = n(z)$ be the magnitude of the carrier fraction observed down core and $n_0 = n_0(z)$ be the corresponding magnitude in fresh sediment. Table 2.2 gives examples of signals and their carrier fraction.

signal, $c(z)$	carrier fraction, $n(z)$
abundance of given species	size fraction counted
diameter of given species	species
$\delta^{18}O$ of given species of given size	species of that size
^{14}C age of bulk sediment	carbonate particles
^{14}C age of coarse fraction	carbonate particles in coarse fraction

Table 2.2. Examples of signals and carriers. ^{14}C is discussed in Section 3. In cores considered in Chapter 4, the coarse fraction is nearly 100% carbonate, so that the carrier fraction for the ^{14}C age of the coarse fraction is simply the coarse fraction itself.

2.1. Solution

To reconstruct a non-radioactive signal, we first make the assumptions

- 1) that the model of Fig. 2.1 is true,
- 2) that mixing is fast enough to homogenize the mixed layer,

- 3) that the mixed layer thickness remains constant,
- 4) and that sediment density does not change.

According to the model, accumulating sediment leaves a record by pushing material out of the bottom of the mixed layer. By assuming a homogeneous mixed layer, we thus assume that observations down core are observations of past mixed layer values. Consequently, to find c_o and n_o from c and n , we write the debits, credits, and net change per unit area of the mixed layer at any time t :

$$\begin{aligned}
 &\text{mixed layer change} \\
 &= \text{influx} - \text{leaks} - \text{conversion} - \text{output} \\
 &= \text{fresh sediment input} + \text{horizontal influx} \\
 &\quad - \text{winnowing} - \text{dissolution} - \text{conversions} \\
 &\quad - \text{output}
 \end{aligned}$$

In symbols, for the change in the carrier fraction, this equation is

$$\begin{aligned}
 Zdn &= n_o s_o dt + n_h s_h dt \\
 &\quad - n_w s_w dt - n_D s_D dt - n_K K Z dt \\
 &\quad - n(s_o + s_h - s_w - s_D) dt
 \end{aligned} \tag{2.1}$$

For the corresponding change in observed signal,

$$\begin{aligned}
 Zd(nc) &= n_o c_o s_o dt + n_h c_h s_h dt \\
 &\quad - n_w c_w s_w dt - n_D c_D s_D dt - n_K c_K K Z dt \\
 &\quad - nc(s_o + s_h - s_w - s_D) dt
 \end{aligned} \tag{2.2}$$

where

$c = c(z)$ is the observed value of the parameter of interest; the parameter is associated with solid particles (Table 2.2); at earlier time, c was value of the parameter in mixed layer; at that time, material now at depth z was at bottom of mixed layer;

$c_o = c_o(z)$ was the value of parameter in fresh sediment when the

sediment now at z was at the bottom of the mixed layer;

$n = n(z)$ is the observed fraction of particles carrying parameter of interest;

$n_o = n_o(z)$ was the fraction of particles carrying parameter in fresh sediment when sediment now at z was at bottom of mixed layer;

$s_o = s_o(z)$ was sedimentation rate (cm/kyr) of fresh sediment when sediment now at z was at bottom of mixed layer;

$s_h(z)$, $s_w(z)$, and $s_D(z)$ are similar to $s_o(z)$ except that they give effective sedimentation rate of horizontally-transported, winnowed, and dissolved material, resp.; units are cm/kyr, for instance;

$K=K(z)$ was conversion rate of one type particle into another (kyr^{-1}); we define $K < 0$ to mean that the fraction n gains by conversion;

$c_h(z)$, $c_w(z)$, $c_D(z)$, and $c_K(z)$ are similar to $c_o(z)$ except that they give value of the parameter of interest in particles in horizontally-transported, winnowed, dissolved, and converted material, resp.;

$n_h(z)$, $n_w(z)$, $n_D(z)$, and $n_K(z)$ are similar to $n_o(z)$ except that they give fraction of particles carrying parameter in horizontally-transported, winnowed, dissolved, and converted sediment, resp.;

Equations of the same form, but less inclusive, appear in Sundquist et al. (1977).

Solving eq (2.1) algebraically for n_o , we get

$$n_o = \frac{1}{s_o} (ns - n_h s_h + n_w s_w + n_D s_D + n_K ZK) + \frac{s}{s_o} Z \frac{dn}{dz} \quad (2.3)$$

Here we introduce $s = s_o + s_h - s_w - s_D$, which is the accumulation rate: $s = dz/dt$. Now, $d(cn) = c dn + n dc$. Eq (2.1) gives dn . Substituting these in eq (2.2) yields

$$c_o = c + \frac{1}{n_o s_o} [-n_h s_h (c_h - c) + n_w s_w (c_w - c) + n_D s_D (c_D - c) + n_K K Z (c_K - c)] + \frac{n s}{n_o s_o} Z \frac{dc}{dz} . \quad (2.4)$$

2.2. Discussion

Obviously, to reconstruct c_o , all variables on the right sides of eq (2.3) and eq (2.4) must be known. Except for c and n and their derivatives, finding the instantaneous values of these variables is a major undertaking. The five terms at the beginning of eq (2.3) and eq (2.4) apply even during steady state; they thus must be known even for low-resolution stratigraphy. They include the effects of enrichment and impoverishment of the mixed layer due to leaks, conversion, and dilution.

More important at times than these steady-state terms are the transient-sensitive terms on the end of eq (2.3) and eq (2.4). The transient-sensitive terms include a multiplier which amplifies small changes in the observations. The multiplier consists of Z [as in eq (1.1)] and a coefficient. The coefficient in eq (2.3), s/s_o , is the ratio of output volume flux to input volume flux. The coefficient in eq (2.4), $\frac{n s}{n_o s_o}$, is the ratio of the output particle flux to the input particle flux, the particles being the type particular to the observations

(Table 2.2).

In eq (2.4), the coefficient can have the effect of changing the "time" constant of mixing. Thus, when enrichment is not a factor ($c=c_h=c_w=c_D=c_K$), the rate of response of the output to changes in the input varies as the ratio of output to input particle fluxes. However, we must put "time" in quotes because the record we see is not a function of time but of depth in core. That is, eq (2.3) and eq (2.4) depend explicitly on z only.

The physical reason in this case that the "time" constant is affected by the flux ratio is that leaks and conversions -- as well as output -- can help sweep older material out of the mixed layer; on the other hand, horizontal influx can slow down the cleaning process by continually adding material of the same character as the mixed layer. The faster the cleaning, the more closely the mixed signal appears to track the original signal. Another way to look at it is that leaks, conversion, and horizontal influx tend to compress or expand the output record.

2.2.1. Simple dissolution

A special case of interest is one in which carbonate dissolution dominates. Here observations of the fraction of carbonate in the sediment provide clues to the dissolution rate, s_D , which we need in all reconstructions.

If we know the original unmixed carbonate percentage, $n_0(z)$, then the dissolution rate follows from eq (2.3):

$$\frac{s}{s_0} = \frac{s_0 - s_D}{s_0} = \frac{1 - n_0}{1 - \bar{n}} \quad (2.5)$$

where $\bar{n} = n + z \frac{dn}{dz}$. For this equation, we assume $s_w = s_h = 0$. We also assume that all the carbonate particles can be subjected to dissolution ($n_D = 1$) and that carbonate does not convert spontaneously into any other mineral ($K=0$). Note that eq (2.5) is similar to the steady-state version (Heath and Culberson, 1970) except in the latter $\bar{n} = n$.

At high carbonate percentages, eq (2.5) is very sensitive to $n_0(z)$. Consequently, accurately finding this is an important first step in finding s_D . The usual way (Heath and Culberson, 1970) is to try to take a shallow core unaffected by dissolution. This has a weakness in that shallow cores are sometimes winnowed, and winnowing generally enriches sediment in coarse, high-carbonate particles (Moore et al., 1973). We will ignore this weakness so that we can address the following practical problem: Suppose we indeed have an unwinnowed shallow core (say, Core 1) and also a dissolved but nearby, unwinnowed, deeper core (say, Core 2). Using only carbonate percentages, how do we find s/s_0 at all levels in the deeper core? The difficulty here is in correlating levels, z_1 and z_2 , in the two cores so that we can apply eq (2.5).

The solution is a progressive, downward integration of eq (2.5).

$$\begin{aligned} z_2 &= \int_0^{z_1} \frac{s}{s_0} dz \\ &= \int_0^{z_1} \frac{1 - n_0(\xi)}{1 - \bar{n}(\xi)} d\xi \end{aligned}$$

where $d\xi$ are small increments in the undissolved core; the n_o come from observations down the undissolved core and the \hat{n} come from observations down the dissolved one. To perform the integration, we let $\xi=0$ be the bottom of the mixed layer. The value, $\hat{n}(0)$, can be immediately calculated since the bottom of the mixed layers of the two cores are synchronous. For the first depth increment,

$$z_2(\Delta\xi) = \frac{1-n_o(0)}{1-\hat{n}(0)} \Delta\xi ;$$

for the second depth increment, we use the \hat{n} calculated at the last z_2 ,

$$z_2(2\Delta\xi) = z_2(\Delta\xi) + \frac{1-n_o(2\Delta\xi)}{1-\hat{n}(\Delta\xi)} \Delta\xi ;$$

and so on for each additional increment. Better estimates of the \hat{n} at each new level can be achieved by a Taylor series expansion about the previous level.

The result of the integration is a correlation of each level in the dissolved core with each level in the undissolved core. The integration simultaneously provides the desired s/s_o for the dissolved core.

2.2.2. Errors in the coefficient

Errors in the coefficient $\frac{ns}{n_o s_o}$ tend to produce the same kind of response as errors in the mixed layer thickness, Z . At most, the reconstructed signal, c_o , depends 100% on the slope term $\frac{ns}{n_o s_o} \frac{dc}{dz}$. Therefore, assuming that the errors for the bracket term in eq (2.4) are small, a 10% error in $\frac{ns}{n_o s_o}$ results in at most a 10% error in c_o .

An example is the case of simple carbonate dissolution, there

being errors in measured carbonate fraction. Given such errors, we now seek the resulting errors in $\frac{ns}{n_0 s_0}$, in the case where we must deduce $\frac{s}{s_0}$ from eq (2.5). We assume that the carbonate fractions involved are large (say, >70%) and that the measurement errors are small relative to the fraction. We further assume that the stratigraphic correlation which provides n_0 is perfect. This last may at times be a very poor assumption, but what we seek here is a handle on error amplification even under the best of circumstances.

We let the flux ratio be called q ; from eq (2.5),

$$q = \frac{n}{n_0} \frac{1-n_0}{1-\bar{n}}$$

We then define \bar{n} and n_0 in terms of finite differences:

$$n_0 = (Z/\Delta z + 1)m_1 - (Z/\Delta z)m_2$$

$$\bar{n} = (Z/\Delta z + 1)n_1 - (Z/\Delta z)n_2,$$

where m_1 and m_2 are observations in the shallow core which provides n_0 , and n_1 and n_2 are observations in the deeper core whose flux ratio we seek. Now, if the observations have small random errors, dm_1 , dm_2 , dn_1 , and dn_2 , then the consequent error in calculating the flux ratio, q , is

$$\begin{aligned} dq &= \frac{\partial q}{\partial m_1} dm_1 + \frac{\partial q}{\partial m_2} dm_2 + \frac{\partial q}{\partial n_1} dn_1 + \frac{\partial q}{\partial n_2} dn_2 \\ &= q \left[\frac{1+Z/\Delta z}{(1-n_0)n_0} dm_1 + \frac{Z/\Delta z}{(1-n_0)n_0} dm_2 + \frac{dn_1}{n} + \frac{1+Z/\Delta z}{1-\bar{n}} dn_1 + \frac{Z/\Delta z}{1-\bar{n}} dn_2 \right]. \end{aligned}$$

Assuming that all the observational errors are independent, we then can find the variance of dq ($=\text{var}[q]$):

$$\text{var}[dq] = q^2 \sigma^2 (2Z^2/\Delta z^2 + 2Z/\Delta z + 1) \left[\frac{1}{[(1-n_0)n_0]^2} + \frac{1}{(1-\bar{n})^2} \right] + \frac{2\sigma^2}{n^2}.$$

where $\sigma^2 = \text{var}[dm_1] = \text{var}[dm_2] = \text{var}[dn_1] = \text{var}[dn_2]$.

Take, for example, the case where carbonate is measured to $\pm 1\%$, i.e., $\sigma = .01$. Let $Z = 8$ cm, $n_0 = .9$ and $n = \bar{n} = .8$, which are not unusual values in the deep sea. For these numbers, the flux ratio, q , becomes .44 and its rms error is about $1.5q$. The multiplier in the transient-sensitive term in eq (2.4), qZ , is thus 3.5 ± 5.2 cm.

For this typical example then, measuring carbonate to $\pm 1\%$ at 1-cm intervals is worthless. Reconstructed signals will zig-zag as the multiplier, qZ , ranges from zero (total dissolution, no accumulation) to Z (no dissolution). It is then clear, for instance, that the correlation procedure of the previous section requires measurement precision much greater than 1%.

3. Problem: dating mixed sediment

The next question we ask is this: How can we use ^{14}C to date events in the reconstructed record? The assumptions listed at the beginning of the last section -- constant density, constant Z , and fast mixing -- apply here as well.

3.1. Solution

The assumption of fast mixing implies that any event recorded in fresh sediment makes itself immediately felt in the still sediment at the bottom of the mixed layer. When we reconstruct a signal in the still sediment by eq (2.3) and eq (2.4), the reconstructed signal of the most recent period appears just below the mixed layer.

For this reason, it is convenient to turn the ^{14}C clock on when particles pass through the lower boundary of the mixed layer. That is, in the model, the true age of any event is given by

$$c_r = ce^{\lambda t},$$

where t (< 0) is the true age of the event, λ is the decay constant of ^{14}C ($\lambda = .12449 \text{ kyr}^{-1}$; see Faure, 1977), c is the concentration of ^{14}C in the carrier fraction that the mixed layer had at time t , and c_r is the reported concentration at the depth in core the (reconstructed) event. We let c_o be the concentration of ^{14}C in the carrier fraction of fresh sediment at time t . In practice, reported ^{14}C dates assume an initial concentration c_{or} [which is usually 95% of that of the NBS standard (Broecker and Olson, 1959) and may or may not include a correction for fractionation]. Consequently, the true age of the event is

$$t = \frac{1}{\lambda} \ln(c_r/c) \quad (2.6)$$

$$\begin{aligned} &= \frac{1}{\lambda} \ln[(c_r/c_{or})(c_o/c)(c_{or}/c_o)] \\ &= \frac{1}{\lambda} \ln(c_r/c_{or}) + \frac{1}{\lambda} \ln(c_o/c) + \frac{1}{\lambda} \ln(c_{or}/c_o) \\ &= t_r - t_{ML} + \frac{1}{\lambda} \ln(c_{or}/c_o). \end{aligned} \quad (2.7)$$

Here t_r is the reported ^{14}C age and t_{ML} is the "age" which the mixed layer would have shown at time t . (The "age", t_{ML} , is merely a measure of the ^{14}C in the mixed layer and is not per se an age at all).

Thus, to date an event recorded at level z , we simply subtract the contemporaneous mixed layer age from the reported age and add a small correction for c_o . The contemporaneous mixed layer age is the age the mixed layer must have displayed when the material now at depth z was

at the bottom of the mixed layer.

An important point to realize is that with this procedure we are dating events and not shells. We use the ^{14}C concentration to measure the time elapsed since the (reconstructed) event. It does not matter what carrier fraction the event is recorded in. Thus, if we are dating an event in the species abundance of large foraminifera, ^{14}C ages from the bulk material do just as well as ages from the coarse fraction. In fact, ages from the bulk material are preferable. We shall see shortly that the mixed layer age of the coarse fraction is very sensitive to changes in dissolution, winnowing, and productivity. The mixed layer age of the bulk material is -- under circumstances of interest here -- much less sensitive.

The last term on the right in (2.7) depends on ^{14}C production rates in the upper atmosphere and ocean circulation (Stuiver, 1978). The variation of this term can be seen in a paper by Ralph and Michael (1974), who summarize available comparisons of tree ring counts and tree ring ^{14}C dates. These data show that ^{14}C ages are about 800 yr younger than tree ring ages for dates before about 5500 BP. Their data end at 7500 BP but Stuiver's (1978) sparse data suggest that this offset may continue until about 28,000 BP.

The 800 yr shift appears to have been gradual, ending about 2000 BP. The effect on reported oceanic sedimentation rates should be an apparent increase of about 20% from 5500 BP until 2000 BP. Stuiver (1971) in fact sees evidence for such an increase in lake sediments.

3.1.1. Age of the mixed layer

We can derive the contemporaneous mixed layer age from an equation similar to eq (2.2). In this case, we let c be the ^{14}C concentration in the carrier fraction in the mixed layer. Also, the right side of eq (2.2) must now contain a decay term, $-nc\lambda Zdt$. In dating bulk foraminiferal ooze, n must be the carbonate fraction; in dating only coarse particles from ooze, n must be the coarse fraction, since this fraction is essentially 100% carbonate.

To get the mixed layer age at any time t , we solve the modified eq (2.2) algebraically for c_0/c and subsequently calculate $\frac{1}{\lambda} \ln(c_0/c)$. Before doing this, we note that differentiating eq (2.6) gives

$$\begin{aligned} dt &= dc_r/dc_r - dc/dc \\ &= dt_r - dc/dc \\ &= dz/s_r - dc/dc \end{aligned}$$

where s_r is the instantaneous sedimentation rate displayed by the reported ^{14}C dates.

On substitution of the last relation in the decay term, the modified eq (2.2) becomes

$$\begin{aligned} Zcdn &= dz[s_0 n_0 c_0/s + s_h n_h c_h/s - s_w n_w c_w/s - s_D n_D c_D/s \\ &\quad - KZn_K c_K/s - nc - nc\lambda Z/s_r] . \end{aligned}$$

The conversion term, $KZn_K c_K/s$, appears only if material is lost from or gained by the fraction being dated. For example, fragmentation does not affect dates of bulk sediment but does affect dates of the coarse frac-

tion.

Using eq (2.1) for Zdn and solving for c_o/c , we get two useful forms for c_o/c : One form is

$$c_o/c = 1 + \frac{dZ}{s_r} \frac{ns}{n_o s_o} + \frac{n_h s_h}{n_o s_o} \frac{c-c_h}{c} - \frac{n_w s_w}{n_o s_o} \frac{c-c_w}{c} - \frac{n_D s_D}{n_o s_o} \frac{c-c_D}{c} - \frac{n_K KZ}{n_o s_o} \frac{c-c_K}{c}.$$

When the age of the material in leaks, conversions, and horizontal influx is the same as that of the mixed layer, this equation shows that

$$t_{ML} = \frac{-1}{d} \ln \left[1 + \frac{dZ}{s_r} \frac{ns}{n_o s_o} \right]. \quad (2.8a)$$

(We keep to my convention that ages are negative). The other form of the solution for c_o/c gives the the mixed layer age in cases where $c \neq c_h$, $c \neq c_w$, $c \neq c_D$, and $c \neq c_K$:

$$t_{ML} = \frac{-1}{d} \ln \left[1 + \frac{dZ}{s_r} \frac{ns}{n_o s_o} + \frac{n_h s_h}{n_o s_o} - \frac{n_w s_w}{n_o s_o} - \frac{n_D s_D}{n_o s_o} - \frac{n_K KZ}{n_o s_o} \right] + \frac{1}{d} \ln \left[1 + \frac{n_h s_h c_h}{n_o s_o c_o} - \frac{n_w s_w c_w}{n_o s_o c_o} - \frac{n_D s_D c_D}{n_o s_o c_o} - \frac{n_K KZ c_K}{n_o s_o c_o} \right]. \quad (2.8b)$$

3.2. Discussion

In the steady state, with no leaks, conversions, or horizontal influx, eq (2.8b) reduces to the equation derived by Peng et al. (1977) and Nozaki et al. (1977).

Notice in eq (2.8a) that the factor $\frac{ns}{n_o s_o}$ again modulates the effect of the mixed layer thickness Z . For a given mixed layer thickness and for a given reported sedimentation rate, s_r , leaks tend to make

the mixed layer appear younger and horizontal influx tends to make it appear older.

3.2.1. Steady state

Under steady state conditions, the actual accumulation rate, s , equals the apparent sedimentation rate, s_r . When eq (2.8a) applies, the age of the steady state mixed layer is then

$$t_{ML} = \frac{-1}{\alpha} \text{Ln} \left[1 + \frac{\alpha Z n}{s_o n_o} \right] . \quad (2.8c)$$

A nomograph of this function -- which is used extensively in Chapter 4 -- appears in Fig 2.2. When eq (2.8c) holds, leaks, conversions and horizontal influx affect the mixed layer age only by affecting carrier fraction. In the case of dating bulk sediment, the carbonate fraction is the carrier. Carbonate dissolution then makes the mixed layer younger and winnowing makes it older, for instance. (Winnowing's effect stems from the relatively large amount of non-carbonates in the fine fraction). If horizontal influx is of the same age as the mixed layer and has the same carbonate fraction, then of course the influx does not change the mixed layer age. Such a condition would result when the influx is merely local mixed layer material.

A rationalization of the effect of the ratio, n/n_o , on mixed layer ages in the steady state has to do with the "residence time," $\frac{nZ}{n_o s_o}$. As n decreases relative to n_o , the residence time of the fraction in the mixed layer decreases; hence, the mixed layer age of the fraction decreases. When $\frac{nZ}{n_o s_o} \ll 1$, the mixed layer age is in fact equal to the

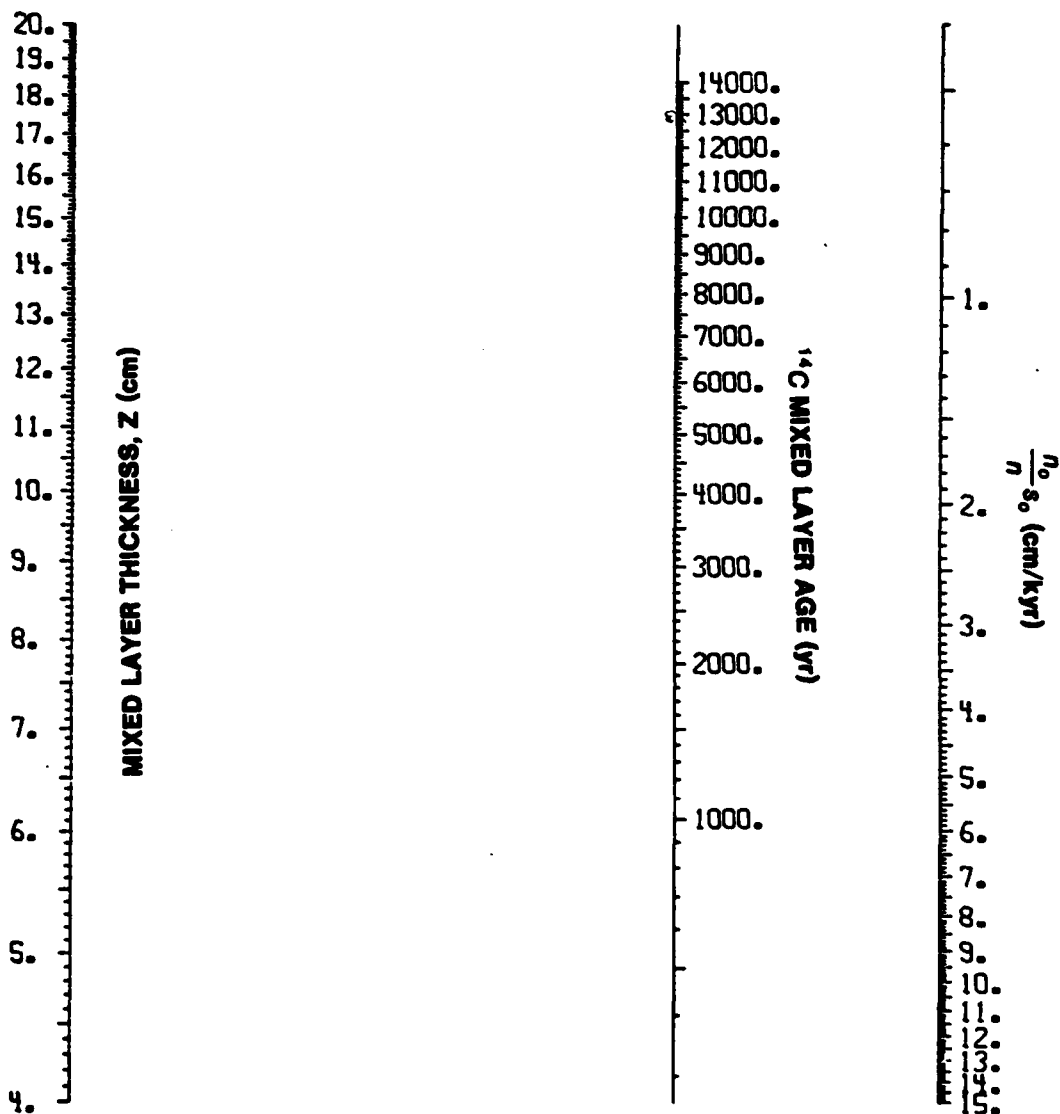


Fig 2.2. Nomograph of ^{14}C age of the mixed layer under certain additional assumptions. Besides making the assumptions listed at the beginning of Section 2.1.1, we also assume steady state and that the age of the material in leaks, conversions, and horizontal influx is the same as the mixed layer.

residence time, as can be seen by expanding the logarithm in eq (2.8c).

Another way to view the effect of the ratio, n/n_0 , is to consider the mass balance of the mixed layer. When n is less than n_0 , the amount of decaying material in the mixed layer is reduced; hence, the rate of decay is reduced and so the mixed layer appears younger.

A special but useful case occurs when the carrier fraction, n , is large. In this case, large changes in leaks, conversions, and horizontal influx change n only slightly. The most useful case is when dating bulk sediment, n being the carbonate fraction. It is not unusual in this instance to have $n > 70\%$ and $n_0 = 90\%$. Thus, when $s/s_0 = .5$, $n/n_0 = 8/9$. For this situation and ones like it, we can neglect effects of changing n in the mixed layer. The mixed layer age then becomes a measure of the pelagic sedimentation rate, s_0 . A few more ^{14}C measurements below the mixed layer give the accumulation rate. The size of leaks and horizontal influx then follows by subtraction: $s_0 - s$. (But when using this approach, we must keep in mind the long list of assumptions, including: $n = n_0$, $c = c_D = c_K = c_W = c_h$, $s = s_r$).

In dating only certain size fractions (e.g., Rubin and Suess, 1955), the ratio n/n_0 usually varies more widely, n here being the weight percentage of the size fraction of interest. It is not surprising, then, to find widely different ages for different size fractions from the same stratigraphic level.

Take as an example an instance where we are dating the sand fraction in a core subject to carbonate dissolution. Since dissolution decreases the sand fraction by fragmentation, $n < n_0$ during periods of

dissolution. Therefore, the age of the sand fraction in the mixed layer decreases at these times.

A typical case might be $n_0 = .50$ with n falling to $.25$ during periods of dissolution. Thompson's (1976) measurements for V28-238 show many such cases. (We assume here that the periods are long enough for a steady state to be established). For a case where $Z = 8$ cm and $s_0 = 2$ cm/kyr, the undissolved age of the sand fraction in the mixed layer would be 3300 yr (Fig 2.2). The age during periods of dissolution ($n = .25$) would fall to 1800 yr, a 1500 yr difference. On the other hand, the difference in ages for measurements on the total sediment would be less than 400 yr, assuming in this example that carbonate percentage changes from 90% to 80% during dissolution.

3.2.2. Age of material in leaks and horizontal influx

Key assumptions in eq (2.8c) are that $c = c_h = c_D = c_w = c_K$. That is, the formula assumes that the material in horizontal influx, leaks and conversions is the same age as that in the mixed layer. Whether or not this is so depends in part on local conditions and in part on crystal chemistry.

Let us take first the case of horizontal influx and winnowing, in the absence of dissolution. In this case, local conditions play the biggest role. If a site suffers winnowing of the fine fraction without any horizontal influx, the material removed is younger than the bulk sediment in the mixed layer. This is because the fine fraction has a lower residence time in the mixed layer. In other words, eq (2.8c) might apply to the fine fraction ($< 62\mu$) but not to the bulk material.

Actually, parts of the fine fraction can probably be winnowed more easily than others; thus the age of the winnowed material must be still younger than the age of the fine ($<62\mu$) fraction.

The other extreme of local conditions is a case in which there is an influx of dead carbon ($c_h=0$) from an area of erosion. In this instance, the fine fraction is likely to be older than the coarse fraction.

A middle point includes cases where horizontal influx and winnowing alternate at a particular location. If the influx is winnowed from sites nearby, and if the mass of influx is more or less the same as the efflux later winnowed, then the fine fraction will indeed be the same age as the rest of the mixed layer. Eq (2.8c) will hold.

In the presence of carbonate dissolution, the validity of $c=c_h=c_D=c_w=c_K$ becomes more difficult to assess. For one thing, crystal chemistry plays a role. For another, dissolution as well as winnowing affects the fine fraction.

The role of crystal chemistry is that some particles may dissolve more quickly than others (see Berner, 1978; Keir, 1980). Large smooth particles may lose mass more slowly (per unit mass) than small, angular particles. Most of the dissolved $^{14}\text{CO}_3^{-2}$ may thus originate from mass of low residence time in the mixed layer. Consequently, for bulk sediment, it is likely that $c_D > c$; the bulk age of the mixed layer is likely to be greater than eq (2.8c) would lead us to expect.

On the other hand, there is some evidence that coccoliths (which

make up a large portion of the fine fraction in well-preserved sediment) are more "resistant" to dissolution than foraminifera (Berger, 1976; Roth and Berger, 1975). The coarse fraction in dissolved sediment should then be younger than the bulk material for two reasons: 1) The dissolved carbonate may be coming mostly (per unit mass) from the foraminifera and their fragments. And 2), the coarse fraction breaks down by fragmentation. If the coarse fraction is younger, the fine fraction must be older. Hence, material winnowed from dissolved sediment may be older than that from undissolved sediment. Such winnowed material may perhaps be older than the local mixed layer as a whole.

In short, the assumptions $c=c_h=c_D=c_w=c_K$ and the validity of eq (2.8c) can only be established by observations.

3.2.3. Non-steady state

Eq (2.8a) and eq (2.8b) account for non-steady sedimentation rates by including the reported sedimentation rate, s_r . The difficulty comes in estimating the actual accumulation rate, s . Since the slope of the ^{14}C record does not provide this in the non-steady state, we must deduce it from indirect observations. We might, for instance, extrapolate from higher stratigraphic levels at which a steady-state exists. We might also use fragment abundance, faunal counts, and other keys to indicate the various losses from and gains to s_0 .

An example of the ^{14}C record during non-steady state is the case where the mixed layer consists at time zero entirely of dead carbon ($t_{ML}=\infty$). At the next instant, we turn on sedimentation at its usual rate. (We assume $s=s_0$, $n=n_0$). The age of the mixed layer would behave

as in eq (2.8a), gradually growing younger. The reported sedimentation rate, s_r , would be very small at first and then slowly increase to s_0 .

To find the actual behavior of s_r in cases of known changes in sedimentation rate we must solve in the usual way the differential equation which describes ^{14}C in the mixed layer. Such an approach can also readily tell us the "time" constant of sedimentation rate changes. This particular question can be stated like this: Suppose that the mixed layer has achieved a steady state at some instant ($t=0$), so that the reported and actual accumulation rates are the same. Suppose further that at the next instant the sedimentation rate changes to a new value which stays constant indefinitely. How quickly does the apparent sedimentation rate, s_r , approach the new value?

To answer this question, we use eq (2.1) and eq (2.2) plus a decay term on the right, $-mZcdt$. If we take the simplest case -- where leaks, conversions, and horizontal influx are negligible -- the differential equation is

$$\frac{dc}{dt} + (s_2/Z+d)c = c_0 s_2/Z .$$

Here c is the concentration of ^{14}C in the mixed layer. Since we have assumed that the new sedimentation rate, s_2 , is constant, the solution to the differential equation is by inspection,

$$c(t) = \Delta c e^{-kt} + c_2 ,$$

where $k=s_2/Z+d$, and where Δc is the difference between the initial and final mixed layer concentrations, the latter of which is c_2 . The parameter k is the time constant of the mixed layer concentration. Thus,

when $s_2=2$ cm/kyr and $Z=8$ cm, it takes $8/3$ kyr or about 5 cm for the concentration to cover $2/3$ s of the "distance" to the new concentration. The time constant for the ^{14}C is thus significantly larger than the time constant for non-radioactive tracers (s_2/Z). For ^{14}C , the decay helps clean out the mixed layer.

Sedimentation rates do not adjust quite so quickly. For the simple case solved above for a sudden change in the steady sedimentation rate,

$$s_r = s_2 \frac{1 - \frac{dZ/s_1}{1+dZ/s_1} \frac{s_2-s_1}{s_2} e^{-kt}}{1 + \frac{1}{1+dZ/s_1} \frac{s_2-s_1}{s_1} e^{-kt}}.$$

Here s_1 is the initial sedimentation rate and s_2 is the final rate. This formula follows from the solution to the differential equation, with substitution of $1+dZ/s_r$, $1+dZ/s_2$, and $1+dZ/s_1$ for the inverse of the various concentrations (times c_0). The formula shows that s_r does not approach s_2 in a strictly exponential fashion. However, if the fractional change is $x = \frac{s_r-s_1}{s_2-s_1}$, then the time required to reach the fraction x is

$$t = \frac{-1}{K} \ln(1-x) + \frac{1}{K} \ln \left[1 + \frac{x}{s_1+dZ} \right].$$

which, for $x=1-e^{-1}$, is

$$t = \frac{1}{K} + \frac{1}{K} \ln \left[1 + \frac{1-e^{-1}}{s_1+dZ} \right].$$

The time for achieving $2/3$ s of the sedimentation rate change is thus

slightly longer than $1/k$. For the case $s_1=2$ cm/kyr and $Z=8$ cm, the time is about 20% longer.

In cases so far discussed, we have shown that the sedimentation rate must adjust slowly because the age of the mixed layer changes slowly. In cases with leaks, conversions, and horizontal influx, the accumulation rate, s , can sometimes change without changing the age of the mixed layer very much. (As we saw earlier, such maybe the case for ages in bulk sediment of high carbonate content). For these cases, sedimentation rates adjust immediately. Thus, if a particular ^{14}C record shows a sudden change in s_r , we should suspect a change in dissolution (s_D), winnowing (s_w), or horizontal influx (s_{bh}), but not in productivity (s_o).

When leaks, conversion, or horizontal influx do change the age of the mixed layer, the time constant of the change is

$$k = \frac{n_o s_2}{nZ} + d .$$

This follows from eq (2.1) and eq (2.2) with decay. It assumes that the material in leaks and conversions is the same age as that in the mixed layer. These latter processes only change the time constant by changing the "residence time" of the carrier fraction, n .

4. Problem: effect of finite mixing rates

We return in this section to reconstruction of non-radioactive signals. Some ^{210}Pb data suggest that mixing rates may at places in the deep sea be as low as $30 \text{ cm}^2/\text{kyr}$ (Turekian et al., 1978). How would

such rates affect signal reconstructions? Is it possible to include corrections for such rates in eq (2.3) and eq (2.4)?

4.1. Solution

To answer these questions, we simplify a result from Guinasso and Schink (1975). For brevity, we assume here that leaks, horizontal influx, and conversions can be neglected. As before, though, we assume that sediment density is constant and that the Goldberg-Koide (1962) model holds. We also assume that the sedimentation rate, s_o , is constant.

In the Goldberg-Koide model, solid particles diffuse throughout the mixed layer at a vertically constant rate, D . At any level, x , in the mixed layer, the local rate of change in the concentration, c_{ML} , of a particular type of (non-decaying) particle is

$$\frac{\partial c_{ML}}{\partial t} = D \frac{\partial^2 c_{ML}}{\partial x^2} - s_o \frac{\partial c_{ML}}{\partial x} . \quad (2.9)$$

(In this equation, x is positive downward). The first term on the right accounts for diffusion; the second term accounts for the movement of level x upward as sediment accumulates. The boundary conditions are that there is only a flux of fresh sediment through the sea bottom and that there is no diffusion through the mixed layer bottom.

4.1.1. Guinasso and Schink's solution

Guinasso and Schink (1975) solve for the impulse response of eq (2.9) and its boundary conditions. Their solution evaluated at the bot-

tom of the mixed layer ($x = Z$) represents the recorded impulse response at time t , t being measured from the instant of impulse:

$$h(t) = \sum_{m=0}^{\infty} a_m e^{-b_m t} \quad \text{for } t > 0, \quad (2.10a)$$

$$h(t) = 0 \quad \text{for } t \leq 0. \quad (2.10b)$$

where Guinasso and Schink show that

$$a_m = e^{1/2G} \frac{\cos \Theta_m + \frac{\sin \Theta_m}{2G\Theta_m}}{1/2 + \frac{1}{2G\Theta_m^2} + \frac{1}{8G^2\Theta_m^2}},$$

$$b_m = (1/4G + G\Theta_m^2)/Zs_0, \quad (2.11a)$$

Here $G = D/(s_0 Z)$ and the Θ_m are solutions of

$$\Theta_m^2 - \frac{1}{4G^2} - \frac{\Theta_m \cot \Theta_m}{G} = 0. \quad (2.11b)$$

4.1.2. Simplification

The form of eq (2.10a) suggests a simplification. Any sum of simple exponentials must be the solution of a linear ordinary differential equation with constant coefficients. In particular, eq (2.10a) must be a solution of

$$0 = h + u_1 \frac{dh}{dt} + u_2 \frac{d^2 h}{dt^2} + \dots + u_n \frac{d^n h}{dt^n} + \dots \quad (2.12)$$

We will see shortly that for our purposes a finite number of terms suffices. Given this, we can find the coefficients u_n immediately: For eq (2.10a) to be the solution of eq (2.12), each and every term on the

right in eq (2.10a) must satisfy eq (2.12); i.e., by substituting each term in eq (2.12), we see that

$$\begin{aligned} 0 &= 1 + b_0 u_1 + b_0^2 u_2 + \dots + b_0^N u_N \\ 0 &= 1 + b_1 u_1 + b_1^2 u_2 + \dots + b_1^N u_N \\ &\vdots \end{aligned} \tag{2.13}$$

$$0 = 1 + b_{N-1} u_1 + b_{N-1}^2 u_2 + \dots + b_{N-1}^N u_N .$$

where N is the order of eq (2.12) which we eventually decide will suffice. Solving these N equations simultaneously provides the u_n .

Since eq (2.10) is the impulse response of eq (2.8) and its boundary conditions, we might expect eq (2.10) also to be the impulse response of the right hand side of eq (2.12) and its initial conditions, whatever they may be. If this is true, we have a convenient equation for signal reconstruction:

$$c_0 = c + u_1 \frac{dc}{dz} + u_2 \frac{d^2 c}{dz^2} + \dots + u_N \frac{d^N c}{dz^N} . \tag{2.14}$$

(Here we have set $dt = dz/s_0$ and adjusted the u_n accordingly. In calculating derivatives, remember that we have defined z decreasing downward).

A numerical proof of eq (2.14) appears in Fig. 2.3. For reasons apparent in Chapter 4, the proof is in terms of c_0 as a step function rather than an impulse, the former being merely the integral of the latter. In the proof, we first convolve eq (2.10) with a step function to get

$$c(z) = \sum_{m=0}^M \frac{a_m}{b_m} \left[1 - e^{-b_m(z_0-z)} \right], \quad (2.15)$$

where z_0 is the present depth of the material which was at the bottom of the mixed layer at the instant of the step in c_0 . M is the number of terms we need to compute c to any set precision.

To continue the proof, we differentiate eq (2.15) to order N . Then we select some G and calculate the u_n from eq (2.13). Now we test eq (2.14). If c_0 approaches a step function as $N \rightarrow \infty$, the proof is complete. Alternatively, for a given N , if c_0 approaches a step function as $G \rightarrow \infty$, the proof is likewise complete. Fig 2.3 shows the latter proof.

4.2. Discussion

As Fig 2.3 shows, a second order equation does a remarkably good job of reconstruction when $G > .5$. (Computational error affects the first few mm of the response, c , and its derivatives).

The role of G becomes clear when we approximate b_0 and b_1 for $G \geq .5$. ($G=.5$ is equivalent to $D=8 \text{ cm}^2/\text{kyr}$, for $Z=8 \text{ cm}$ and $s_0=2 \text{ cm/kyr}$. This is certainly at the lower end of published mixing rates [other than the microtektite rates of Guinasso and Schink (1975)]}. Using the expansion $\cot \theta_0 = 1/\theta_0 - \theta_0/3 - \dots$ and noting that $\theta_n \approx n\pi$ for $n > 0$, we see from eq (2.11a) that

$$b_0 \approx \frac{1}{Z} \left[\frac{1}{4G} + \frac{1 + \frac{1}{4G}}{1 + \frac{1}{3G}} \right] \approx \frac{1}{Z} \quad \text{when } G \geq .5, \quad (2.16a)$$

$$b_1 \approx \frac{1}{Z} \left[\pi^2 G + \frac{1}{4G} \right] \approx \frac{\pi^2 G}{Z} \quad \text{when } G \geq .5. \quad (2.16b)$$

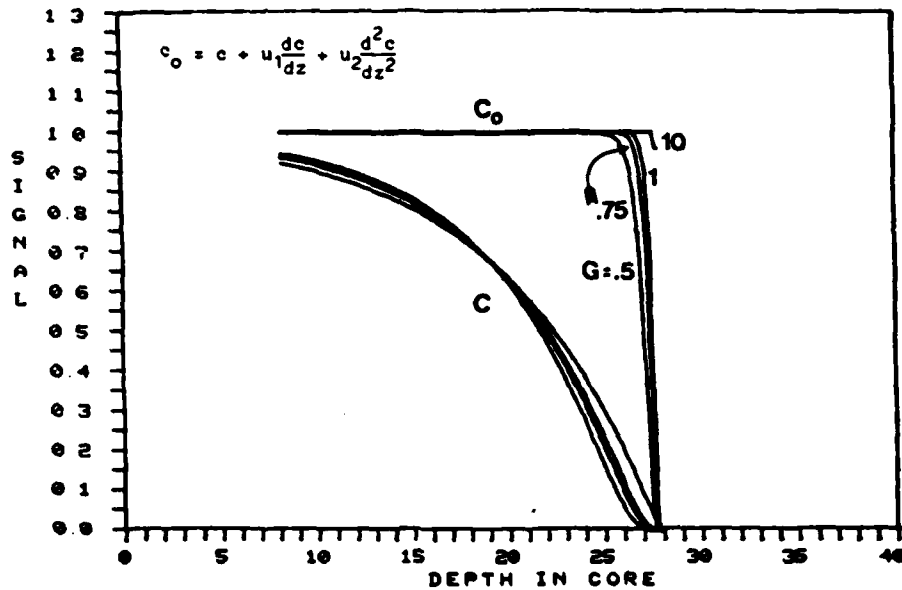


Fig 2.3. Proof that eq (2.10) is the impulse response of eq (2.14) and its initial conditions as $N \rightarrow \infty$. However, instead of letting $N \rightarrow \infty$, we set $N=2$ and let $G \rightarrow \infty$; also, rather than eq (2.10), we calculate c from eq (2.15), so that c_0 should converge to a step function rather than an impulse. The calculations of c use $M=9$; this and 6-digit word-length introduce computational error in c when z is within 2 mm of the step. The plot uses an 8 cm mixed layer thickness.

The solution of eq (2.13) for $N = 2$ is

$$u_1 = -(1/b_0 + 1/b_1)$$

$$u_2 = \frac{1}{b_0 b_1}$$

Substituting eq (2.16) into these equations and then these equations into eq (2.14), we find that

$$c_0 = c + z \frac{dc}{dz} + \frac{z^2}{w^2 G} \frac{d^2c}{dz^2} \quad (2.17)$$

Thus, as $G \rightarrow \infty$, eq (2.14) \rightarrow eq (1.1).

Fig 2.4 shows the effect of using eq (1.1) when $.5 \leq G \leq 10$. Infinity is effectively $G = 10$.

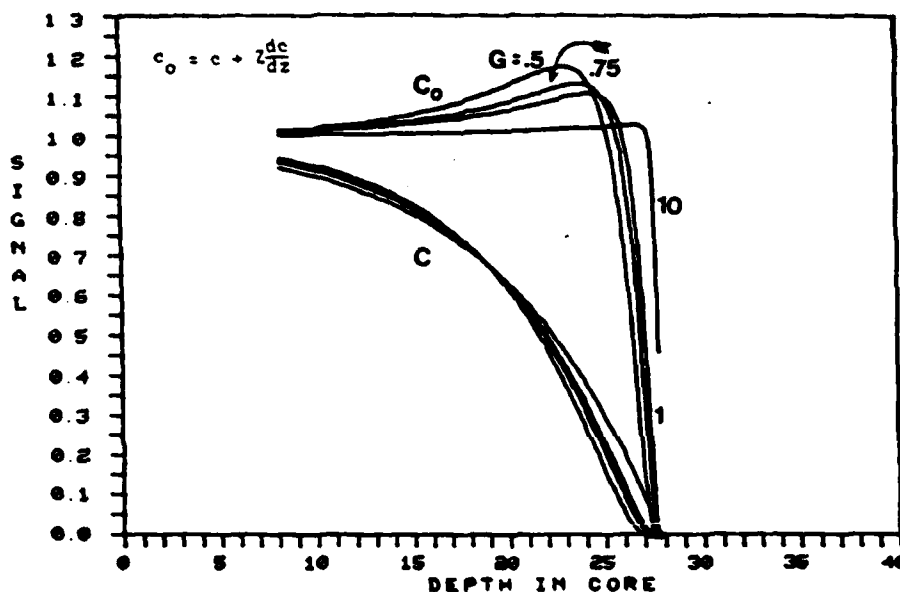


Fig 2.4. Result of using eq (1.1) on sediment mixed at finite rates when original unmixed input is a step function. In this figure, c is calculated from eq (2.15). Computational error affects c within 2 mm of step. The plot uses $Z=8$ cm.

When $G = 1$, eq (1.1) causes a 10% overshoot of a step function and a 1 cm delay in its appearance (for $Z = 8$ cm). By $G=5$, the overshoot has increased to 25% and the delay to 2-3 cm.

Eq (2.17) can be used to estimate the consequences of measuring error when calculating c_0 by eq (2.14). As in Chapter 1, let σ^2 be the variance in c and σ_0^2 be the resulting variance in the calculation of c_0 .

Then, for a sample interval of 1 cm, putting eq (2.17) in finite difference form shows that

$$\sigma_o^2 \approx \left[\frac{4Z^3}{\pi^2 G \Delta z^3} + \frac{6Z^4}{\pi^4 G^2 \Delta z^4} \right] \sigma^2 .$$

Thus, for $G=.5$, $Z=8$ cm, and $\Delta z=1$ cm, we need over 1400 replicates to bring σ_o down to σ . (This assumes that the mean of the replicates is the best estimator of c). In terms of improving σ , we must improve measuring precision by a factor of 37. This also means that to keep up with the ancient micropaleontologist who counts 300 specimens in a perpetual sediment trap, we must count 420,000 specimens per cm in the sediment.

5. Problem: Testing for deep-burrows

Many deep-sea cores show filled-in burrows which have apparently penetrated below the mixed layer. To correctly reconstruct signals with the formulas developed in the preceding 3 sections, we must be able to show that the material transported by these burrows is a small part of our samples.

5.1. Solution

One way to detect deep burrows may be to examine the ^{14}C record. The ^{14}C record may be a good indicator because deep-burrowing must tend to 1) make the mixed layer older and 2) change the apparent sedimentation rate at levels below the mixed layer.

We now develop a simple model to demonstrate these tendencies.

The model is not particularly realistic but it does provide a physical connection between the amount of burrowing and the expected changes in the ^{14}C record.

To begin with, assume

- 1) that there is no dissolution, winnowing, conversion, or horizontal influx,
- 2) that all rates are steady and the entire sediment is in a steady state,
- 3) that the mixed layer is homogeneous,
- 4) that material from deeper layers enters the mixed layer at a rate b cm/kyr,
- 5) that burrows never intersect,
- 6) that each depth increment during burrowing contributes an equal amount of burrowed material to the mixed layer,
- 7) that empty burrows fill with contemporary mixed layer material,
- 8) and that burrows reach to a depth Z_1 cm deeper than the mixed layer depth, Z .

This model may be visualized schematically as in Fig 2.5: all burrows are of length $Z+Z_1$; they are of constant diameter and occur at a constant frequency; the diameter and frequency are such as to result in the rate, b . (For instance, if $Z_1=10$ cm, and if the diameters are 1 cm and the frequency is 1 burrow/10 cm²kyr⁻¹, then $b=1$ cm/kyr, for square burrows).

The ratio, b/s_0 , is the fraction of the material in the historical record that is in burrows. A minimum estimate of this parameter can be deduced from looking at a core. Why the number of burrows visible is

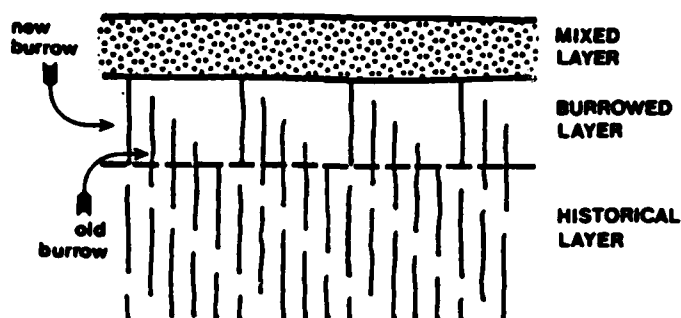


Fig 2.5. Schematic diagram of a model of deep-burrowing.

likely to be smaller than the number present is discussed by Berger et al. (1979).

Note from Fig 2.5 that burrow density is least at $z=Z$ and most at depths at or below $Z+Z_1$. This is a result, of course, of the deeper levels being older.

We first derive an expression for the age of sediment at various levels within the burrowed layer. For convenience, we imagine a layer with thickness dz at a fixed distance below the mixed layer. At any instant this layer 1) will receive ^{14}C because of the push of sedimentation, 2) will lose ^{14}C for the same reason, 3) will lose ^{14}C because of

decay, 4) will receive ^{14}C because of burrowing, and 5) will lose ^{14}C for the same reason. Since we are assuming a steady state, these gains and loss sum to zero:

$$s \frac{dc}{dz} dz - dcdz + \frac{b}{Z_1} c_{ML} dz - \frac{b}{Z_1} c^* dz = 0.$$

Here c is the concentration of ^{14}C at depth z in the burrowed layer, c_{ML} is the concentration in the mixed layer, and c^* is the concentration in the unburrowed material in the burrowed layer:

$$c^*(z) = c_{ML} e^{d(z+z)/s_0}$$

As before, $z=0$ at the surface and $z<0$ below. Substituting this in the equation for mass balance, we get the differential equation which describes how c varies with depth:

$$\frac{dc}{dz} - \frac{d}{s_0} c = -\frac{b}{s_0 Z_1} c_{ML} (1 - e^{d(Z+z)/s_0}).$$

The boundary condition is that $c(Z)=c_{ML}$. We solve this equation and calculate $\frac{1}{d} \ln(c_0/c)$ to find the ages in the burrowed layer:

$$t_{BL} = \frac{-1}{d} \ln \left\{ \left(1 + \frac{b(Z+z)}{s_0 Z_1} - \frac{b}{d Z_1} \right) e^{d(Z+z)/s_0} + \frac{b}{d Z_1} \right\} + t_{ML}.$$

Fig 2.6 shows what a typical ^{14}C record of the burrowed layer might look like. Notice the steepening of the apparent sedimentation rate near the bottom of the layer. This is a reflection of the increased density of burrows at this level. Levels a few cm below the mixed layer are not affected even at high burrowing rates.

The maximum burrowing rate in the model is $b=s_0$. At this rate,

REPORTED AGE MINUS MIXED LAYER AGE (kyr)

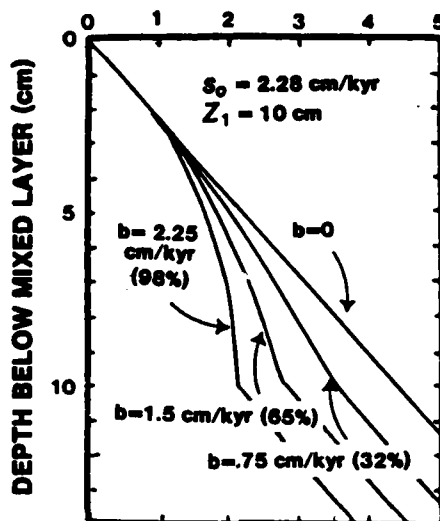


Fig 2.6. Hypothetical ^{14}C ages in the burrowed layer. This layer extends for 10 cm below the bottom of the mixed layer. The calculations assume that the mixed layer thickness, Z , is 8 cm and that the accumulation rate, s_0 , is 2.28 cm/kyr. Various possible burrowing rates, b , are shown; the ratio b/s_0 is in parenthesis.

burrows at the bottom of the burrowed layer are touching; any further increase in the burrowing rate would cause burrows to intersect at this level, in violation of one of our original assumptions. Actually, we should expect burrow intersections well before this saturation density. For this reason, the slope changes shown are likely to be more excessive than reality.

The age of the mixed layer also follows from a mass balance equation:

$$s_o c_o dt - s_o c_{ML} dt - dZ c_{ML} dt + b c_b dt - b c_{ML} dt = 0.$$

Here c_b is the ^{14}C concentration in material brought up by burrows. Since we have assumed that burrows do not intersect, c_b is the average of c^* from Z to $Z+Z_1$:

$$c_b = \frac{s_o c_{ML}}{dZ_1} (1 - e^{-dZ_1/s_o}).$$

Solving the mass balance equation algebraically gives the age of the mixed layer:

$$t_{ML} = \frac{-1}{d} \ln \left[1 + \frac{dZ}{s_o} + \frac{b}{s_o} - \frac{b}{dZ_1} (1 - e^{-dZ_1/s_o}) \right]$$

Fig 2.7 shows how a typical mixed layer might react to deep-burrowing. At modest burrowing rates, say, $b/s = .3$, and reasonable burrow lengths, say, 12 cm below the mixed layer, the mixed layer age increases ~500 yr.

6. Summary and conclusions

This chapter has shown that signal reconstruction is straightforward in theory but intimidating in practice. From a theoretical viewpoint we have seen the following:

- (1) Leaks, fragmentation, and horizontal influx can change the "time" constant of mixing.

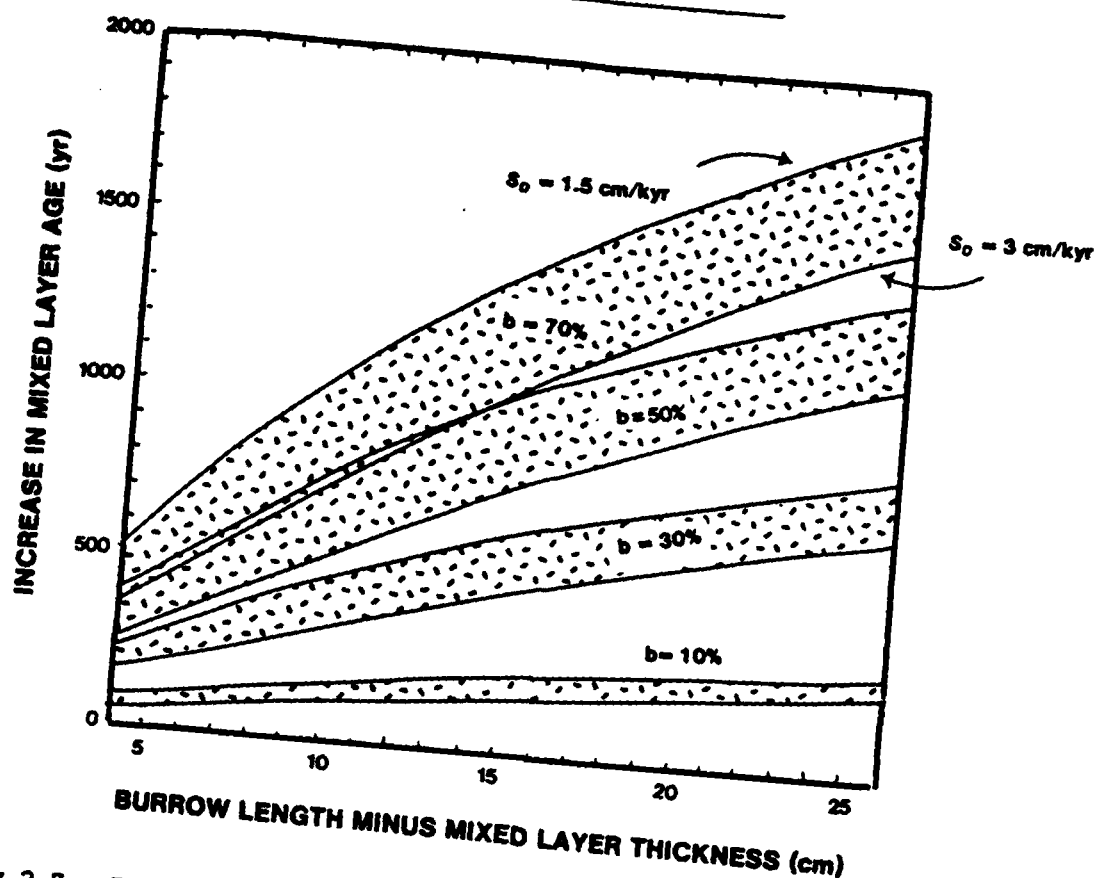


Fig 2.7. Effect of deep-burrowing on mixed layer ages. The burrowing rates, b , are shown as a percentage of the accumulation rates, s_o . These latter range in the figure from 1.5 cm/kyr to 3 cm/kyr.

- (2) Dating reconstructed events is simply a matter of subtracting from reported ages the contemporaneous mixed layer ages. In general, dating with bulk sediment is better than dating with a particular size fraction, no matter what fraction the signal is in.
- (3) The ^{14}C age of the mixed layer under the simplest conditions is a function only of pelagic sedimentation rate, even in the pres-

ence of dissolution, winnowing, and horizontal influx. When the latter effects are present, the reported accumulation rates down core may differ from one core to another but not the age of the mixed layer.

- (4) However, dissolution does tend to make the mixed layer younger and winnowing does tend to make it older. These effects should be especially apparent in cores of low (50%) carbonate or when dating coarse fraction.
- (5) In cores where mixing rates are relatively low ($\sim 8 \text{ cm}^2 \text{ kyr}^{-1}$), we can reconstruct the original signal by adding a term which includes the second derivative of the observed signal. At even lower rates, we add higher derivatives.
- (6) Even at modest levels of activity, deep burrowing can change the ^{14}C age of the mixed layer by 500 yr.
- (7) Even when nearly every cm^3 of the historical record is deep-burrowed, the ^{14}C record can show a mixed layer with a sharp boundary; however, in this case, we might expect a second layer deeper down which appears homogenized.

From a practical viewpoint, we have seen that:

- (8) To fully reconstruct a signal, we must know to a high precision the degree of dissolution, winnowing, horizontal influx, and fragmentation.
- (9) Precisely reconstructing events recorded in sediment mixed at relatively low rates (less than, say, $G=1$) may be beyond the current state-of-the-art in instrumentation.

CHAPTER 3

SAM: A PRECISION STRATIGRAPHER

1. Capabilities

This chapter describes a machine I built to identify and measure the shells of planktonic foraminifera automatically. It presently processes 7000 shells per day and has an ultimate capability of about 40,000 shells per day. Even at its present processing rate it can provide a signal precise enough for signal reconstruction at 1-cm resolution. This chapter lists the machine's capabilities, describes its hardware and software, and explains its calibration.

The machine (Sam: System for automatic micropaleontology) has the following capabilities at present:

Species recognized	Sam recognizes 10 species and 3 classes of fragments; it also distinguishes between <u>Globigernoides sacculifer</u> trilobus and <u>G. sacculifer</u> sacculifer. All species are tropical or equatorial and only defined for the 355-840 μ fraction.
Processing rate	Sam identifies, measures, and catalogs one shell in about 10 seconds.
Capacity	Sam can count over 100,000 shells without human intervention except to change the disk cartridge every 37,000 shells.
Recognition efficiency	For the average species, 45% of scanned shells are correctly recognized; 55% are either not recognized or recognized incorrectly. (All species are weighted equally in this and the following average).

Error rate	For the average species, 20% of recognized shells are recognized incorrectly.
Loading efficiency	15% of shells loaded are never viewed.
Viewing efficiency	15% of viewed shells are out of the TV frame and Sam attempts no identification.
Physical sorting capability	Sam can mechanically isolate one class of shell.
Measurement capability	Resolution is 1 TV pixel. This equals about 3 microns when Sam is set for the 355-840 micron class. For all species, Sam files 6 basic measurements. In addition, it files 5 or more measurements particular to any given species. At the push of a button, an operator may use a cursor to measure and have filed any dimension of the outline of the shell currently being viewed.

As can be seen, Sam is very inferior to a trained human in species recognition. It excels, however, in objective measurements and is tireless.

A large error rate, like that shown above, is not as important as it might seem. Calibration can compensate for much of the error. In practice, calibration is merely a matter of sitting down with Sam for a few days and specifying to the machine the true identity of each shell as it comes by. We discuss calibration in detail in the last section of this chapter.

The main consequence of errors is inefficiency. It is possible to improve efficiency by more extensive programming. A more productive alternative, though, may be to substitute newer and faster electronics into the system. With faster electronics, the ultimate throughput of the machine is probably less than 2 seconds per shell, or 40,000 shells

per day.

2. How the hardware works

In terms of hardware, Sam consists of a minicomputer system, a video digitizer, a TV camera, and a framing mechanism. The framing mechanism projects the images of shells one by one onto the faceplate of the camera. The video digitizer converts the voltage signals from the camera into digital values of light intensity. The computer controls the digitizer and the framing mechanism. It also converts a half-million intensity values into a species name and a shell's dimensions.

2.1. The framing mechanism

Figure 3.1 shows two views of the framing mechanism. In what follows, integers in parenthesis refer to parts labelled in the figures. The mechanism works like this: An intermittent stream of shells (4) falls onto the apex of a cone (12). The cone splits the stream into a circle of shells. A narrowing gap (17) constrains the circle into a thin line. The shells drop onto the flat side of a wheel (13), possibly glass. A motor rotates the wheel [via a speed reducer (34)] so that shells move into the view of a microscope one by one. A vacuum continuously cleans the wheel.

Mirrors provide several views of each shell. A wheel (41) holds some mirrors (39). Others (43) sit at the side of or below the wheel on which the shells lie. A motor (18) rotates the mirror wheel to give consecutive views of different sides of each shell. Figure 3.2 shows the geometry of the mirrors. The mirrors can provide a top view,

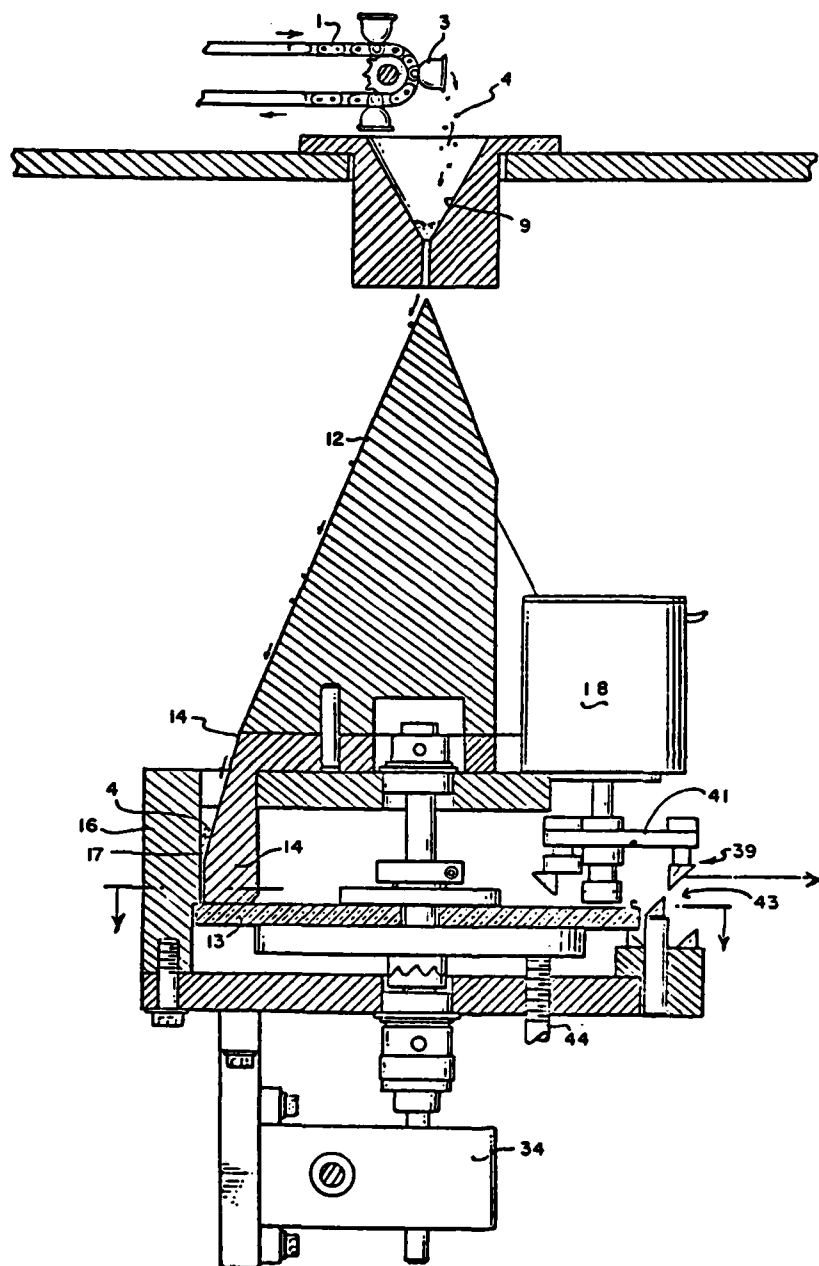


Fig 3.1a. Side view of the framing mechanism. This figure and Figs 3.1b, 3.2, and 3.4 are from a patent application prepared by the Office of Naval Research under the direction of P.N. Critchlow.

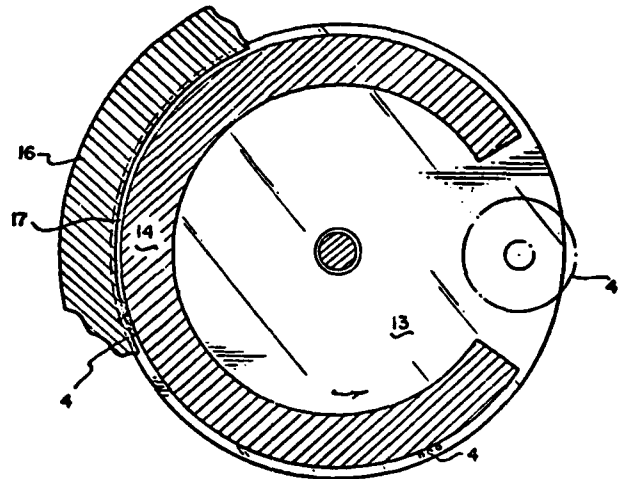


Fig. 3.1b. Horizontal section through framing mechanism. Plane of section is indicated by heavy lines with arrows in Fig 3.1a.

a front view, a back view, and a bottom view . The latter view requires that the wheel (13) holding the shells be glass. The angle of view of the microscope governs the size of the mirrors. The mirrors used are 45 degree prisms silvered on the hypotenuse. Because the present identification program (see below) only relies on shell outlines, the machine at present uses only the top and front views.

A chain (1) of small buckets (3) provides the intermittent stream of shells to the cone (12). A motor turns the chain and so dumps

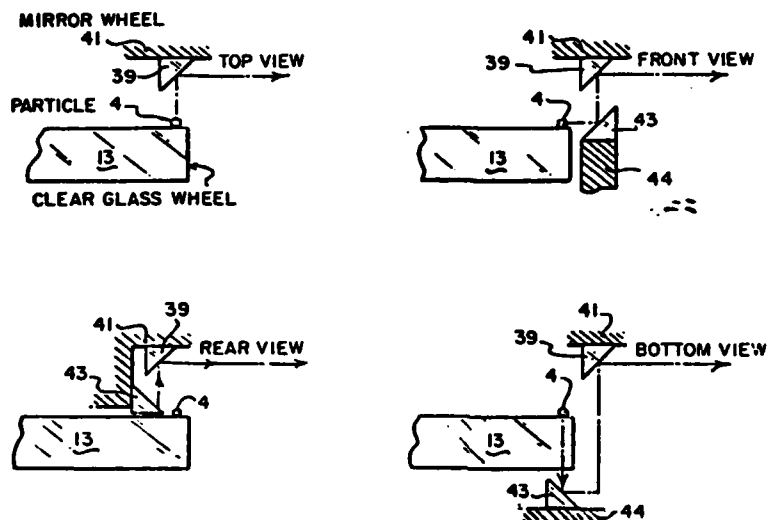


Fig 3.2. Mirror geometry looking from the side with microscope to the right. Only the top mirror needs to be moveable.

40 or so shells from a bucket through a funnel (9).

The wheel (13) onto which the shells fall can move up or down a small distance. A screw (44), turned by the focus motor (see below), raises and lowers the wheel (13). When up, the wheel seals the shell-trapping gap (17) from below. Once a bucket has dumped its load, the wheel lowers, so that shells cannot touch the sides of the trapping gap (17). An exchangeable sizing plate (14) fixes the width of the gap. The cylindrical main plate (16) serves as the outer wall of the gap.

2.2. From image to digital intensities

The image reflected from the mirrors travels through a microscope and onto the faceplate of a TV camera. From there the image makes its way into the computer via the video digitizer. The microscope consists of the objective lens and focus mechanism of a Wild M5. The distance from the microscope to the camera controls the magnification. A motor focuses the microscope for each mirror view. (This motor also serves to raise and lower the wheel holding the shells.)

The TV camera is an RCA TC 1005/01. The company claims a horizontal resolution of 800 lines and a distortion of less than 2%. The camera scans 480 vertical lines in a 2:1 interlace. The signal to noise ratio of the voltage output is about 10:1. (Because of this noise level, a single scan of a shell cannot resolve a shell's texture. This is the main reason we use shell outlines for identification.)

The video digitizer is Model 270 made by Colorado Video, Inc. Horizontal resolution is 512 points. The digitizer works like this: The user provides two numbers, x and y, which address a particular point on the camera faceplate. When the camera's beam traverses that point, the digitizer converts the TV output voltage to a number, z. This number is proportional to the intensity of light at x,y. Two potentiometers on the digitizer allow the user to set the black level ($z=0$) and the white level ($z=255$).

The black and white levels are important. Changing these levels changes the outline of a shell and so can change shell identification. This, in turn, changes Sam's calibration.

Likewise, shell lighting is important. The lighting arrangement we use appears in Fig 3.3. The intent is to provide a high contrast between the shell, which is white, and the background which is dark. This is not as simple as it seems. The wheel upon which the shells sit is the background for the top mirror view. If this wheel is smooth, a reflected image of the current shell appears in side views. If the wheel is rough, specular reflections appear in top view. Currently, we use an aluminum wheel, sandblasted and painted flat black.

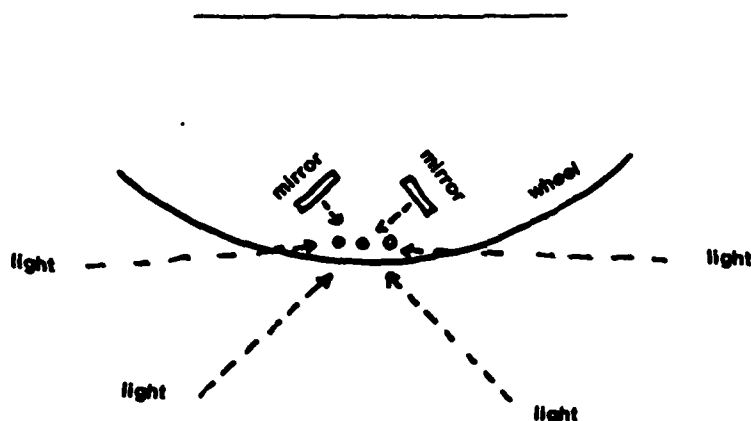


Fig 3.3. Lighting arrangement, looking down.

3. How the software works

The minicomputer system controls the other hardware and identifies and catalogs the shells. It continuously cycles between three programs: a control program, an analysis program, and an identification program. The first two are of a general nature; the identification program is particular to species present in the western equatorial Pacific during the Quaternary. To use Sam where other species dominate, you

must write additional identification subroutines. It is possible that you may want to write additional analysis subroutines, too, but it is unlikely that you will want to change the control program. This is fortunate because the control program is complex and is written in Assembler and microcode for speed and conciseness. However, it is important to understand the control program; by its nature it introduces biases into the counts of species and statistics of measurement. Such biases may not fully be compensated by calibration.

3.1. Control program

Figure 3.4 shows the flow of information in the machine. The control program drives the video digitizer, 4 stepping motors, and an air valve, based on previous information. The program also converts a map of image intensity into shell outlines. This latter process is of little concern here; it is more or less bias free. It works by searching the image for edges and then logically arranging the edges into arrays of connected points. These connected points it passes to the analysis program as the outline. One source of grief for the analysis program is that these connected points are not equally spaced: vertical and horizontal lines, no matter what their length, are described only by endpoints; lines 45 degrees to the horizontal have one point for every pixel.

Other parts of the control program may contribute bias. To see this, consider how the program works: The wheel holding the shells makes one revolution. As the wheel revolves, the computer scans the leftmost edge of the TV frame. The TV camera, meanwhile, is looking down on the

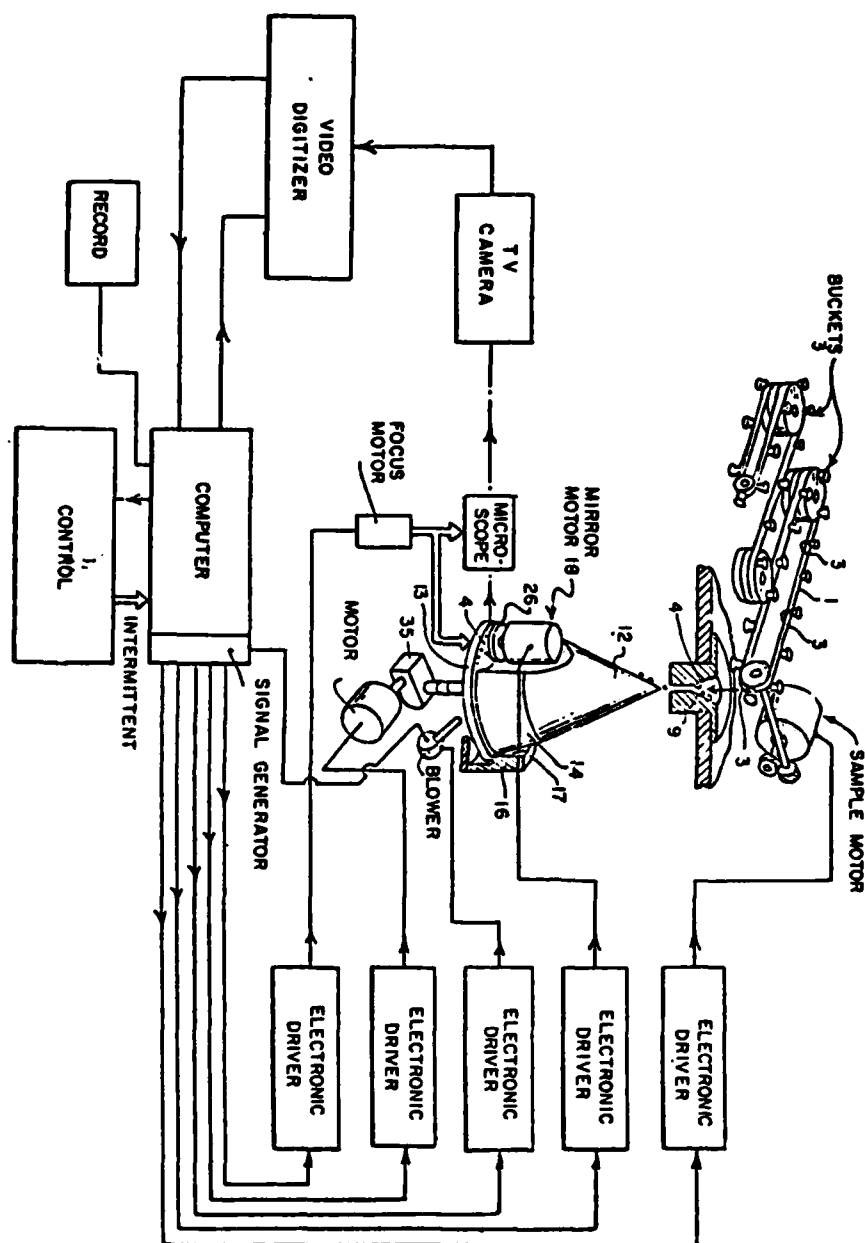


Fig 3.4. Flow of information.

wheel and sees the surface of the wheel moving left to right. When a white image crosses the leftmost edge, the computer stops the wheel with

the image more or less centered in the frame. The full frame is then scanned. If there are one or more shells completely in the frame, if memory has not overflowed, and if no shells will overlap in a front view, the computer changes the microscope focus point, steps the front view mirror into position, and scans this view fully. If the count and position of "good" shells in the front view matches that of the top, the computer returns the mirror wheel to the top view and starts the analysis program and then the identification program. On return from these programs, the computer starts the wheel moving to search for the next shell.

Once a wheel revolution is complete, an air valve comes on to blow off any shells not picked up by the vacuum system. This done, the computer raises the wheel to seal the trapping gap. It then steps the sample motor to dump a few shells from the current sample bucket. The number of steps it takes depends on the number of shells detected on the last revolution: if too many shells, the motor takes fewer steps than last time; if too few shells, the motor takes more steps than last time. The program considers 40 shells optimum. Once the dumping is complete, the computer lowers the wheel and starts searching for shells as before.

There are at least 5 sources of possible bias in this control program:

- (1) The computer rejects shells that are out of frame. These shells may not be a representative sample. Shells may be out of the frame for one of three reasons: they fell through certain leaks in the trapping gap during dumping; one shell landed on top of

another during dumping and during lowering of wheel rolled out of frame; and the start and stopping of the wheel during search rolled them out of frame. The first of these reasons is probably bias free. The last two may be sensitive to shape and size.

- (2) The computer rejects shells that overlap in front view. This process depends on the size of the trapping gap and the size of the shells. Two large shells are not likely to overlap; nor are two small ones.
- (3) Shells can touch one another. If they fit in the frame, the computer will scan them. If not, it will reject them. Clearly, this process depends on the ability of at least one of the touchers to roll. The identification program can detect some of the touchers and so some of the bias, if present, can be removed by calibration.
- (4) Memory overflow during scanning is size dependent. Texture and shadows also play a role.
- (5) The search of the wheel may miss shells of low contrast.

To test for these possible biases, I counted species in the first four of these types of rejects (the fifth type was too rare to count). The bias was not serious. Globorotalia menardii did seem slightly enriched in the rejects (especially specimens over a millimeter long).

This experiment did not test for bias in size. However, since

the various species have different mean sizes, their minimal bias suggests only minimal bias in size.

3.2. Analysis program

The analysis program receives from the control program two closed curves, namely, a shell's outline in top view and in side view. The program's job is to characterize these two closed curves by a list of traits. The identification program (described shortly) uses only this list to classify the shell. The list includes such measurements as maximum, minimum and mean diameter, height, and maximum curvature. It also includes the results of a more discriminating analysis.

This latter analysis is one of fitting circles to segments of the outlines. Circles fit the outlines because planktonic foraminifera grow by adding more or less hemispherical chambers. [In fact, Berger (1969) has exploited this rather simple geometry to speculate on the ecologic meaning of the various morphologies. Similar thinking had been done earlier by Thompson (1917), who gave a description of the geometry that results when growth is by similar but increasing increments: The result is a form that follows a logarithmic spiral. Planktonic foraminifera are without exception by nature three-dimensional logarithmic spirals. Actual taxonomy, however, is based more on surface texture than morphology (Parker, 1962)].

The three-dimensional nature of the foraminiferal shell complicates identification by outline. For some species the character of the outlines from the side and top view depend on the orientation of the shell in front of the TV camera. Other species -- for instance, those

which are flattened -- always lie with a certain side up or down. One way to process shells of the first group is to include programming which recognizes all possible orientations. Another way is to recognize only one orientation and then later measure the probability of the one orientation. This is the approach we take.

3.2.1. Chamber detection and circle-fitting

The analysis program fits an outline with circles by first detecting sutures between chambers and then forcing circles through the suture points. A "suture" is the curve in three dimensions along which the animal attaches a new chamber to its shell. In the outline of a shell, sutures appear as sudden changes in the tangent angle.

The program detects sutures by filtering the outline for high frequencies. The "high-pass" version of an outline shows peaks at sutures. The program does the filtering by subtracting, in a vector sense, a running mean of the outline from the outline itself. It assigns a sign to the magnitude of the vector difference, depending on whether the mean is inside (-) or outside (+) the actual outline. Sutures result in positive peaks in the high-pass version.

Once the program has detected the sutures, it fits circles through these points with the constraint that the area of the protruding part of the circle equal the area of the protruding part of the chamber. In more explicit terms, it first calculates the chordlength, s , as the distance between the two relevant sutures. It then calculates the area of the protruding part of the chamber by integrating along this chord. If θ is the angle subtended by the chord in the circle we seek, then the

area between the chord and the circle must be

$$A = \frac{\theta s}{8 \sin^2 \frac{\theta}{2}} - \frac{s^2}{4} \cot \frac{\theta}{2} .$$

From a precalculated table, the program finds θ from its calculation of A. The radius, r , of the fitted circle follows from the formula for chordlength: $s = 2r \sin \frac{\theta}{2}$. The position of the center of the circle is a distance r along the perpendicular to the chord.

The advantage of using the chordlength and intercepted area in these calculations is that they use all the data points on the outline. (The chordlength is a vector sum of all the sampled arclengths). In this sense, the resulting circle is a "best" fit.

Appendix 1 gives an example of the analysis of one specimen for each of the species Sam can recognize (except for Globigerina calida, whose identification subroutine needs improving). The examples show the circle fittings and list the traits which the identification program relies upon for discrimination. A key to the examples appears at the head of the appendix.

3.3. Identification program

Table 3.1 shows the essential distinctions of each species so far coded. The identification program listing, which appears in Appendix 2, documents the actual distinctions used for this report. Details of the program logic can be found in the comments included with the listing.

species	code	abbreviation
unspecified or unknown	0	unk
<u>Orbulina</u> <u>universa</u>	1	Orb
<u>Pulleniatina</u> <u>obliquiloculata</u>	2	Pul
<u>Globoquadrina</u> <u>dutertrei</u>	3	dut
<u>Globigerinella</u> <u>aequilateralis</u> (normal form)	4	naeq
<u>Globigerinoides</u> <u>sacculifer</u> <u>trilobus</u>	5	tri (sac)
<u>Globigerinoides</u> <u>sacculifer</u> <u>sacculifer</u>	6	sacsac (sac)
<u>Globorotalia</u> <u>menardii</u>	7	men
<u>Globorotalia</u> <u>tumida</u>	8	tum
<u>Globoquadrina</u> <u>conglomerata</u>	9	cgm
<u>Globigerinoides</u> <u>conglobatus</u>	10	cgb
<u>Globigerina</u> <u>calida</u>	11	cal
<u>Globigerinoides</u> <u>aequilateralis</u> (kummerform)	12	kaeq
<u>Globigerinoides</u> <u>ruber</u>	13	rub
fragment	14	frag
two shells touching	15	tch

Table 3.1a. Species names, codes and abbreviations.

4. Calibration

4.1. Method

Correction for mis- and non-identification is achieved as follows:

Let n_j , for $j=0 \rightarrow 15$, be the true number of shells of species j present in a sample. See Table 3.1 for species names corresponding to numbers. Let N_i , for $i=0 \rightarrow 15$, be the number of shells (in the same sam-

<u>species</u>	<u>essential trait(s)</u>
<u>code</u>	
0	doesn't fit any coded description
1	spherical
2	shallow sutures, more or less spherical dimensions
3	5-7 chambers about the same size, shell flattish
4	4-6 chambers of steadily increasing size
5	3 major chambers, deep sutures, last chamber much larger and more lobate than second to last
6	has a trilobate form embedded within its outline
7	flat but has rounded chambers in the top view
8	like <u>G. menardii</u> but thicker
9	3-4 chambers of intermediate lobateness
10	3-4 chambers, one of which is flattened
11	like <u>G. aequilateralis</u> but more lobate
12	like normal form except that last chamber is smaller than 2nd to last
13	less than 500 μ maximum diameter, 3 chambers, last of which is smaller than 2nd to last
14	2 chambers; or circular in top view and not circular in side view; or very sharp corners and no embedded trilobate <u>G. sacculifer</u> or unusual height/width, width/length ratios
15	2 very deep sutures

Table 3.1b. Species currently identified by Sam and their distinctions. See Table 3.1b for species and their codes.

ple) which Sam calls species i . Let p_{ij} be the fraction of species truly j called by Sam species i . Then, obviously,

$$N_i = \sum_{j=0}^{15} p_{ij} n_j, \quad i=0 \rightarrow 15 \quad (3.1)$$

In actual samples we seek n_j ; Sam provides N_i . We calibrate Sam to get p_{ij} .

During calibration, as each shell appears on the TV monitor, we key in true species identification simultaneously with Sam's identification. The size of the sample simultaneously counted presumably governs the precision of the calibration. If c_{ij} is the count of species truly j called by Sam i , then p_{ij} is merely c_{ij} divided by the total count.

Given these p_{ij} from calibration, we can find the n_j for actual samples by solving the 16 versions of eq (3.1) simultaneously. However, due to errors in p_{ij} , a stabler solution results from replacing the 0th version of eq (3.1) with $N = \sum_{j=0}^{15} n_j$, where N is the total number of shells in the sample. Sam's count of unknowns, N_0 , is always a large fraction of the total.

The machine's measurements -- mean diameter, number of chambers, and so on -- are also affected by mis-identifications. Let M_i be the mean of a measurement which Sam made on shells (in a given sample) which it called species i . Let m_j be the mean of this measurement on shells in the same sample which are truly species j . Then

$$M_i = \sum_{j=0}^{15} \left[\frac{p_{ij} n_j}{N_i} \right] m_j, \quad i=0 \rightarrow 15. \quad (3.2)$$

In other words, M_i is a weighted average of the true mean measurements; the weights are $a_{ij} = \frac{p_{ij} n_j}{N_i}$, the fraction of shells in a given sample which are truly species j but which Sam called species i .

Eq (3.2) assumes that mis-identifications and measurements are independent. The equation would not hold if, for instance, the

measurements are of mean diameter and Sam mistakes only the small individuals of species 1 for species 2. But as long as the assumption holds, we can solve the 16 versions of eq (3.2) simultaneously to find the m_j . In practice, for stability, we ignore the case $i=0, j=0$.

Problems arise when Sam makes species specific measurements. In some of these cases, Sam may not provide the M_i for all the species which are misidentified as one another. Uncompensateable error results. This is one argument in favor of minimizing species cross-talk by increasing the count of "unknowns," even at the expense of signal attenuation.

4.2. Example: calibration for the Quaternary in the western equatorial Pacific

Table 3.2 shows the calibration I did for the cores in Chapter 4. This table gives the combined p_{ij} (in parts per thousand) for two samples from core ERDC 79. One sample was from 4-5 cm and the other was from 33-34 cm.

As a matter of peripheral interest, Table 3.2 includes the p_{ij} for 5 categories of shells which Sam does not distinguish:

- 16 = Pulleniatina obliquiloculata without shiny coating
- 17 = Sphaeroidinella dehiscens
- 18 = Globorotalia crassaformis and G. truncatulinoides
- 19 = G. scitula and G. hirsuta
- 20 = Candeina nitida

Shells with $j=16$ are also included in $j=2$; $j=17$ to 20 are also included in $j=0$.

The diagonal p_{jj} in Table 3.2 gives the percentage which Sam

TABLE OF P_{ij} ERDC 79
TOTAL COUNT 18765

		SAMI'S IDENTIFICATION															
	J	I = 0	1	2	3	4	5	6	7	8	9	10	11	12	13	14	15
J	0	350	757	0	154	11	3	0	9	6	3	17	0	6	0	17	11
R	1	154	6	753	240	0	0	0	0	0	0	0	0	0	0	0	0
T	2	5999	196	4	753	0	0	0	0	0	3	2	0	0	0	0	0
U	3	655	456	0	1	357	26	0	12	0	0	5	14	3	124	0	1
E	4	1359	304	0	2	4	505	2	12	0	1	4	3	2	134	1	25
X	5	1390	349	0	5	0	1	555	68	0	0	1	0	5	0	3	5
I	6	1269	549	0	1	5	2	20	348	1	0	2	2	50	9	0	10
D	7	1001	227	0	0	0	0	0	3	740	24	0	0	0	0	0	5
	8	600	505	0	0	0	0	0	7	17	448	0	0	0	0	0	20
	9	538	656	0	30	2	0	0	0	0	4	256	52	0	0	0	0
	10	785	583	0	89	11	4	1	2	0	0	22	278	0	2	0	0
	11	71	540	0	0	0	14	0	225	0	0	0	0	113	42	0	28
	12	480	356	0	2	31	23	0	15	0	0	6	0	12	546	0	2
	13	290	755	0	3	0	7	31	24	0	0	0	28	7	0	138	7
	14	3292	798	0	51	2	2	4	5	3	9	7	1	2	6	0	97
	15	512	78	0	2	0	0	0	4	0	0	0	0	0	0	0	0
	16	467	323	4	662	0	0	0	0	0	0	0	0	0	0	0	0
	17	117	752	0	239	0	0	0	0	0	0	0	0	0	0	0	0
	18	126	770	0	175	0	0	0	0	0	0	0	0	0	0	0	0
	19	35	914	0	0	0	0	0	29	29	29	0	0	0	0	0	0
	20	13	846	0	77	77	0	0	0	0	0	0	0	0	0	0	0

95% CONFIDENCE LIMITS FOR P_{ij}

J	I	0	1	2	3	4	5	6	7	8	9	10	11	12	13	14	15
0	42	0	34	10	5	0	8	14	10	5	12	0	7	0	14	11	
1	13	68	67	0	0	0	0	0	0	0	0	0	0	0	0	0	
2	10	2	10	1	0	0	0	0	0	1	1	0	0	0	0	1	0
3	38	0	3	37	12	0	8	0	0	5	9	4	25	0	3	0	0
4	24	0	2	3	27	2	6	0	1	4	3	2	18	1	8	1	
5	25	0	4	0	2	26	13	0	0	1	0	4	0	3	4	3	
6	27	0	2	4	2	8	26	2	0	2	3	12	5	0	5	0	
7	26	0	0	0	0	0	3	27	9	0	0	0	0	0	4	2	
8	40	0	0	0	0	0	7	10	40	0	0	0	0	0	11	5	
9	40	0	14	4	0	0	0	0	5	37	19	0	0	0	0	0	
10	36	0	22	7	4	0	0	0	0	11	33	0	4	0	0	0	
11	116	0	0	0	27	0	97	0	0	0	74	47	0	39	39	0	
12	43	0	4	16	13	0	11	0	0	7	0	10	45	0	8	0	
13	49	0	7	0	10	20	18	0	0	0	19	10	0	40	10	0	
14	14	0	8	2	2	2	3	2	3	3	1	1	3	0	10	4	
15	23	0	4	0	0	0	5	0	0	0	0	0	0	0	25	33	

Table 3.2. Table of P_{ij} and their confidence limits for ERDC 79. Values are in parts per thousand. Second column is number of shells of species j (n_j). See Table 3.1 for species codes, except for $j=16$ to 20, for which refer to the text.

named correctly. The average p_{jj} is about 45%. Notice also that p_{0j} (what Sam calls unknown) is about 42% on average. Thus, signal attenuation is quite large, especially for fragments ($j=14$), Globigerinoides ruber ($j=13$), and Globoquadrina conglomerata ($j=9$).

The amount of cross-talk, $\sum_{j=0}^{15} p_{ij} n_j$, for $i \neq j$, depends on actual

species abundances. In Table 3.2, n_j appears in the second column. From these numbers, you can see that cross-talk is for the most part minor but that there are exceptions: Globigernoides sacculifer ($j=6$) (non-trilobate form) dominates Globigerina calida ($i=11$) in Sam's counts of the latter (N_{11}). Several species inadvertently contribute to the fragment category (N_{14}). Also, Sam calls a significant number of Globoquadrina dutertrei ($j=3$) Globigerinella aequilateralis (kummerform, $i=12$). The apparent cross talk between the normal form of G. aequilateralis ($j=4$) and the kummer form ($i=12$) may not be real; my distinctions between the two were subjective and may have been occasionally wrong.

An example of the measurement weights, a_{ij} , in parts per thousand, appears in Table 3.3. Note that this table is reversed from Table 3.2; the j are columns and the i are rows. [The size of the a_{ij} also gives some indication of the amount of cross-talk. This is a real sample used in Chapter 4: for safety's sake, I have "turned off" cross-talk from and into Globigerina calida ($i,j=11$) and fragments ($i,j=14$)]. The rightmost column gives the M_i (Sam's mean for species i) for this sample. The true means, m_j , appears at the bottom of the table. In this case, only Globoquadrina conglomerata ($i,j=9$) shows much difference between M_i and m_j . Apparently, crosstalk from the smaller Pulleniatina obliquiloculata ($j=2$) and Globigerinoides conglobatus ($j=10$) brought M_9 down.

4.3. Holocene vs Glacial calibration

As I mentioned, Table 3.2 gives the p_{ij} of two samples combined.

TABLE OF a_{ij}

MAX DIAMETER. ERDC 79. 22.5 CM. REPLICATE 8

J=	0	1	2	3	4	5	6	7	8	9	10	11	12	13	14	15	SAM
0	1000	0	0	0	0	0	0	0	0	0	0	0	0	0	0	0	213
1	0	832	162	0	0	0	0	0	0	0	0	0	0	0	0	0	225
2	0	0	978	0	1	0	0	0	0	1	12	0	0	0	0	0	200
3	0	0	0	10	877	24	0	16	0	0	1	25	0	47	0	0	194
4	0	0	0	0	19	962	2	1	0	0	2	0	10	3	0	0	207
5	0	0	0	2	0	0	8	951	24	0	0	1	0	0	17	0	219
6	0	0	0	0	17	44	158	735	4	5	0	3	0	12	18	0	239
7	0	0	0	0	0	0	0	1	928	11	0	0	0	0	0	0	238
8	0	0	0	5	0	6	0	0	79	908	2	0	0	0	0	0	223
9	0	0	0	145	25	68	7	12	0	0	565	151	0	23	0	0	242
10	0	0	0	83	48	26	0	10	0	0	38	765	0	53	0	0	215
11	0	0	0	0	0	0	0	0	0	0	0	0	0	0	0	0	219
12	0	0	0	0	146	401	0	13	0	0	0	0	3	437	0	0	208
13	0	0	0	0	0	22	52	0	0	0	0	0	0	0	920	0	171
14	0	0	0	0	0	0	0	0	0	0	0	0	0	0	0	0	231
15	0	0	0	0	0	3	11	0	2	3	0	0	0	0	0	0	221 328

SOLUTION

213 221 200 191 208 220 248 205 253 267 218 219 214 167 231 329

Table 3.3. Example of measurement weights, a_{ij} . Data (M_i and N_i) are from an actual sample used in Chapter 4. The necessary p_{ij} come from Table 3.2. Weights are in parts per thousand. Columns and rows are reversed from Table 3.2. Rightmost column gives mean of Sam's measurements. Bottom row labelled "solution" gives "true" value of these measurements, the effects of cross-talk having been eliminated. See Table 3.1 for species codes.

Table 3.4 gives the difference, in parts per thousand, between the p_{ij} of the two samples. The table also gives the 95% confidence limits for the differences based on the count size; i.e., if the confidence limits minus the absolute value of the difference is less than 0, then the difference is significant at the 95% level.

In the table, differences significant at this level are starred. There are 12. This is 5 more than expected (there are 138 non-zero counts). Five which may be truly different are underlined; these differences are largest relative to the confidence limits. Two of these have $j=2$ and three have $j=4$. These differences may partly be the result

HOLOCENE P_{1j} - GLACIAL P_{1j}

J	I	0	1	2	3	4	5	6	7	8	9	10	11	12	13	14	15
0		0	0	0	0	0	0	0	0	0	0	0	0	0	0	0	0
1		12	0	10	2	-4	0	-3	-6	-8	-4	-27	0	-9	0	35	18
2		-2	-23	0	0	0	0	0	0	0	0	0	0	0	0	0	0
3		0	0	-32	0	0	0	0	0	0	0	0	0	0	0	0	0
4		0	0	-15	0	0	0	0	0	0	0	0	0	0	0	0	0
5		0	0	-16	0	0	0	0	0	0	0	0	0	0	0	0	0
6		0	0	0	0	0	0	0	0	0	0	0	0	0	0	0	0
7		0	0	0	0	0	0	0	0	0	0	0	0	0	0	0	0
8		0	0	0	0	0	0	0	0	0	0	0	0	0	0	0	0
9		0	0	0	0	0	0	0	0	0	0	0	0	0	0	0	0
10		0	0	-24	-13	0	0	0	0	0	0	0	0	0	0	0	0
11		0	0	-47	-15	0	0	0	0	0	0	0	0	0	0	0	0
12		0	0	0	0	0	0	0	0	0	0	0	0	0	0	0	0
13		0	0	0	0	0	0	0	0	0	0	0	0	0	0	0	0
14		0	0	0	0	0	0	0	0	0	0	0	0	0	0	0	0
15		0	0	0	0	0	0	0	0	0	0	0	0	0	0	0	0

95% CONFIDENCE LIMITS FOR DIFFERENCE

0	85	0	69	20	0	0	17	27	10	0	22	0	13	0	30	24
1	141	140	0	0	0	0	0	0	0	0	0	0	0	0	0	0
2	20	4	81	0	0	0	0	0	0	0	0	0	0	0	0	0
3	40	0	0	83	25	0	18	0	0	0	0	0	0	0	0	0
4	0	0	0	0	7	0	12	0	0	0	0	0	0	0	0	0
5	0	0	12	0	0	0	0	0	0	0	0	0	0	0	0	0
6	0	0	0	12	0	0	0	0	0	0	0	0	0	0	0	0
7	0	0	0	0	0	0	0	0	0	0	0	0	0	0	0	0
8	0	0	0	0	0	0	0	0	0	0	0	0	0	0	0	0
9	0	0	0	0	0	0	0	0	0	0	0	0	0	0	0	0
10	0	0	23	0	0	0	0	0	0	0	0	0	0	0	0	0
11	0	0	48	18	0	0	0	0	0	0	0	0	0	0	0	0
12	234	0	0	0	64	0	200	0	0	0	0	0	0	0	0	0
13	0	0	12	30	33	0	19	0	0	0	0	0	0	0	0	0
14	0	0	13	0	15	40	36	0	0	0	0	0	0	0	0	0
15	0	0	15	3	3	4	5	4	7	0	0	0	0	0	0	0

Table 3.4. Difference between the p_{1j} from ERDC 79, 4-5 cm, and the p_{1j} from ERDC 79, 33-34 cm. Differences are simply one number subtracted from the other (in parts per thousand) and are not relative. Lower matrix gives 95% confidence limits for difference. Differences which are significantly different at the 95% level are starred. Possible meaningful differences are underlined. See Table 3.1 for species codes.

of there being two types of each species, the ratio of which varies with depth in core (that is, from Glacial to Holocene). In the case of $j=2$ (*Pulleniatina obliquiloculata*), one type is coated with a thick layer of calcite and the other (shown as $j=16$ in Table 3.2) is not. Sam calls more of the uncoated type unknown (Table 3.2). The uncoated variety

increases from Glacial to Holocene by a factor of 3. The effect is to increase $p_{0,2}$ (Holocene) by about 1% (and decrease $p_{2,2}$ by the same amount). This still leaves a significant difference in Table 3.4, so there may be other types or factors involved. In the case of $j=4$ (normal form of Globigerinella aequilateralis), there are, according to Parker (1962), at least two types, each of slightly different geometry and slightly different temperature preferences. This may explain the excess differences for this species in Table 3.4, but I did not distinguish between the types of the species during calibration. Another explanation may lie in my subjective distinction between normal form ($i=4$) and kummerform ($i=12$) G. aequilateralis.

4.4. Fragment calibration

Fragment abundance is an important signal, being an indicator of dissolution (Berger, 1973). Sam's biases in fragment counts are shown in Table 3.5. The numbers shown (in parts per thousand) are similar in meaning to the p_{ij} : Each element gives the fraction Sam called species i which were truly fragments of species j . Thus, 23% of the fragments of G. aequilateralis ($j=4$) it calls fragments ($i=14$); 65% it calls unknown. As you can see from the table ($i=14$), Sam is most sensitive to fragments of G. aequilateralis. Sometimes fragmentation does not change the outline of a shell. In such cases, Sam identifies it as a whole shell. These are shown in the diagonal of Table 3.5.

Table 3.5 also gives the true degree of fragmentation for each species in the two ERDC 79 samples. Here degree of fragmentation is (in parts per thousand): number of fragments divided by the number of whole

		FRAGMENTS															
J	9	1-0	1	2	3	4	5	6	7	8	9	10	11	12	13	14	15
1	94	681	74	123	0	0	0	0	21	21	0	0	0	0	0	74	0
2	947	771	0	169	4	0	0	1	4	8	17	1	1	2	0	21	0
3	55	600	0	0	295	36	0	12	0	0	0	0	0	36	0	55	0
4	812	654	0	21	1	54	4	2	0	5	1	1	0	16	0	233	7
5	208	654	0	101	0	5	183	19	0	0	0	0	0	0	0	89	10
6	250	672	0	12	0	4	36	186	0	0	4	4	16	8	0	60	22
7	267	738	0	0	0	0	0	0	105	26	0	0	0	0	0	116	15
8	161	829	0	0	0	0	0	6	12	62	6	0	0	0	0	62	19
9	53	753	0	0	0	19	0	38	0	0	170	0	0	19	0	0	0
10	75	773	0	40	13	13	0	0	0	0	40	107	0	0	0	0	13
11	17	471	0	0	0	0	0	0	0	0	0	0	0	0	0	170	363
12	23	826	0	130	0	0	0	0	0	43	0	0	0	0	0	0	0
13	24	792	0	0	0	0	42	42	0	0	0	0	0	0	23	42	0

DEGREE OF FRAGMENTATION

J=	1	2	3	4	5	6	7	8	9	10	11	12	13
	610	158	84	597	150	194	267	282	90	96	239	48	23

Table 3.5. Fragment calibration. Elements in table are fraction called I by Sam which were truly fragments of species J. Samples are the same as in Table 3.2. See Table 3.1 for species codes.

shells of a given species.. G. aequilateralis shows the greatest tendency to fragment. Keep in mind, however, that all of Table 3.5 is biased by my ability to recognize the original species from the fragment. According to the count, 10% of the 3292 fragments in the two samples I called unrecognizeable; but this is subjective.

5. Summary

This chapter has described a mechanical micropaleontologist with a potential for great precision. It has bias, some of which can be calibrated for and some of which cannot. Experiment shows the latter type to be minor.

Calibration indicates that the machine counts some species

(especially Globorotalia menardii and Pulleniatina obliquiloculata) at a higher efficiency than others. As currently programmed, it is particularly inefficient in counting Globigerinoides ruber, Globigerina calida, Globoquadrina conglomerata, and fragments.

For the most part, at the counting level of the calibration (2 samples, 8000 specimens in one, 11000 in the other), the precision of the machine was at the level of counting error. The existence of phenotypes of certain species may have confused the machine slightly.

CHAPTER 4

BOX CORES FROM ONTONG-JAVA PLATEAU

1. Introduction

Given the theory described in Chapter 2 and the machine described in Chapter 3, can we in fact reconstruct a record at 1-cm intervals consistent with known history? To answer this question, here we examine samples and data from box cores taken during the Eurydice (ERDC) expedition to the Ontong-Java Plateau (T.C. Johnson et al., 1976).

These cores suit our purposes because 1) they are minimally disturbed by the coring process, 2) they contain sediment that is a typical foraminiferal ooze (Berger et al., 1977), and 3) they penetrate through the glacial-Holocene transition, which of all climatic events in the geological record is the best documented on a global scale. Fig 4.1a shows the location of the ERDC box cores. Fig 4.1b shows fathometer profiles of Ontong-Java Plateau.

Actually, this chapter raises more questions than it answers. We will see shortly that 1) the documented record, although the best available, is in fact ambiguous and conflicting, and that 2) local sedimentary processes are very important. The local processes -- whose horizontal scales are unknown -- make detailed stratigraphic reconstructions at 1 cm intervals difficult with the cores and data at hand. One-cm stratigraphy apparently requires a new kind of coring strategy, a strategy which includes replicate cores from relatively small areas.

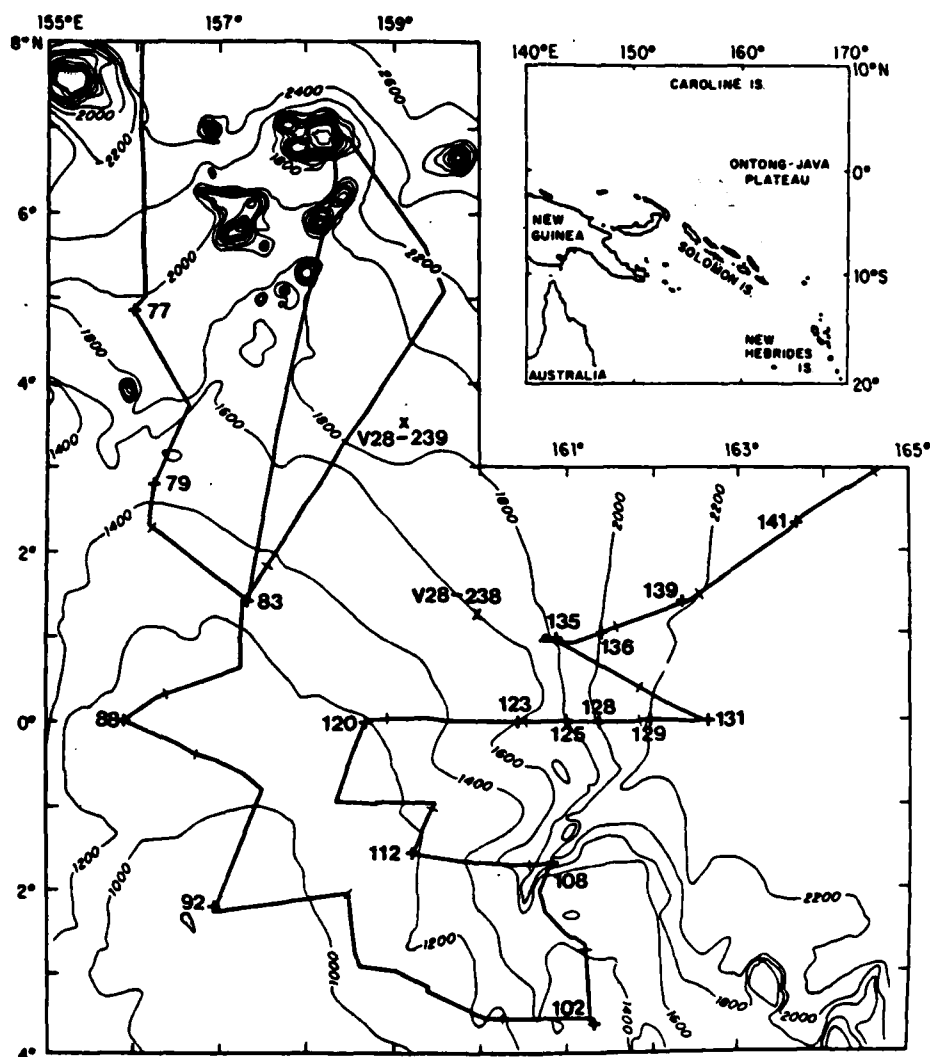
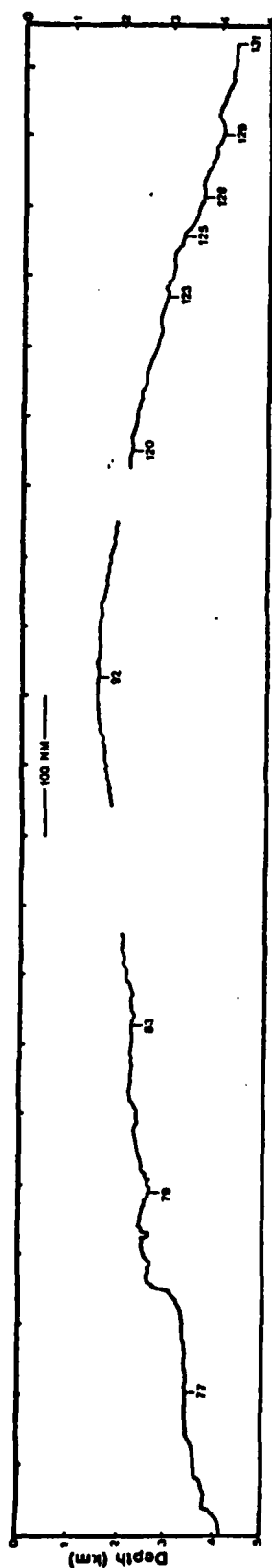
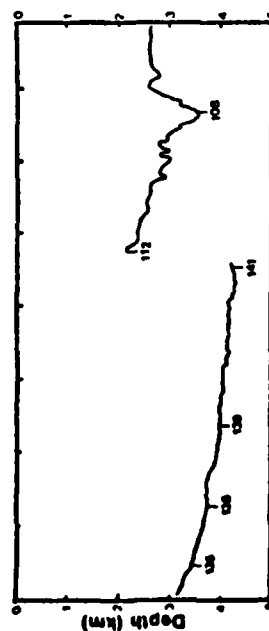


Fig 4.1a. Location of the ERDC box cores. Depths are in fathoms. The figure is from Berger et al. (1977). The map also shows the location of cores V28-238 and V28-239, which are mentioned later in the chapter. The solid meandering line is the ship's track. The profile in Fig 4.1b is along this.



Topographic profiles of Ontong-Java Plateau

Fig 4.1b. Profiles of Ontong-Java Plateau. Profiles are traced from Smith et al. (1975). and are along the ship's track shown in Fig 4.1a. The upper profile starts to the north of ERDC 77. The first break in the profile is at the zig-zag to the west for ERDC 88; the zig-zag is not included. The second break is at the end of the eastward leg following ERDC 92; the profile begins again at ERDC 120, 2° north of the break. The profiles to the left are along the tracks which include the cores shown.



The chapter does demonstrate, however, that the theory elaborated in Chapter 2 is a useful analytical tool and that Sam can indeed track faunal changes.

What follows is organized into 3 parts. In the first part, we discuss briefly the documented record of the glacial-Holocene transition. Our ultimate concern is the western equatorial Pacific, the site of the ERDC cores. However, the transition in this area is poorly documented. We must instead first consider changes elsewhere and then try to extrapolate these to the ERDC area. What information there is on this area is mostly about glacial climate and not about the transition itself. This information is nevertheless relevant because some of the ERDC box cores extend into the glacial.

The second part of the chapter considers the sedimentology of Ontong-Java Plateau. From a unique set of ^{14}C data, we will extract information on mixed layer thicknesses, mixing rates, and sedimentation rates. We will at this point see the importance of local processes. One of several manifestations of such processes is the presence of curious isochronal layers in a number of the cores. We will discuss possible origins for these layers.

The third part of the chapter discusses detailed stratigraphies of several cores. These cores record dramatic changes over the Ontong-Java Plateau: A sudden change in the flux of certain foraminifera occurred more or less simultaneously with an increase in the supply of fresh sediment and a decrease in the rate of carbonate dissolution.

2. Documented record of deglaciation

2.1. Global perspective

The last major deglaciation had a profound effect on the earth: $16 \times 10^6 \text{ km}^2$ of ice melted (Bloom, 1971); sea level rose 130 m (Emery, 1969); sea surface temperature increased globally by an average of 2°C (CLIMAP, 1976); and there were large changes in the sizes of deserts (Sarnthein, 1978) and in the levels of lakes (Street and Grove, 1979). It is not surprising, then, that the record of deglaciation in deep-sea sediment is as pronounced as it is.

As mentioned, we will see in the last part of the chapter that changes at Ontong-Java Plateau were sudden. Climate there apparently shifted from one state to another state in, say, 1000 yrs or less. Was this typical of changes in the rest of the world? In this section, we attempt, among other things, to put these regional changes into a global perspective.

Certain types of change, such as those in ice volume and lake levels, appear to have been gradual. Other changes, such as North Atlantic fauna, are thought to have been sudden. A third type of change — change in carbonate dissolution — is only now beginning to be closely sampled.

Four somewhat independent records of deglaciation appear in Fig 4.2. Three of these are directly related to ice volume. The fourth is perhaps one of the best documented records of changes in atmospheric circulation. The thin solid curve represents ice area as calculated by

F/6 8/7

ONE-CENTIMETER STRATIGRAPHY IN FORAMINIFERAL OOZE: THEORY AND P--ETC(U)

AUG 80 R F JOHNSON

SIO-REF-80-18

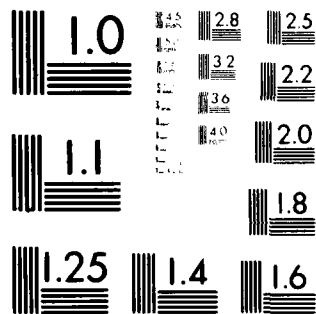
N00014-75-C-0152

NL

UNCLASSIFIED

2 1/3

AD-94-5



MICROCOPY RESOLUTION TEST CHART
NATIONAL BUREAU OF STANDARDS-1963-A

Bloom (1971). The thin dashed curve represents sea level as compiled by Emery (1969). The thick dashed curve is a record of $\delta^{18}O$ from a core in the northeast corner of the Gulf of Mexico (Emiliani et al., 1975). The thick solid curve is from Street and Grove (1978). It shows the proportion of lakes in intertropical Africa at a high stand.

The curves for ice area and sea level in Fig. 4.2 agree surprisingly well, as Bloom (1971) discusses. Ice thickness is more or less unknown, but ice volume should decrease faster than area (Bloom, 1971). Bloom does not show the uncertainty in the curve of ice area. It may be large. The wood and other organic material used for ^{14}C dates is easily transported. Therefore, the age of wood found in a moraine is a minimum age for the moraine. Furthermore, the significance of a given moraine can be misleading if ice retreat is interspersed with ice advance.

Emery (1969) does show the scatter in the sea-level curve. Some of this scatter may be real: sea level did not rise as in a tub; isostasy and gravitational attraction of sea and ice resulted in uneven changes (see, for example, Clark et al., 1978). On the other hand, some of the sea-level scatter may be due to redeposition of the shells, wood, and corals which provide the data for the curve.

The isotope curve in Fig 4.2 is from the carbonate in shells of the planktonic foraminiferan, Globigerinoides sacculifer. (I have subtracted 1000 yr from the reported ^{14}C ages to account for sediment mixing; I have assumed that the mixed layer in the sediment is 10 cm thick; see the nomogram in Fig 2.2; I have not applied eq (2.4) to the isotope curve because the flux ratio, $\frac{n_s}{n_{O_3O}}$, of G. sacculifer is not available;

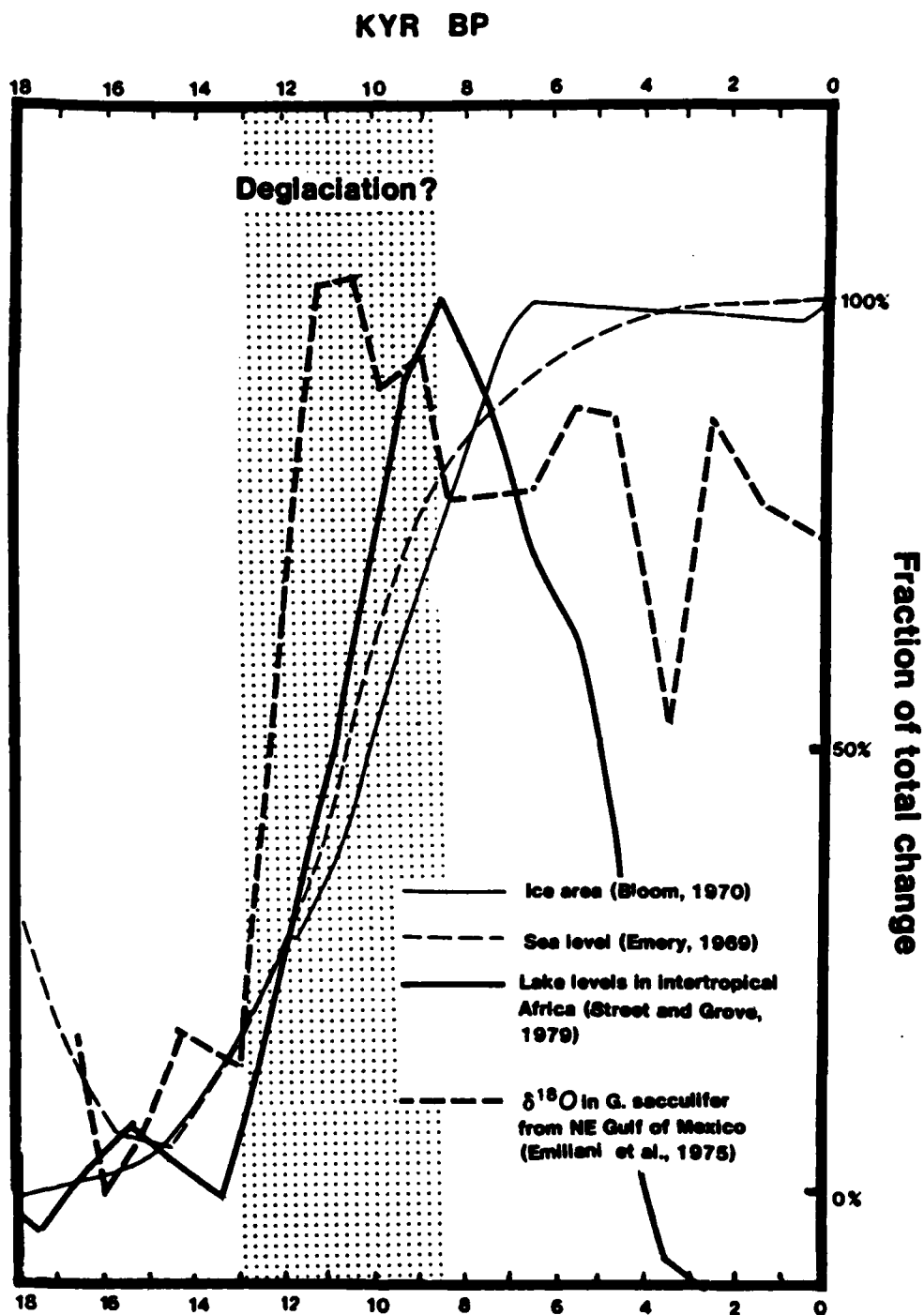


Fig. 4.2. Four records of deglaciation. The abscissa is kyr before present; the ordinate is per cent of the range of variation. Dates shown for the $\delta^{18}\text{O}$ record are 1 kyr younger than given in Emiliani et al. (1975). This is a correction for sediment mixing.

however, at the critical points (13 kyr BP and 12 kyr BP), the curve tends to flatten out, in which case $\frac{dc}{dz} \sim 0$ and $c_0 = c$, barring winnowing, dissolution, and fragmentation]. The curve primarily reflects the oxygen isotope composition of overlying waters.

Two interpretations of the isotope curve are possible (Emiliani et al., 1978). One interpretation is consistent with the published sea-level curve. In this interpretation, sea level rose steadily at a modest rate, say 15 m/kyr. Given the area of the oceans (Sverdrup et al., 1942), we see that this rate of rise is equivalent to a meltwater influx of .15 sv. We now imagine the waters over the core site as being trapped in a well-mixed box. Into the box come meltwaters from the Mississippi River (say, .1 sv). Flushing the box is water from the more or less normal circulation in the Gulf of Mexico. The meltwater has an isotopic composition of -30 ‰ PDB (Dansgaard and Tauber, 1969). The incoming flushing water has a composition of 0 ‰ PDB, as recorded by G. sacculifer before deglaciation begins. Soon after deglaciation begins, G. sacculifer records that the well-mixed box has a composition of -2 ‰ PDB. It therefore follows that the flushing rate must then have been about $(-30/-2)(.1sv) = 1.5sv$. This is not an unreasonable value for shelf water circulation in the Gulf of Mexico (Molinari et al., 1978).

In other words, the first interpretation of the isotope curve is that deglaciation began in earnest at about 13-14 kyr BP. The calculation does not take into account temperature changes in the water but such an accounting would not change the interpretation.

The other interpretation (see Emiliani et al., 1975) is that the

Laurentide ice sheet melted suddenly and a great flood came down the Mississippi. The change at 13-14 kyr BP in the isotope curve would be the beginning of this. Sea level would rise quickly in this interpretation and flushing over the core site would need to be much greater than 1.5sv (Emiliani et al., 1976). Emiliani et al. (1975) give a date of 11.6 kyr BP for the flood. Subtracting 1000 yr for sediment mixing would give a date of 10.6 kyr BP.

The fourth curve in Fig 4.2 tends to support the first interpretation of the isotope data. The change in the number of filled lakes in intertropical Africa appears to have taken several thousand years. Street and Grove (1978) include similar lake data for the southwest US and Australia. (Least contended, though, is the African data). These data from other lakes also show a gradual change. However, like sea level dates, lake level dates show scatter. This would have a tendency to make sudden changes appear gradual. In fact, there is some indication of a sudden change in the lake data: Fig 12 in Street and Grove's paper (p. 97) shows a marked change at about 10 kyr BP in all three geographical areas.

The idea that deglaciation was sudden is not new. One of the earliest applications of ^{14}C dating was dating the deglacial change in planktonic foraminiferal assemblages in the Atlantic and Caribbean (Ericson et al., 1956). The date claimed for this event was 11 kyr BP, which Broecker et al. (1960) considered the point at which climate took a dramatic turn for the better. However, one of the drawbacks of the dates from Ericson et al. (1956) and a similar one from Broecker et al. (1958) is that these workers did not take sediment mixing into account.

Broecker et al. (1960) corrected for mixing somewhat by dating the midpoint of observed changes. Had they dated not the midpoint but the e^{-1} point -- the 63%-point --, they would have indeed accounted for mixing under the simplest conditions. These conditions are: that the change was a step function, that the assumptions of Chapter 2, Section 2, above, were valid, and that dissolution, winnowing, and horizontal influx, if present, affected the sediment at a constant rate. By dating the e^{-1} point under these conditions, they would have in effect subtracted the age of the mixed layer from a date at the beginning of the change. (A better procedure, of course, is to date the beginning of the change in the first place; the additional assumptions of constancy of rates and step-function change are not then necessary). In any case, had Broecker et al. (1960) dated points shallower in core by 13% of the thickness of the change, they would have been, in theory, more nearly correct.

We can correct the date of 11 kyr BP of Broecker et al. (1960) as follows: If the actual change in climate was a step-function, then the thickness of the change should have been about twice the thickness of the mixed layer, Z . Therefore, they dated a point too deep in core by about .26 Z . For $Z=8$ cm and for an accumulation rate of the order of 2 cm/kyr, this translates into an error of about 1000 yr. A date nearer 10 kyr BP for the faunal change in the Atlantic is then more likely. This agrees better with the sudden change in lake levels that the compilation of Street and Grove (1978) provide. However, we should keep in mind that the 1000-yr correction to the date of Broecker et al. (1960) is theoretical. We will see in the last two parts of this chapter that

deep-sea sediment seldom accumulates in a steady, undisturbed fashion. Dating events from widely-spaced cores and at widely-spaced sample intervals does not provide dates of 1000 yr accuracy.

Some of the cores used by Ericson et al. (1956) have a high sedimentation rate. Mixed layer ages should thus be relatively low and the necessary corrections small. The problem with dates from cores of high sedimentation rate is contamination. The process of sedimentation in these cores is usually turbidity currents. Turbidity currents by nature are partly erosive; they thus might easily pick up older carbon. For that matter -- as we will see in the second part of this chapter -- more slowly accumulating sediment can also be contaminated.

At this point, let us summarize what we have seen so far of the documented record of deglaciation. Data for ice area, sea level, and lake levels suggest a gradual transition beginning at around 15 kyr BP and ending at 8 kyr BP. Most of the change may have occurred between 13 kyr BP and 9 kyr BP. On the other hand, because of scatter, the data do not eliminate the possibility of a sudden change. Isotope data from the NE Gulf of Mexico can be interpreted as evidence of either a gradual or sudden change. In the North Atlantic, the abundance of certain planktonic foraminifera changed suddenly at about 10 kyr BP. Lake levels on the continents likewise show a sudden change at about this time. Emiliani et al. (1975) give a date, when corrected for possible mixing effects, for a great flood at about 10.6 kyr BP. In short, the global record is ambiguous but there is a suggestion of important events at

about 10 kyr BP.

2.2. Documented record for the western equatorial Pacific

2.2.1. Climate and surface circulation today

Let us now focus on the deglacial changes in the western equatorial Pacific. To put the changes in context, we first review what the climate there is like today. Fig 4.3 does this. It shows the annual march of the doldrums north and south of the equator and the ocean's response to the changing winds.

From May to October winds blow from the southeast. The westward component of stress from these winds causes upwelling at the equator. This eventually results in a noticeable cooling at 100 m depth. As the winter monsoon develops over Asia, the southeasterly trades migrate south of the equator. The westward stress of these winds is replaced by the eastward stress of winds in the doldrums. Upwelling ceases. Temperature at 100 m on the equator rises. The height of the winter monsoon sees the northeasterly trades at the equator for a brief period. Some upwelling occurs. With the relaxing of the monsoon, the doldrums move north, followed finally by the southeasterly trades in May.

Horizontal motion in the upper levels of the western equatorial Pacific is governed by the south equatorial current, the north equatorial countercurrent, and the equatorial undercurrent. Both eastward currents decrease to the east, the decrease being most obvious east of 140°W (undercurrent: Philander, 1973; countercurrent: see Kendall, 1970, his Fig 1). This suggests that surface waters recirculate -- that, in

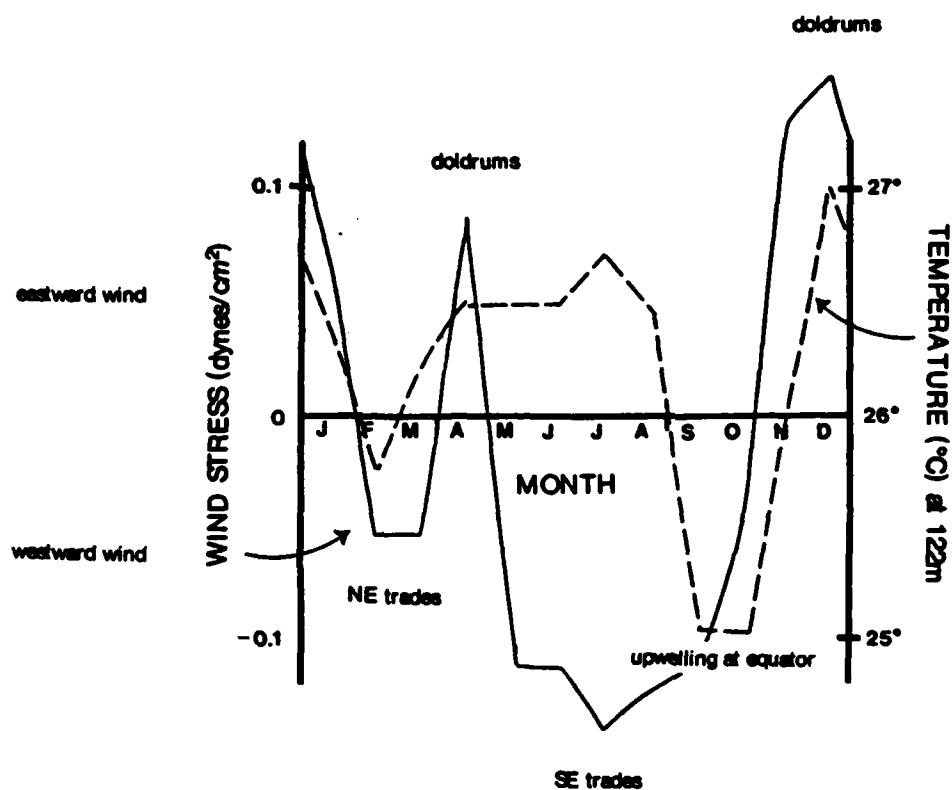


Fig 4.3. Zonal wind stress and 122 m subsurface temperatures at the equator at the longitude of Ontong-Java Plateau. The wind stress is from the averages of Wyrtki and Meyers (1975) at 155°E. Values shown are the average of their points at 2°N and 2°S; the values thus are representative of, say, 6° spanning the equator. The temperatures are from the averages of Robinson (1976) at 160°E on the equator.

fact, the equatorial current system is gyral. Reid and Arthur's (1975) map of geopotential anomaly of the surface relative to 1000 m confirms this, as do Robinson's (1976) maps of the depth to the top of the ther-

mocline. Fauna (McGowan, 1974; Bradshaw, 1959) indicate that the gyre may extend as far east as 120°W , in which case the gyre is nearly ocean wide.

2.2.2. Glacial climate and surface circulation

How did these features of climate and circulation in the equatorial Pacific change during the Ice Age? The evidence -- from land, sea-floor sediment, and numerical simulations -- is unfortunately somewhat conflicting.

2.2.2.1. Evidence from land

Evidence from land includes that summarized by Bowler et al. (1976). Fig 4.4 shows two curves extracted from their paper. The dashed curve was deduced from a pollen record from northeast Australia. It shows a dramatic increase in rainfall in this area beginning about 13,000 years ago. Age control, however, is limited to 4 widely-spaced ^{14}C dates, which, according to Kershaw (1974), may be contaminated by younger roots.

The solid curve in Fig 4.4 shows a temperature record from the New Guinea highlands. The temperatures were deduced from pollen stratigraphies in bogs at various levels on the slopes of 3 different mountains. Uncertainty in temperature estimates is claimed to be $\pm 1.5^{\circ}\text{C}$. Bowler et al. (1976) show closely spaced ^{14}C intervals but the amount of contamination is not known. In light of changes elsewhere, most relevant here is the sudden change in temperature between 10 and 11 thousand years ago. A record from a fourth site (Sirunki) is different. It

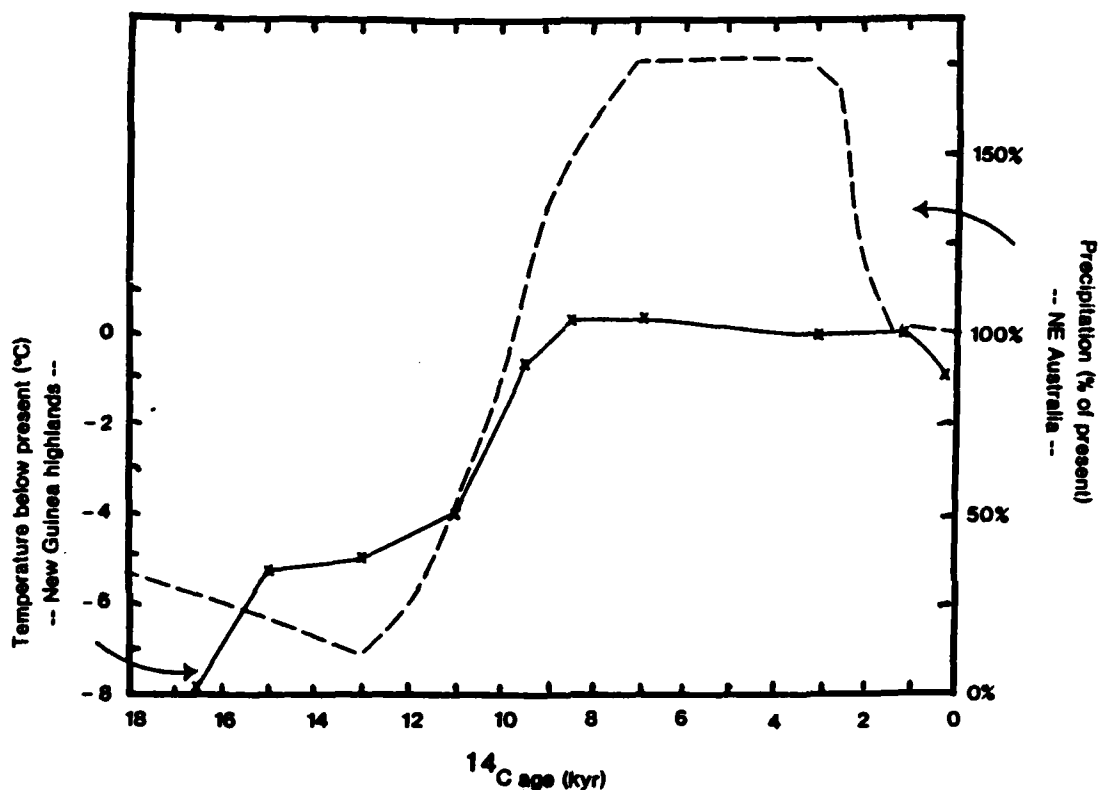


Fig 4.4. Climate change on land in the tropical western Pacific. The dashed curve shows a pollen record of precipitation in NE Australia. The solid curve shows a pollen record of temperature in the New Guinea highlands. Both curves are from Bowler et al. (1972).

shows warming between 15 and 17 kyr BP.

Löffler (1972) describes glaciation in the New Guinea highlands. Floors of cirques reached as low as 3.5 km above sea level. Löffler considers this altitude the glacial snowline (where air temperatures

were about 0°C).

Webster and Streten (1978) point out that this snowline requires surface temperatures much colder than those deduced by CLIMAP (1976). This can be seen most easily by using a temperature lapse rate of 6.5°C/km, the lapse rate of the "standard" mid-latitude atmosphere (see, e.g., Hiltner and Martin, 1957), which is drier than the equatorial atmosphere. (This lapse rate is excessive since condensation in the moister equatorial air releases more latent heat as the air rises; this causes slower cooling with height). Given this lapse rate and the height of the snowline, we see that this implies a glacial surface temperature of $3.5 \times 6.5 = 23^\circ\text{C}$ at most. Webster and Streten use a set of more likely lapse rates to deduce glacial surface temperatures of 17-20.5°C.

CLIMAP's (1976) estimate for glacial sea surface temperatures was greater than 27°C. At present, mean surface air temperatures are within 1°C of the present mean sea surface temperature of 29.5°C (US Navy, 1977; Robinson, 1976). There is a slight tendency for air temperatures to be cooler (Riehl, 1954).

A similar discrepancy between snowline-derived surface temperatures and CLIMAP (1976) temperatures appears also in the Hawaiian Islands. There the snowline fell 1 km (Porter, 1979). CLIMAP (1976) claimed a local sea-surface temperature drop of less than 2°C.

Why is there this discrepancy between CLIMAP (1976) and the land geologists in the western equatorial Pacific? There are at least three possibilities:

- 1) Snow accumulation may have been so rapid that even cirques did not represent the freezing level. Today New Guinea is one of the rainiest places on earth (see, for example, Riehl, 1954).
- 2) The cirques may have been cut during an earlier, colder glacial period. This period need not have been colder worldwide. A possibility is stage 16 shown in Shackleton and Opdyke's (1976) record of oxygen isotopes from core V28-239 from Ontong-Java Plateau. This level shows a $\delta^{18}\text{O}$ of -1.1‰ PDB in Globigerinoides sacculifer. Present isotopic composition for this species over Ontong-Java Plateau is about -2.1‰ PDB (Berger et al., 1978). If the isotopic composition of the ocean during stage 16 was 1‰ lower than today (as Savin and Stehli, 1974, suggest for the latest glacial), then the paleotemperature equation (as modified by Craig, 1965) gives a temperature of 23°C for stage 16. This is more in line with the cirque evidence.

In agreement with this is Thompson's (1976) counts of foraminifera in nearby (Fig 4.1a) core V28-238. He shows 10% abundance of Globorotalia truncatulinoides during stage 16. Compare this to the less than 1% abundance for the most recent glacial (see Table 3.2, above, species 18). Today this species lives in the northern half of the central gyre (Bradshaw, 1959). It may thus be an indicator of colder surface temperatures during stage 16.

There may be some objection to the above isotopic paleotemperature. First of all, as Shackleton and Opdyke (1976) point out, the carbonate in core V28-239 has suffered a large amount of

dissolution, which tends to make paleotemperatures cooler (Savin and Douglas, 1973). On the other hand, Shackleton and Opkyke's accompanying record of the weight percent of the fine fraction shows that stage 16 is relatively well preserved, albeit not as well preserved as ERDC 92 (which Berger et al. (1978) used to determine the present day composition of G. sacculifer). Furthermore, the change in isotopic composition of the ocean may have been greater than 1‰. The coldness of stage 16 may have been worldwide; consequently, there may have been more water tied up in ice sheets. Also, Duplessy (1978) suggests that the ice effect during the last glacial may have been 1.5‰ not 1‰.

Counter-balancing these arguments are the smoothing effects of sediment mixing. Eq (2.4) applied to the isotope record of V28-239 at the end of stage 16 may give a much "colder" glacial. However, measurement noise in the given $\delta^{18}\text{O}$ record prohibits actual use of eq (2.4) in this case.

- 3) Another possible explanation for the discrepancy between the CLIMAP (1976) temperatures and the New Guinea snowline temperatures is meteorological. Air masses impinging on the New Guinea highlands may have been much cooler and drier than today. A stronger monsoon over Asia might have caused this. Present January streamlines at 2 km (Sadler and Harris, 1970) show that the New Guinea highlands receive a certain amount of cool, dry monsoonal air. We might imagine then the possibility that the inevitable modification of these monsoonal air masses took place downstream (east) of the highlands. In this case, the climate

over Ontong-Java Plateau would have been stormy as the cool dry air swept across the sea.

Aside from that summarized in Bowler et al. (1976), the land record of glacial climate in the western Pacific is skimpy. One intriguing set of observations is that of Hutchinson (1950) on guano deposition. He observed that a number of Pacific equatorial islands had phosphate deposits but no recent deposition. Some islands with deposits are now too rainy to allow accumulation of guano. One island (Jarvis) apparently shows cycles of deposition. Hutchinson concluded that these observations reflect migration of the ITCZ in the Pleistocene. He had no age control but he later [1952; quoted in Quinn (1971)] identified times of increased guano accumulation with glacial climates. This correlation he based on Arrhenius's (1952) theory that glacial climates corresponded to high oceanic productivity because of stronger tradewinds along the equator. [Arrhenius's theory has not been disproven but his evidence has been discredited by Berger (1973)]. Quinn (1971) elaborates on the meteorological aspects of Hutchinson's observations and Arrhenius's theory.

2.2.2.2. Evidence from sea-floor sediment

We turn now to the record of glacial climate in the western equatorial Pacific as documented by deep-sea sediment. Unfortunately, published data are few and difficult to interpret. Part of the problem is that most carbonate sediment in the Pacific has suffered some dissolution. Berger (1973), Thompson and Saito (1974), and Thompson (1976) have shown that much of the down core variability in almost any param-

ter can be explained by fluctuating carbonate dissolution. Oxygen isotopes, which we used above, are a case in point (Shackleton and Opdyke, 1976; Berger and Killingley, 1977).

The available information suggests that glacial sea surface temperatures over Ontong-Java Plateau were not much different from those of today (CLIMAP, 1976; Thompson, 1976; Geitzenauer et al., 1976; Berger et al., 1978). Thompson's (1976) data indicates that an area of relatively stable temperature stretched from Ontong-Java Plateau to at least 140°W. In his Text Fig 10 (his p. 222), he shows the abundance in glacial sediment of the main planktonic foraminiferal species along an equatorial transect. There is very little change in glacial fauna to 140°W, except perhaps in the abundance of Globigerinoides ruber, which is a dissolution-susceptible species (Parker and Berger, 1971).

This observation of a large, stable gyre is apparently in conflict with the CLIMAP (1976) temperature reconstruction. CLIMAP (1976, their Fig 2, p. 1134) shows a large area of 4-6°C cooler water beginning at 170°W and stretching east to South America. This area, based to the west of 120°W on 3 cores, is centered at about 10°S. In terms of the product of the temperature change and square km involved, the cool area is the most significant which CLIMAP (1976) found on the planet. Its position and size should also result in its having a strong influence on tropical and perhaps global climate (see Barnett, 1978, for a summary of these interactions as understood to date).

Thus, the cool area found by CLIMAP (1976) deserves careful scrutiny. Unfortunately, the data and reasoning involved in their

interpretation has not yet been published. We will see next, however, that this cool area as drawn is not consistent with numerical simulations of glacial climate.

2.2.2.3. Numerical simulations

Williams et al. (1974), Gates (1976), Manabe and Hahn (1977), and others have simulated a glacial climate with some of the various global circulation models. Gates and Manabe and Hahn used CLIMAP's (1976) sea surface temperatures, sea levels, and ice distributions as input. Williams et al. (1974) collected their own set of similar data; their sea surface temperatures were based on Emiliani's early isotope work and so are cooler in the tropics than those used by the other modellers. These temperatures are still not as cool as suggested by the New Guinea glacial snowline given in Bowler et al. (1972).

The models generally agree on mid-latitude circulation (stronger than at present) but disagree on tropical circulation. Williams et al. (1974) and Gates (1976) found a reduced Hadley circulation. From this Gates (1976) suggested that ocean circulation may have been slower during the Ice Age. This is in disagreement with the conjectures of Gardner and Hays (1976) of CLIMAP, whose sea surface temperatures he used.

Williams et al. (1974) found that the summer monsoon disappeared in their model. Gates (1976) and Manabe and Hahn (1977) found it only to be weakened.

Manabe and Hahn's (1977) simulation showed the southern limb of

Hadley cells over the ocean to be strengthened. In the western equatorial Pacific, the simulation showed strengthened July glacial easterlies. This, in contrast to the other models, would imply cooler equatorial temperatures and greater upwelling over Ontong-Java Plateau. On the other hand, in the central equatorial Pacific, Manabe and Hahn (1977) found that the glacial southeasterlies became more southerly. This suggests that equatorial upwelling was not greater in this area during the Ice Age. Furthermore, from their glacial streamlines (their Fig 22, p. 3903), it does not appear that the curl of the wind stress during the Ice Age was more cyclonic in the area of CLIMAP's (1976) large Pacific equatorial cold patch mentioned above. Therefore, Ekman pumping of the kind described in Sverdrup (1947) would not have been higher in this area during the Ice Age.

In short, the two latest simulations of glacial climate are inconsistent with CLIMAP's (1976) boundary conditions in obvious cases where there is interaction with the ocean.

2.2.3. Carbonate dissolution

We consider now the documented record of changes in carbonate dissolution during deglaciation. Unfortunately, this record is only now beginning to be looked at closely (see Berger, 1977). Part of the problem is that the record of particular interest is the deep-sea record. Hence, for the most part, the effects of dissolution occur in cores of low sedimentation rate. Unraveling sediment mixing thus plays an important role in interpreting the record. As we saw in the derivation of eqs (2.3) and (2.4), there are a number of parameters that need to be

known precisely for accurate reconstruction of dissolved and mixed sediment.

Take, for instance, interpretation of Fig 4.5. This figure consists of three curves traced from Thompson (1976). The curves are data from core V28-238, whose location appears in Fig 4.1a. The top curve in Fig 4.5 shows an oxygen isotope record; the middle curve shows counts of the percent of fragments in the fraction greater than 149μ ; the bottom curve shows the weight percent of material greater than 63μ . According to Shackleton and Opdyke (1973), the isotope curve primarily records ice volume. As plotted, the up-direction on the curve means less ice. According to Berger (1973) and Thompson and Saito (1974), increasing fragments and fine fraction record increasing dissolution.

The three curves are obviously correlated. The correlation of the top and bottom curves is discussed in Moore et al. (1977). Inter-glacials ($\delta^{18}O$ on the up-cycle) appear to correspond to high dissolution (high fragment counts, high percentage of fines). Indeed, this correspondence of dissolution and climate may be worldwide (see Volat et al., 1980, for a review).

However, in the case of V28-238, some of the correlation between the curves may be due to changes in the living assemblages of planktonic foraminifera. The assemblage during warmer times may be more easily fragmented, in agreement with Berger's (1968) ranking of dissolution resistance. [Thus, the fragmentation rate, $K=K(z)$, in Chapter 2, changes somewhat independently of the dissolution rate, $s_D=s_D(z)$]. Likewise, the curve for fine fraction may be affected by productivity

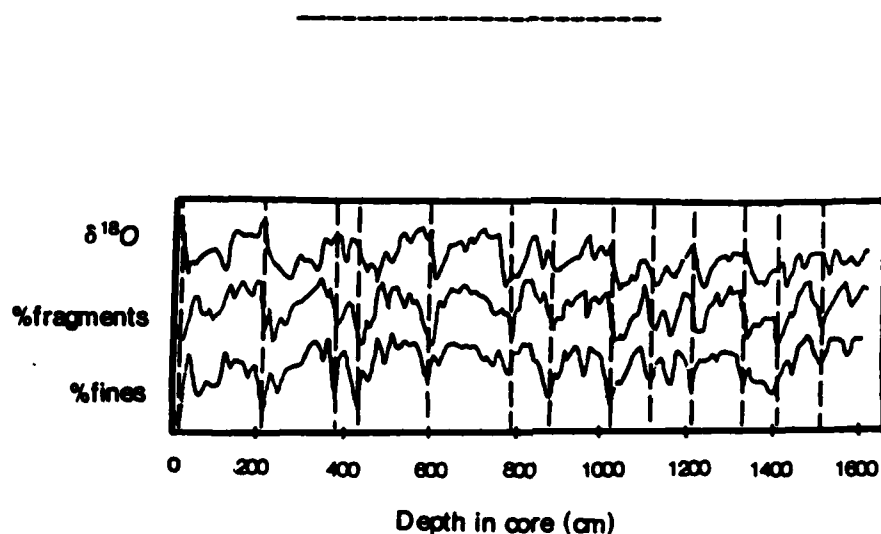


Fig 4.5. Low-resolution correlation of global climate and Ontong-Java Plateau's record of carbonate dissolution. The three curves are from core V28-238 (see Fig 4.1a) and traced from Thompson (1976). The upper curve, published by Shackleton and Opdyke (1973), represents global ice volume, up in the figure being less ice. The lower two curves depend on the carbonate dissolution rate at the depth of the core (3120 m). The dashed vertical lines mark dissolution minima.

(Broecker et al., 1958); that is, in eq (2.3), if we let n_o be fine fraction, $n_o = n_o(z)$ varies somewhat in parallel with $s_o = s_o(z)$.

In other words, just as it is difficult to make inferences about paleoclimate without accounting for dissolution, it is difficult to make inferences about dissolution without accounting for paleoclimate.

As we saw in Chapter 2, these problems of interpretation are amplified in 1-cm stratigraphy. Knowledge of the ratio of the output flux (n_s) to the input flux ($n_o s_o$) is a necessity. Observations of the

abundance of dissolution-susceptible species -- the most easily measured indicator -- cannot provide this flux ratio without extensive calibration.

Despite these problems, some workers have attempted to describe the changes in dissolution during deglaciation. The best documented change is perhaps a minimum in dissolution which occurs just before, during or after the ice-melting, the timing being not yet resolved. Berger (1977) puts the event at 14 kyr BP but he did not account for the effect of mixing on ^{14}C ages. It is clearly impossible to compare dates worldwide without doing this.

Vertical dashed lines in Fig 4.5 show the relation between the minima and ice volume at Ontong-Java Plateau. Most of the minima appear to lag deglaciation slightly. The minimum at about 800 cm is an exception. The apparent lag is in disagreement with the timing suggested for the latest minimum by Berger (1977), who put the event at the time of deglaciation.

Thus, we can sum up present understanding of deglacial changes in dissolution in one word: uncertain. Whether or not the results reported below for the ERDC cores are of global significance or only of a local character cannot be established from the literature.

2.3. Summary

In summary, the documented record of deglaciation is still in contention. Significant climate change began sometime after 15 kyr BP. The rate of change is currently unresolved. A sudden change of climate

and ocean circulation may have occurred at about 10 kyr BP.

In the western and central equatorial Pacific, Thompson's (1976) counts indicate that the planktonic foraminiferal assemblage showed little change. This may imply that the equatorial gyre in glacial times was about the same size as today. CLIMAP's (1976) estimates of glacial sea-surface temperature disagree with this but numerical simulations do not support the estimates.

The deglacial record of carbonate dissolution is uncertain as of yet.

3. Sedimentology of ERDC cores

With this information from the literature in mind, we now examine data from the ERDC cores. Our objective, as stated at the outset, is to reconstruct a 1-cm stratigraphy consistent with published history. We have just seen that the published history relevant to us (the glacial-Holocene transition) is ambiguous and conflicting. Thus, in a sense, we have no firm "ground truth." Nevertheless, there are still enough constraints from the literature to make a close examination of the ERDC data enlightening in one way or another. Whether this enlightenment is a verification of the theory in Chapter 2 is unclear.

Before examining detailed stratigraphies from Ontong-Java Plateau, we first consider the sedimentology of the area. Of particular importance are mixed layer thicknesses, mixing rates, and sedimentation rates.

3.1. Mixed layer thicknesses

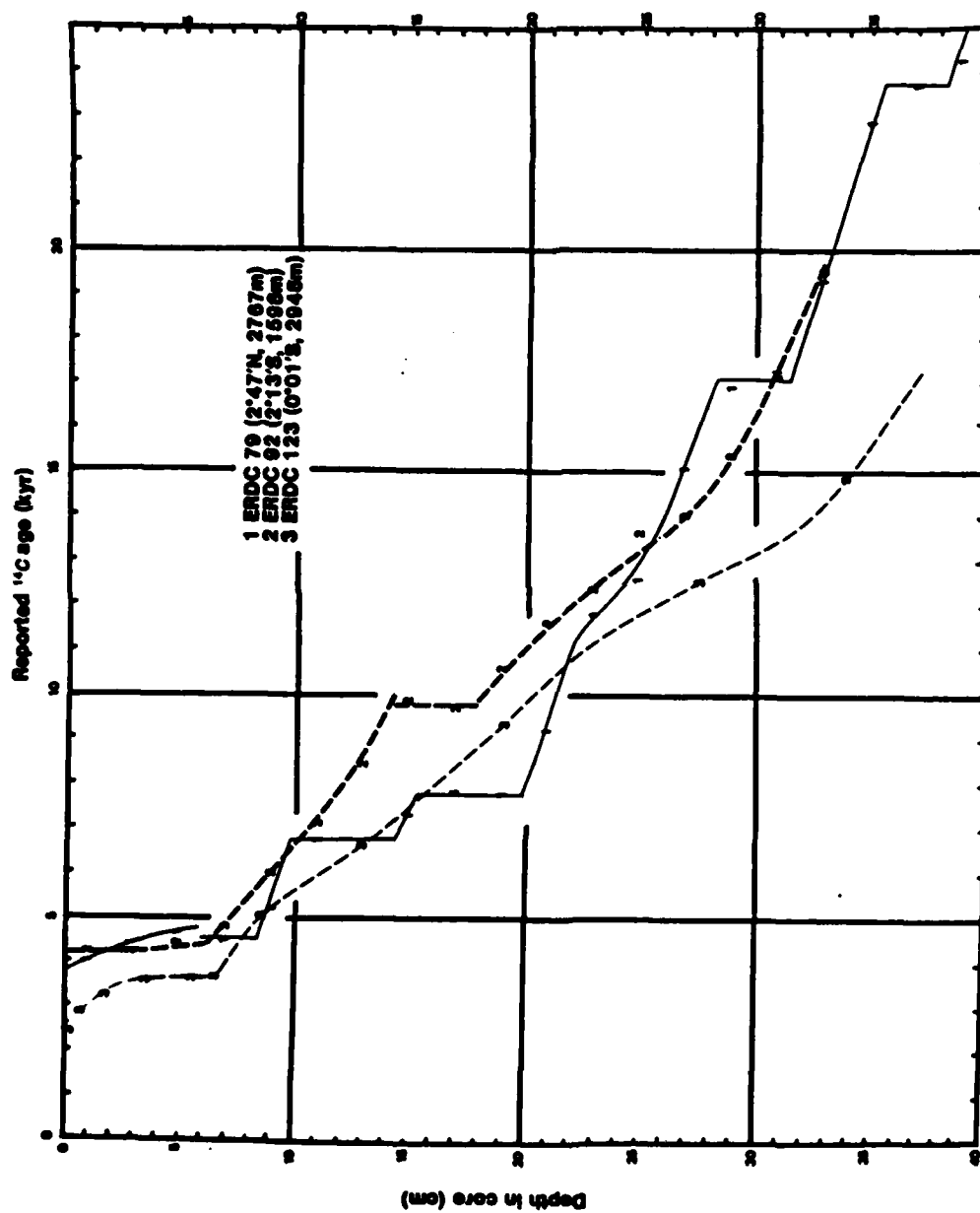
Fig 4.6 shows ^{14}C data from 3 closely sampled cores. The data from ERDC 92 appear in Peng et al. (1979); the data from ERDC 123 appear in Krishnamurthy et al. (in press); the data from ERDC 79 are from Berger et al. (in preparation). In ERDC 79 and 123, one-sigma uncertainties in dates due to counting statistics are of the order of 200 yr or less. In ERDC 92, 1σ varies from 180 yr in the mixed layer to 850 yr for the deepest sample (see Peng et al., 1979, for actual values).

Samples from ERDC 92 and 79 are 2 cm thick — contiguous samples touch. Each sample thus represents an average over 2 cm. To connect the data points, it is incorrect simply to draw straight lines between; a 2-cm average over these lines will not result in the correct datum, except in special cases such as constant accumulation rate. Consequently, connecting the points requires a certain amount of interpretation. The constraint is that the average of the interpretation over the 2-cm intervals be the data points.

My interpretations are shown. A slightly different interpretation of ERDC 79 appears in another figure below (Fig 4.18a). We will discuss each of the interpretations in Fig 4.6 shortly. It is sufficient to note at this point that a 2-cm sampling interval is too coarse to resolve a number of the features in these ^{14}C records.

In spite of the limited resolution, Fig 4.6 does show that a discrete mixed layer exists exist in some cores. The bottoms of these mixed layers are relatively sharp.

Fig 4.6. Closely-spaced ^{14}C dates for 3 ERDC cores. The data for ERDC 79 are from Berger et al. (in preparation); those for ERDC 92 are from Peng et al. (1979); those for ERDC 123 are from Krishnamurthy et al. (in press). Data points are indicated by the numbers, 1, 2, and 3. The curves are my interpretations of the data.



Three other ERDC cores have been closely dated near the core top: 102, 129, and 141 (Krishnamurthy et al., in press). ERDC 102 shows dates which zig-zag over 3 kyr within the upper 8 cm. ERDC 141 shows a 6 kyr age in the top cm and a steady decrease below. The core appears as if it were unmixed. ERDC 129 looks similar but there is one 1.5 kyr zig-zag and a 1 cm isochronal layer in the upper 5 cm. Both cores are from over 4000 m depth (Fig 4.1) and so are heavily dissolved. Whether these two cores appear unmixed as an artifact of dissolution or as an actual lack of animal activity is worth further study.

Fig 4.6 seems to indicate the following mixed layer thicknesses: ERDC 92, 5-7 cm; ERDC 79, 8 cm; ERDC 123, 7 cm. Peng et al. (1979) gave a thickness of 8 cm for ERDC 92. They assumed 1-cm was lost from the top of the core. This is, of course, possible, but there is no evidence to confirm or deny this. Krishnamurthy et al. (in press) give a thickness of 9 cm for ERDC 123. This value was based in part on the ionium-thorium distribution in the top of the core. It is difficult to reconcile this 9-cm estimate with the ^{14}C profile shown in Fig 4.6.

A detailed stratigraphy (see Fig 4.18a below) shows a sharp change in the abundance of P. obliquiloquata at 4 cm in ERDC 79. The layer 5-8 cm in this core may thus be an isochronal layer (of the types discussed below) out of reach of mixing. The slight inversion of ^{14}C ages from 5-7 cm supports the idea that this layer is foreign.

A mixed layer thickness of 4-6 cm is also likely for ERDC 128. Fig 4.7 shows measurements of coarse fraction from this core. Late Holocene dissolution (discussed below) has apparently resulted in a

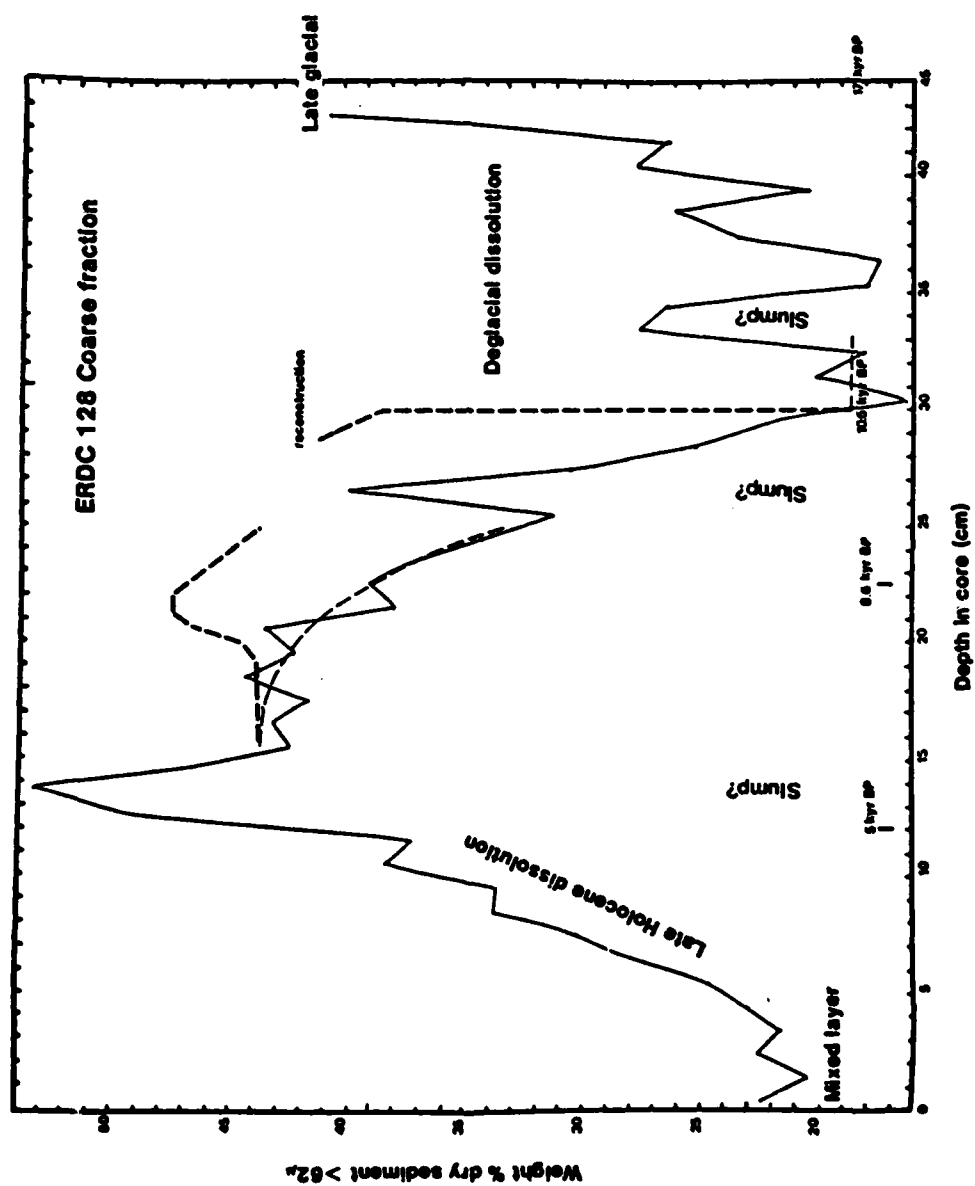
recent rapid change in the coarse fraction. This change makes the homogenization of the upper 4-6 cm clearly visible.

Similar homogenization can be seen in some of the CaCO_3 measurements from the ERDC cores. Fig 4.8a shows the variation of percent carbonate in the shallow cores; Fig 4.8b shows the variation in the deeper cores. Notice in Fig 4.8a that even the shallow cores display a sudden decrease of carbonate just below the mixed layer. This decrease -- presumably due to dissolution -- is most evident in cores at or deeper than the depth of ERDC 79. The fluctuations in the surface samples (0-1 cm) may be due to water sloshing in the box corer during core recovery (see discussion of mixing rates, below, where the effect may also appear). ERDC 129 does not show a mixed layer in its carbonate curve. As mentioned above, its ^{14}C profile did not show one either.

These carbonate data (Fig 4.8) favor a mixed layer thickness of 6 cm or less. However, the sampling interval is somewhat large and the noise in measurement is considerable. The rms error is about 1.5% CaCO_3 .

In summary, observed mixed layers, where present, seem to be between 4 and 9 cm on Ontong-Java Plateau. If a value of 4 cm is correct for ERDC 79, a range of only 4 to 7 cm is possible. Berger and Johnson (1978) calculated a range of 7.5 to 9.5 cm from mixed layer ages. However, these calculations assumed that dissolution, winnowing, and horizontal influx were negligible for the cores then considered (ERDC 120, 123, 125, and 135). We will see shortly that this was a poor assumption.

Fig 4.7. Coarse fraction in ERDC 128. Section 4.2.1 discusses the stratigraphy shown in this figure. The measurements (made by D. Ripley) relied on ultrasonication to disaggregate the sediment.



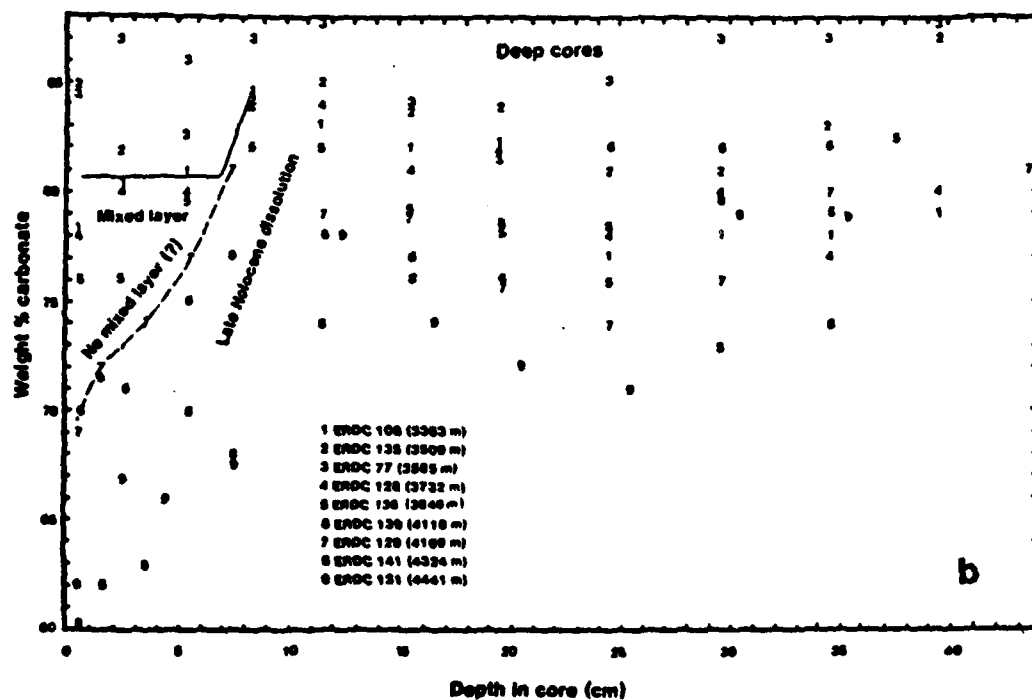
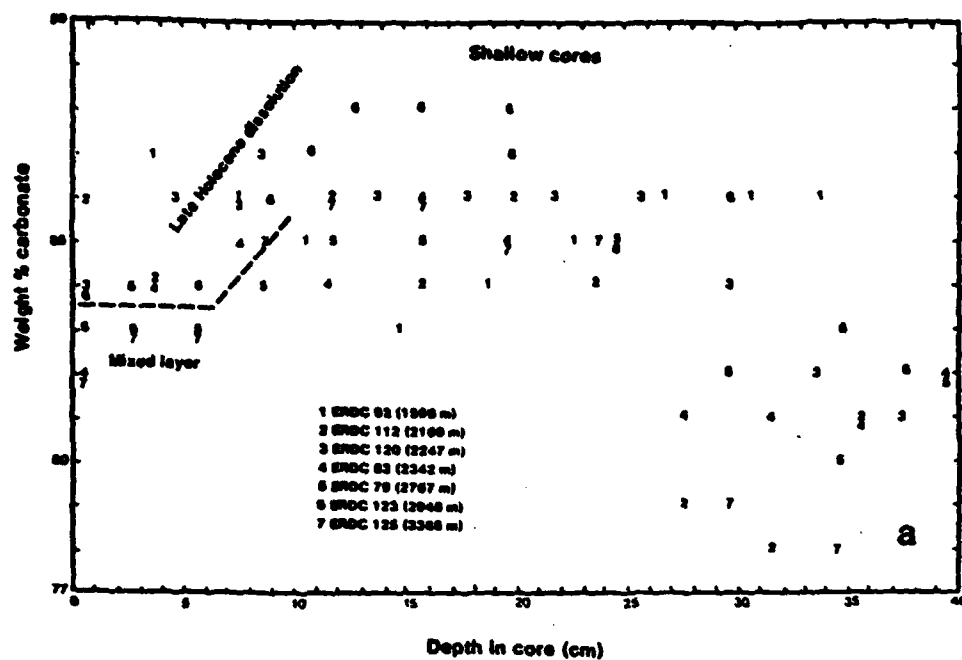


Fig 4.8a,b. Weight percent carbonate in the ERDC cores. Precision and method of measurement are described below.

If the observed range is real, then we must consider the possibility of at least a similar range down core. Such a range may limit the ultimate accuracy of signal reconstruction via eqs (2.3) and (2.4). We may eventually sidestep this problem if and when we know the causes of variability in thickness. For instance, the thickness might be tied to the concentration of organic carbon in the mixed layer. This concentration, in turn, must depend on the flux of new and old sediment to and from the mixed layer. This flux we can estimate one way or another and so work our way back to the instantaneous value of Z .

3.2. Mixing rates

The ^{14}C records in Fig 4.6 may also indicate the mixing rate, D . The rate for ERDC 92 appears high, as discussed in Peng et al. (1979). The rate in ERDC 79 appears to be lower. Fig 4.9 models the mixed layer in ERDC 79 for various mixing rates. The mechanics of the model are precisely those of Goldberg and Koide (1962): we assume steady state, no leaks, no conversion, no horizontal influx, no deep-burrowing, and constant D . The upper set of curves in Fig 4.9 assume that the mixed layer thickness is 8 cm; the lower set assume that the thickness is 4 cm. Curves on the left assume that the sedimentation rate (s_0) is 2 cm/kyr; those on the right assume that the rate is 1 cm/kyr. In the figures, depth is shown as a fraction of the mixed layer thickness.

Clues to the mixing rate lie in the shape of the mixed layer ^{14}C curves, not in the ages themselves. Thus, ERDC 79 is about 800 yr younger at the surface than at 5 cm. If $Z=8$ cm, this can be achieved, according to the upper set of curves in Fig 4.9, by $D=20-30 \text{ cm}^2/\text{kyr}$. If

$Z=4$ cm, this can be achieved, according to the lower set of curves, by $D=5-10$ cm²/kyr.

ERDC 123 in Fig 4.6 exhibits an even more pronounced younging at the surface. However, the shape of this curve does not fit the Goldberg-Koide model (Fig. 4.9). What this core may show is the effect of water sloshing in the box corer during core retrieval. The sloshing may cause winnowing and redeposition. The effect would be to concentrate one size fraction or another. As we saw in Chapter 2, size fractions tend to have widely different ages. ERDC 79 may have suffered from the same problem. In ERDC 123, the upper cm appears to be the most affected. Other cores show unusual values of carbonate percentage (Fig 4.8) and grain size (Fig 4.15, below) in the upper cm. Photographs of the box cores show some redeposition; however, the photos also show that many surface features such as fecal mounds are preserved during core recovery.

3.3. Sedimentation rates

We consider now ERDC data on sedimentation rates. We are concerned in this section with processes not stratigraphy. We thus postpone until later all discussion of the climatic significance of down-core changes in sedimentation rate.

Ultimately we need to know the magnitude of each of the components in the net accumulation rate:

$$s = s_o + s_h - s_D - s_w . \quad (4.1)$$

As in Chapter 2, s is the accumulation rate, s_o is the rate of supply of

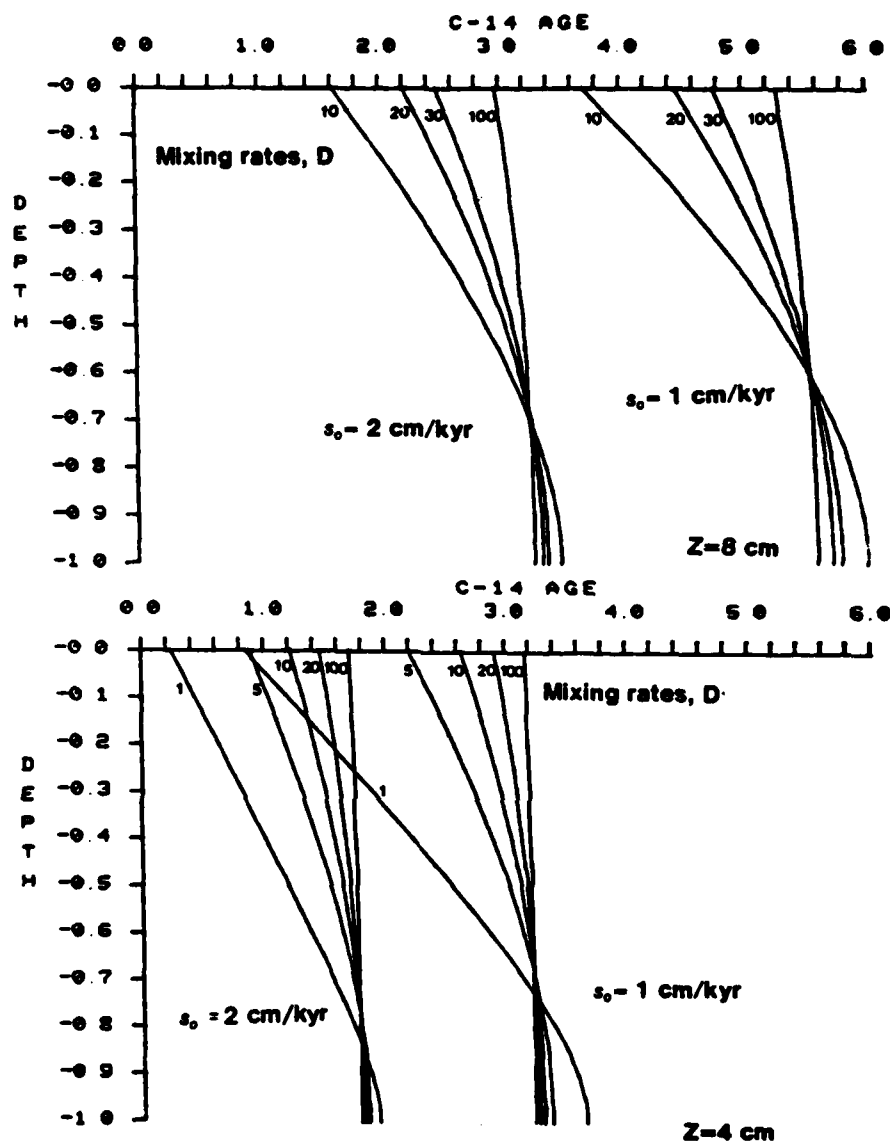


Fig 4.9. Goldberg-Koide (1962) model of the mixed layer of ERDC 79. The upper figure assumes that the mixed layer thickness, Z , is 8 cm; the lower figure assumes that $Z=4$ cm. The set of curves on the left in each figure assume that the sedimentation rate (s_0) is 2 cm/kyr. The set on the right assumes that the rate is 1 cm/kyr. Values for the mixing rate, D (cm^2/kyr), are shown to the left of each curve. Compare these curves with the ^{14}C profile for ERDC 79 shown in Fig 4.6.

fresh sediment, s_h is the rate of horizontal influx, s_d is the dissolution rate, and s_w is the winnowing rate. Units are, say, cm/kyr. In what follows, we will see that, with the data at hand, it is difficult to enumerate each component.

Given sufficient ^{14}C data, we can find the accumulation rate, s , more or less directly: For steady state, s is the slope, $\frac{dz}{dt_r}$, in profiles of depth (z) vs. reported age (t_r). Thus, Fig 4.6 shows that ERDC 123 accumulated at a rate generally greater than 2 cm/kyr, that ERDC 92 accumulated at a rate generally less than 2 cm/kyr, and that ERDC 79 accumulated at a rate generally less than 1 cm/kyr. Both ERDC 79 and 92 display isochronal layers, of which we will have more to say shortly. About half the sediment in ERDC 79 accumulated through the mechanism of these layers.

The accumulation rates of the cores in Fig 4.6 were not constant. Intervals of relatively low accumulation appear at the bottom of the mixed layer in ERDC 123 and at the bottom of the core in ERDC 92. Intervals of relatively high accumulation appear at about 25 cm in both ERDC 79 and 92. However, the interval in ERDC 79 can also be interpreted as an isochronal layer (see Fig. 4.18a, below).

Clearly, steady state is not the rule in these cores. The apparent accumulation rate, s_r , is therefore not necessarily equal to the actual accumulation rate: The age of the mixed layer may be in a state of change. See Chapter 2, Section 3.2.2. My interpretations in Fig 4.6 show a gradual change in s_r when I believe changes in this rate include changes in the mixed layer age.

Some of the interpretations in Fig 4.6 are arbitrary. 2-cm sample intervals do not suffice to resolve many of the features of the ^{14}C profiles. For instance, undetectable is the 20% increase in apparent accumulation rate due to changes in the ^{14}C concentration in the atmos-

phere between 5500 BP and 2000 BP (see Chapter 2, Section 3.1). The higher apparent rate should appear between reported ages of 9500 BP and 6000 BP, according to eq (2.7). Likewise, it is probable that the ^{14}C profile in ERDC 123 is smooth below 10 cm only because the sample interval is large.

A broader view of sedimentation rates on Ontong-Java Plateau follows from the data in Table 4.1. This table gives ^{14}C dates from 3 levels in each of 14 of the ERDC cores. The 3 levels consist of one in the mixed layer, one just below the mixed layer (depth= z_1), and one deeper down (depth= z_2). The table shows the ages at these 3 levels [$t_{\text{ML}}, t_r(z_1), t_r(z_2)$]. Also given in the table are estimates of mixed layer thickness, Z , based on Figs 4.6-4.8. If these figures are not definitive, I have assumed $Z=7$ cm.

Not included in the table are dates from ERDC 88 and 102. These cores are severely disturbed. Included, however, are ERDC 129 and ERDC 144, even though they do not display a mixed layer in their ^{14}C profiles (see above). For these cores, Table 4.1 does not include any data or calculations involving the mixed layer.

Sources for the ^{14}C data in Table 4.1 are Berger and Johnson, 1978, Peng et al., 1979, Krishnamurthy et al., in press, and Berger et al., in preparation.

The two deeper ^{14}C dates provide accumulation rates in the usual way. These rates are listed in the rightmost column in Table 4.1. The column is labelled as reported accumulation rate, s_r , for two reasons. First, unless a steady state exists, the true accumulation rate, s ,

Core	Depth (m)	Latitude	%CaCO ₃		Z ₁ (m)	t _{ML} (yr)	Z ₂ (m)	t _r (z ₂) (yr)	Z ₃ (m)	t _r (z ₃) (yr)	s ₀ * (mm/yr)	s ₀ (mm/yr)	s ₀ (mm/yr)
			mixed layer	Holocene									
77	3583	4.05	86.90	85.00	4.0	6495	0.5	7210	22.5	19175	0.40	0.45	1.17
79	2767	2.79	81.50	84.75	4.0	4400	9.0	5210	23.0	11820	0.66	0.77	2.12
83	2362	1.40	81.50	84.75	7.0	3695	8.5	4380	22.5	8925	1.41	1.59	3.08
92	1598	-2.23	87.00	85.00	6.5	4400	9.0	6000	24.0	13000	1.12	1.31	2.14
108	3383	-1.75	88.00	82.50	7.0	4680	8.5	5870	22.5	11650	1.03	1.19	2.42
112	2169	-1.63	85.00	85.50	7.0	4340	8.5	5040	22.5	9895	1.20	1.41	2.88
120	2247	-0.02	86.00	86.25	7.0	3940	12.0	5290	36.0	16030	1.38	1.63	2.23
123	2348	-0.02	83.50	85.75	7.0	3390	11.0	5620	35.0	14650	1.61	1.95	2.66
125	3368	-0.00	83.00	83.50	7.0	3410	12.0	5600	34.0	14963	1.59	1.93	2.35
128	3732	-0.01	80.00	81.50	5.5	4015	8.5	5570	22.5	12070	0.98	1.16	2.15
129	4169	-0.01		78.00			8.0	10040	17.5	18320			1.51
131	4441	-0.03	66.50	72.00	8.0	6270	12.0	11220	19.0	15970	0.65	0.73	1.47
135	3509	0.88	82.50	83.00	7.0	4540	12.0	6770	32.0	22300	1.10	1.28	1.29
136	3448	1.10	76.00	79.00	4.0	4250	8.5	5915	22.5	13740	0.63	0.74	1.79
139	4118	1.36	71.50	76.00	4.0	5590	12.0	11010	20.0	19700	0.41	0.47	0.92
141	4324	2.36		71.00			3.5	8810	7.0	12880			0.86

Table 4.1. Data used to determine sedimentation rates for the ERDC cores. The table includes 3 ¹⁴C dates for each core: one in the mixed layer (t_{ML}), one just below the mixed layer at depth z₁ [t_r(z₁)], and one deeper down at depth z₂ [t_r(z₂)]. The table also shows mixed layer thicknesses observed or assumed for each core. The two columns labelled CaCO₃ give the mixed layer and Holocene carbonate percentages, the later being a graphical average between the surface and z₂ from Fig 4.8. The rightmost column provides accumulation rates.

$$s_r = \frac{z_2 - z_1}{t_r(z_2) - t_r(z_1)}.$$

The other two columns at the right, s₀* and s₀, give rates of supply of fresh sediment calculated from mixed layer ages and eq (2.8c). The column marked s₀ assumes that deep burrowing has increased the mixed layer ages by 500 yr; the column marked s₀* does not.

differs from the reported rate, s_r , as discussed in Chapter 2. Second, the reported rates are an average over a certain period of time; the period is not quite the same amongst the cores.

The most important sedimentation rate for our purposes is the rate of supply of fresh sediment, s_o . Not only is this usually the biggest contributor to the net accumulation [eq (4.1)] but it is also of great stratigraphic importance, since in the deep sea s_o depends upon the productivity of overlying waters.

There are two somewhat independent ways to recover s_o from the data in Table 4.1. One way is to re-arrange eq (4.1) thusly:

$$s_o = s - s_h + s_D + s_w. \quad (4.2)$$

We use s_r in Table 4.1 in place of s , estimate s_h , s_D , and s_w , and then calculate s_o from eq (4.2).

The second way to find s_o is via mixed layer ages and eq (2.8c). Recall that eq (2.8c) accounts for dissolution, winnowing, and horizontal influx by the ratio, $\frac{n}{n_o}$, so long as the sediment lost or gained by these processes is the same age as the sediment of the mixed layer en masse. Values for s_o found from mixed layer ages are present values, in distinction to values found from eq (4.2) and the two deeper ^{14}C dates. The latter values are, say, Holocene averages.

What we will do now is calculate s_o for each core by the two different methods. In the first method [eq (4.2)], the major uncertainty is the amount of horizontal influx, s_h . In the second method [eq

(2.8c)], both the amount and age of horizontal influx are uncertain.

3.3.1. s_o from mixed layer ages

Let us proceed with the second method first, since it is unconventional. Calculations of s_o from mixed layer ages and eq (2.8c) appear in the second and third columns from the right in Table 4.1. The calculations in the table assume that the carbonate fraction, n_o , in fresh sediment is 86%; results are not sensitive to this. The table gives the fraction, n , observed in the mixed layer. The column third from right labelled s_o^* is the straight calculation. The column second from right labelled s_o uses a mixed layer age 500 yr younger than that given in the table. This 500 yr is intended to compensate for the presence of deep burrowing. Fig 4.6 argues against a larger correction. No obvious burrowed layer of the kind modelled in Chapter 2, Section 5, appears. This suggests that $b/s_o < 30\%$ (Fig 2.6). (As in Chapter 2, b is the burrowing rate; b/s_o is the fraction of the area of the historical layer which is covered by burrows in a vertical slice). Fig 2.7 shows that for $b/s_o = 30\%$, 500 yr is reasonable for the effect of deep burrowing on the mixed layer age. Although the model in Chapter 2, Section 5, neglects dissolution, winnowing, and horizontal influx, the order of magnitude of the burrowing-correction will probably not be changed by these complications. The column third from the right (labelled s_o^*) does not include the 500 yr correction.

Fig 4.10 shows a plot of s_o (with the 500 yr burrowing-correction) vs. latitude. The idea here is that s_o should be highest on the equator due to upwelling (see Fig 4.3 and its discussion). The

position of each core in Fig 4.10 is marked by a number which is its reported accumulation rate, s_r . Cores which are from sites deeper than 3000 m have their accumulation rates, s_r , underlined in the figure. Sites between 3000 m and 3600 m have a broken underline; sites deeper than 3600 m have a solid underline.

Superimposed on Fig 4.10 is a curve of primary productivity averaged from the data of Rotschi et al. (1972). In the figure, I have arranged the scale of the primary productivity such that equatorial values coincide with the maximum calculated values of s_o for cores on the equator. The zero in the productivity curve lines up with the zero on the s_o axis.

The data of Rotschi et al. (1972) result from only a few cruises. For this reason, the curve of primary productivity in Fig 4.10 may not be strictly comparable to the thousand-year averages of s_o recorded in the sediment. In fact, the data are from 1965-1966, which was at the end of the 1965 el Niño. December 1965 temperatures at 400 ft (122 m) were 20°C at the equator (Rotschi et al., 1972, their Fig 3, p 43). This was 6 or 7°C cooler than normal [see Robinson's (1976) December map; or Fig 4.3 above]. However, Fig 10 (their p 111) of Rotschi et al. (1972) shows no spectacular increase of primary productivity at the equator during December 1965. This may indicate that the sea surface mixed layer in the western equatorial Pacific does not receive added nutrients during el Niño. This conforms with Wyrtki's (1975) idea of equatorial sloshing: In other words, the mixed layer merely thinned in December 1965; there was no pumping through the thermocline. As a matter of fact, Rotschi et al. (1972) show a peak of productivity in

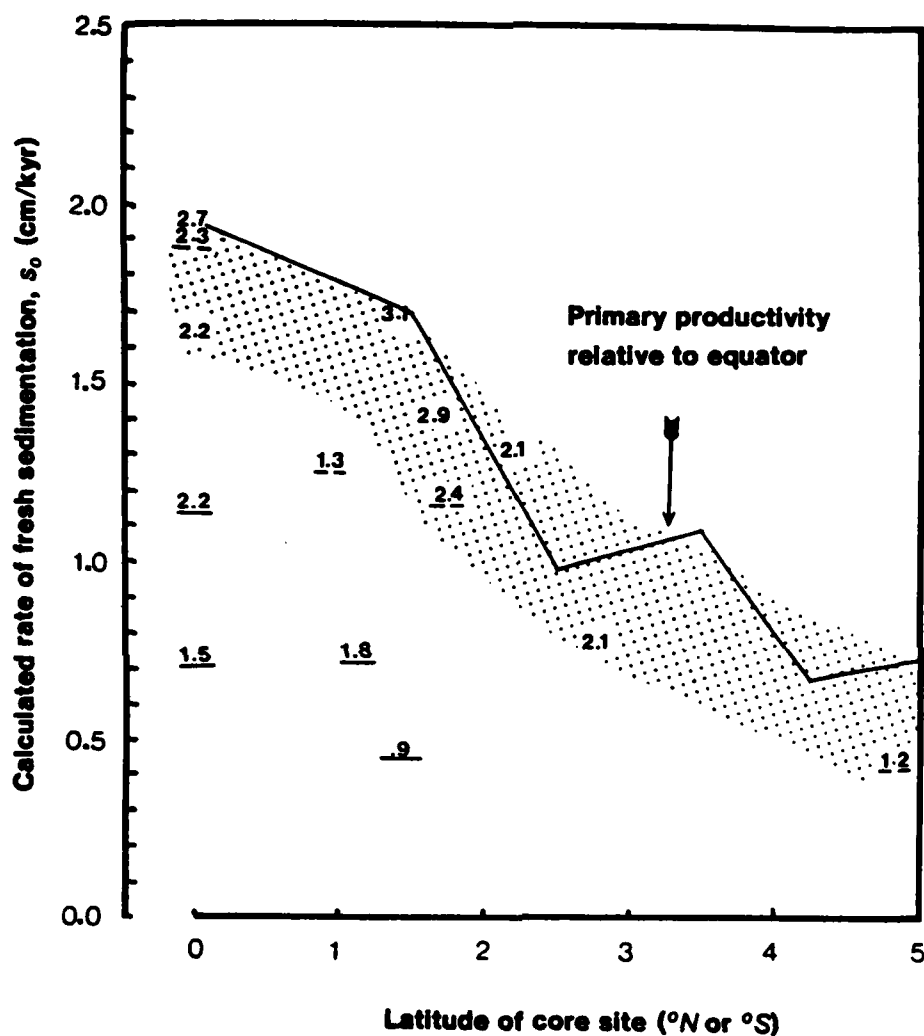


Fig 4.10. s_o vs latitude, from mixed layer ages and eq (2.8c). Mixed layer ages are those in Table 4.1 minus a 500-yr correction for deep burrowing. Position of each core in the plot is marked with s_r from Table 4.1. Cores deeper than 3000 m are underlined; if less than 3600 m, the underline is broken; if greater than 3600 m, the underline is solid. Solid curve is primary productivity from Rotschi et al. (1972).

their cruise of September–October 1966, in agreement with the annual cycle shown in Fig 4.3. So, even though their cruise occurred during an unusual year, the productivity variations they found appear representative in time and, hopefully, space.

Several features are worth noting in Fig 4.10. First of all, nine of the 14 cores in Fig 4.10 fall more or less along the curve of primary productivity (dotted area). Every core deeper than 3600 m is considerably below the curve. For the shallower cores, there appears to be a sharp break in the latitudinal variation of s_o between 1.5° and 2.5° just as there is in the primary productivity curve. However, the scatter is large. The plot shows convincingly, though, that ERDC 77 and 79 (the rightmost two points) have distinctly lower rates of supply of fresh sediment. The s_o calculated for ERDC 79 is .77 cm/kyr (Table 4.1). This is not very different from the rates for this core shown in Fig 4.6 between intervals of isochronal layers. (The s_r for ERDC 79 in Table 4.1 includes the effect of the isochronal layers).

How can we explain the scatter in Fig 4.10? The simplest way is to think in terms of mixed layer ages. Cores whose calculated s_o are higher than the actual values have mixed layers which are too young. Conversely, cores whose calculated s_o are lower than the actual values have mixed layers which are too old.

Possible reasons for "old" mixed layers are:

- 1) underestimation of the mixed layer thickness, Z ,
- 2) non-steady state such that $s > s_r$ (see Chapter 2, section 3.2.3),

- 3) erosion,
- 4) deep-burrowing,
- 5) dissolution or winnowing of young material preferentially, or horizontal influx of old material; in other words, in eq (2.8b), $c_D > c$ or $c_W > c$ or $c_H < c$ (see Chapter 2, Section 3.2.2),

Mixed layers can be "too young" because of

- 1) overestimation of Z ,
- 2) non-steady state such that $s < s_r$,
- 3) ponding of fresh sediment,
- 4) finite mixing rates,
- 5) and dissolution or winnowing of older material or influx of younger material; in other words, in eq (2.8b), $c_D < c$ or $c_W < c$ or $c_H > c$.

All of these factors may be at work but some are more likely than others. Let us consider them one by one.

Gross under- or over-estimation of the mixed layer thickness does not seem likely. According to eq (2.8c), to achieve a doubling of s_0 , we must double Z for a fixed mixed layer age. In the case of the deeper cores, even doubling Z would not bring the plotted s_0 's up to the primary productivity curve. For ERDC 79 (the second point from the right in Fig 4.10), doubling the 4 cm thickness used would bring Z up to that suggested by the ^{14}C profile (Fig 4.6) but would leave unexplained the faunal variation (see Fig 4.18a) within this 8 cm "mixed" layer. As mentioned, the low value of s_0 for ERDC 79 shown in Fig 4.10 is con-

sistent with the low value of the slope, $\frac{dz}{dt_r}$, indicated in Fig 4.6. (The same can be said for the slope in the profile of ERDC 92).

A non-steady state may in fact exist in view of the recent increase of carbonate dissolution at Ontong-Java Plateau (see below). Whether or not this affects mixed layer ages depends on whether or not dissolution preferentially dissolves material that is younger or older. We will have more to say about this shortly.

Erosion is a possibility that cannot be eliminated without finer ^{14}C sampling. Ponding is unlikely here but may explain why the core shown in Nozaki et al. (1977) has such a young mixed layer.

Deep-burrowing is likely. The 500-yr correction used in Fig 4.10 may be too much in some cases and too little in others. Inspection of the cores themselves does not indicate much difference between cores nor that b/s_0 is much greater than 30%. Appearance can be deceiving though, since visual detection of burrows depends on color contrasts, which may not exist in some filled burrows.

As we discussed above, some cores do exhibit finite mixing rates. These rates will tend to make mixed layers younger than predicted by eq (2.8c). For the likely range of rates, this "younging" should amount to something less than 500 yr (Fig 4.9). This could lower the s_0 's in Fig 4.10 by up to 20% but 10% is a more likely figure.

There is one remaining possible explanation for the scatter in Fig 4.10: The sediment in horizontal influx, winnowing, and dissolution may not be the same age as the mixed layer. The old mixed layer ages

for the 5 cores deeper than 3600 m suggest that dissolution may remove mostly young material. In an extreme case, much dissolution of carbonate may occur immediately following deposition, before burial in the mixed layer. In such a case, the actual input of fresh sediment (s_0) is simply the flux from the surface minus the amount of dissolution.

One example of such an extreme may be the sedimentation of pteropod shells. These aragonitic shells are probably an important component of the carbonate flux from the sea surface over Ontong-Java Plateau (as they are elsewhere; see Berger, 1978b). Yet little or no aragonite occurs in samples from the mixed layers of ERDC cores. [I found 1 pteropod shell in the fraction $>840\mu$ after sieving 700 cm^3 of mixed layer sediment from ERDC 79 and ERDC 83. The amount of aragonite in the finer fractions is unknown; Keir (1980) found aragonite in the $<62\mu$ fraction of a sample from ERDC 92 but the stratigraphic position of the sample is unknown].

One possible explanation, then, for the low s_0 of the deeper cores in Fig 4.10 is that there is a component in the sediment which is an analog of aragonite: it dissolves before burial. As mentioned, if we assume that the departure of the deeper cores from the productivity curve is due primarily to pre-burial dissolution, the amount of this dissolution is the departure itself. This exceeds 70% of s_0 in one case in the figure (ERDC 139, indicated by $s_0=.9$).

The large percentage for this and the other deep cores argues against the departure being due primarily to the existence of an aragonitic analog. There is no single fraction in the sediment this large.

Fine fraction, which dissolves at a relatively high rate in Keir's (1980) experiments, probably constitutes no more than 50% of the original undissolved (calcite) sediment.

Thus, if dissolution of young sediment is indeed responsible for the departures in Fig 4.10, sediment of a non-zero age must be dissolving, at least in the deeper cores. This in turn would imply that the amount of dissolution is larger than the departures. The exact amount would depend on the age [or c_D in eq (2.8b)] of the dissolved material.

A similar argument applies if we attribute the departures to winnowing. In this case, it is even more difficult to find an aragonite analog: Preburial winnowing is probably not important. As mentioned in Chapter 2, most fine sediment arrives in fecal pellets (Honjo, 1975); nondeposition of fines due to energetic water motions is thus unlikely. Once fine particles are buried, there is no reason for winnowing to discriminate amongst them by age, unless there is a time-dependent aggregation process of which we know nothing. Thus, winnowed material as a whole must be of a non-zero age; in fact, it is likely to be about the age of the fine fraction. Since the fine fraction is large in the deep cores (>80%), the age of any material winnowed from their sites is probably about the age of the mixed layer. Therefore, the departures in Fig 4.10 cannot be due to winnowing.

A last possibility is that horizontal influx contributes material of an age distinct from the mixed layer. Berger et al. (1977b) showed that the topography on Ontong-Java Plateau is quite rugged in places (see Fig 4.1b; also see Berger and T.C. Johnson, 1976). The

deeper cores, with the exception of ERDC 77, are situated within the fine-fraction settling distance (see Table 2.1) of a major submarine valley. (ERDC 108 is in the valley proper; see Fig 4.1). Slumping and sliding probably go on in this valley (Berger et al., 1977b). Any fine fraction suspended by these processes may travel to the sites to the north, assuming that currents are in that direction.

Small valleys also incise the upper part of the plateau. ERDC 79 was recovered from one and indeed seems to record slumping or some other form of sudden influx. Another source of material in horizontal influx may be erosion from the top of the plateau. There may be examples of such erosion in the ERDC cores: ERDC 83 may have lost material between 7 and 10 kyr BP (see below); ERDC 102 displays a ^{14}C age of 8 kyr BP in its upper cm (see data in Krishnamurthy et al., in press).

In short, lateral transport is apparently an important process on Ontong-Java Plateau. One way to quantify this is via the shallow cores. If we assume that $s_D = s_w = 0$ in these cores, then eq (4.1) gives us a maximum (of sorts) for s_h : It is $s - s_0$, s being read from each point in Fig 4.10 and s_0 being read from the corresponding ordinate value. A minimum (of sorts) for s_h can be found by letting all the carbonate coming in laterally be "dead" carbonate: We set $c_h = 0$ in eq (2.8b) and get that

$$s_h = \frac{s(e^{\frac{dt_{ML}}{n_0}} - 1) - \frac{dz}{n_0}}{\frac{n_h}{n_0} + e^{\frac{dt_{ML}}{n_0}} - 1} \quad (4.3)$$

If the horizontal influx is from suspension, a reasonable value for n_h ,

the carbonate fraction of the influx, is 60% or less. If the horizontal influx is from some sort of bedload, then a reasonable value is 75% or more. Table 4.2 uses these values and eq (4.2) to calculate minimal s_h for the shallow cores. It also shows the maximal s_h from $s-s_0$. Data for both calculations are in Table 4.1, except for the accumulation rate, s , of ERDC 92, which Fig 4.6 indicates to be 1.6 cm/kyr. Where available we must use present values of s because we are using present values of mixed layer age.

Table 4.2 suggests that horizontal influx may be from 10-50% of the accumulation rate in the shallow cores. If winnowing, which we have so far neglected, is important, than these estimates are too low. This is because winnowing decreases the accumulation rate much more quickly than it is likely to have increased the mixed layer age, if it increases it at all.

The three rightmost columns in Table 4.2 also give a possible range of values for s_0 . The rightmost is from Table 4.1; it assumes that the carbonate in horizontal influx has the same age as that in the mixed layer; it therefore is a minimum of sorts. The two columns to the left of the rightmost give an s_0 found by subtracting the minimal s_h (columns 1 and 2) from the reported accumulation rates, s_r , in Table 4.1. These s_0 are the maxima consistent with our assumptions. These assumptions are that $s_w=s_D=0$, that $n_0=86\%$ and $n_h<75\%$, that the Z in Table 4.1 are correct, that the s_r in Table 4.1 are correct and equal to the true accumulation rate, s , that the correction for deep burrowing is 500-yr, and that eq (2.8b) holds.

Core	s_h (cm/kyr)		s_h/s_r		s_o (cm/kyr)	
	min	max	min	max	min	max
	$n_h=75\%$	$n_h=60\%$	$n_h=75\%$	$n_h=60\%$	$n_h=75\%$	$n_h=60\%$
ERDC 83	.5	.7	.16	.25	.45	2.3
ERDC 92	.1	.2	.07	.15	.19	1.4
ERDC 112	.6	.8	.21	.29	.51	2.0
ERDC 120	.2	.4	.09	.18	.18	1.8

Table 4.2. Horizontal influx to the shallow ERDC cores. Minimum rates of horizontal influx, s_h , assume that all carbonate coming in laterally is dead; we let $c_h=0$ in eq (2.8b) so that s_h follows from eq (4.3). For n_h , the carbonate fraction in the horizontal influx, we try two values, $n_h=75\%$ (least likely) and $n_h=60\%$ (most likely). Maximum rates of s_h are simply s_r-s_o in Table 4.1. Maximum s_o are s_r minus minimum s_h . Minimum s_o is that calculated from eq (2.8c) and given in Table 4.1.

Because of dissolution, finding a range for s_h in the deeper cores presents a more difficult problem. It may be that the departures in Fig 4.10 from the productivity curve are not due to dissolution of young carbonate but to increasing, downslope, horizontal transport. With the data at hand, the two alternatives cannot be unambiguously resolved.

However, it is instructive to plot $s_r - s_o$ vs. depth at core site. Fig 4.11 does this. Instead of using the calculated values of s_o from Table 4.1, the figure interpolates s_o from the primary productivity curve in Fig 4.10. We in effect here assume that the actual shape of the latitudinal variation of s_o matches that of the primary productivity curve. We let the zero point of the difference, $s_r - s_o$, be floating so that in fact we are plotting

$$s - s_o = s_h - s_D - s_w + \text{unknown constant.}$$

Thus we hopefully remove the latitudinal variation and leave only depth variation and local variation. Because we do not explicitly exploit mixed layer ages in this interpolation, we are justified somewhat in using Holocene s_p from Table 4.1 and not substituting present values for ERDC 79, 92, 123 from Fig 4.6. Likewise, we may include s_p from ERDC 129 and 141, even though these cores have no mixed layer.

Fig 4.11 shows a linear trend which becomes more negative with depth at core site. The trend, indicated by a dashed line, appears to start at about 2400 m. This may be the depth where horizontal influx starts to decrease or where winnowing or dissolution start to increase.

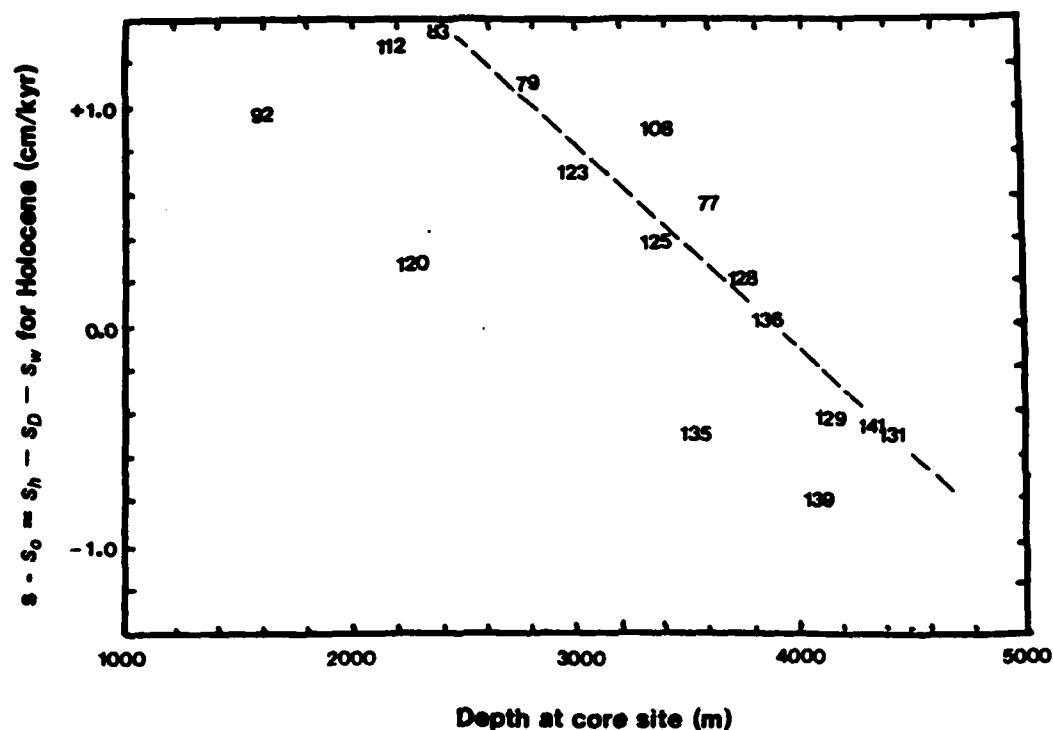


Fig 4.11. $s - s_0$ for the ERDC cores. Here the accumulation rate, s , is estimated by the reported Holocene rates, s_h , in Table 4.1. The rate of fresh sedimentation, s_0 , is taken from the curve of primary productivity in Fig 4.10. The dashed line indicates the trend of the deeper cores.

That the trend is linear suggests that it is due to dissolution. Petersen (1966) found a linear trend in dissolution loss in his experiment with moored calcite spheres. Similarly, Berger (1975) found a linear trend in sedimentation rate differences amongst DSDP cores from the eastern tropical Pacific. The slope of the trend that Berger found was 1 cm/kyr/km, which is close to that in Fig 4.11. It is unlikely

that the local processes of winnowing and horizontal influx would be the same in the DSDP cores and the ERDC cores. However, it is not inconceivable that the depth variation of dissolution be ocean-wide and more or less constant in time.

Scatter in Fig 4.11 about the trend is nearly the same as that in Fig 4.10. ERDC 120, 135, and 139 show large departures. The equatorial set of deeper cores, ERDC 123, 125, 128, 129, and 131 follow the trend closely. This may be because they all have the same s_0 ; any errors in the estimates of s_0 from the primary productivity curve affect all these cores equally. On the other hand, since these cores are concentrated in one area of the plateau (Fig 4.1b), it may be that the local effects -- horizontal influx and winnowing -- are similar.

The apparent dissolution losses in the ERDC cores should result in decreasing carbonate content with depth at core site. This indeed happens, according to Berger et al. (1977b). However, if horizontal transport is important, the relationship between carbonate and dissolution loss will not be as simple as that described above in Chapter 2, Section 2.2.1. Horizontal influx will contain an unknown fraction of carbonate, n_h . If the influx is mostly fine sediment, it will tend to decrease carbonate and give the appearance of dissolution loss.

3.3.2. s_0 from eq (4.2)

Even if this problem exists, it is worthwhile to tackle the question of sedimentation rates in the conventional way. We now proceed to do this. We estimate dissolution loss from carbonate changes and subtract this loss from reported accumulation rates to find another

estimate of s_0 .

Table 4.1 includes the carbonate fraction in the Holocene sediment of the ERDC cores. The values shown come from graphically averaging the carbonate fraction (Fig 4.8) from depth z_2 (Table 4.1) to the surface. (The average does not include the measurement at 0-1 cm; this sample may be affected by water sloshing in the box core during retrieval; see Section 3.2, above). Although somewhat sensitive to the choice of z_2 , the average lessens the effects of measurement error and sediment mixing.

If we neglect winnowing and horizontal influx and assume steady state, the formula (Heath and Culberson, 1970) for dissolution loss is

$$\frac{s_D}{s_0} = \frac{n_0 - n}{1 - n} . \quad (4.4)$$

Here we use averages in time for the observed carbonate fraction, n , and for the carbonate fraction, n_0 , in fresh sediment. We take n_0 to be the Holocene average of the carbonate fraction in the shallow cores (Table 4.1). This average appears to be from 84% to 86%. In what follows, we use $n_0=86\%$.

That the carbonate fraction in all the shallow cores is more or less the same is intriguing in itself. The carbonate fraction stays constant even though primary productivity and probably s_0 vary by a factor of 2 or more (Fig 4.10). Now, according to Lisitzin (1970), there is less than 1% amorphous silica in the sediments of Ontong-Java Plateau. (Mikkelsen's (1978) study of diatom preservation in the ERDC cores suggests that most of the incoming silica dissolves). Therefore,

the major part of the non-carbonate must be clay minerals and quartz. Yet to keep the carbonate fraction, n_o , constant, the sedimentation rate of these terrigenous minerals must be strongly correlated to productivity. The idea that these minerals form a uniform rain independent of productivity cannot hold over Ontong-Java Plateau in the Holocene.

One possible explanation for this correlation between sedimentation of terrigenous minerals and productivity is that the clays and quartz reach the seafloor via fecal pellets. Fecal pellet production is likely to be strongly correlated with the carbonate supply, $n_o s_o$, and primary productivity. Transport of terrigenous minerals by fecal pellets is known to occur (Davis and Gorsline, 1976; Dunbar and Berger, 1979).

Another possible explanation is that the terrigenous minerals have a higher concentration in the equatorial undercurrent, which is restricted to within a degree or two of the equator (Philander, 1973). That the undercurrent comes from the west, the nearest source of terrigenous sediment, is an argument in favor of this explanation.

In any case, whichever is the correct explanation, n_o does appear to be independent of latitude over Ontong-Java Plateau. Using 86% and substituting this and values for n from Table 4.1 in eq (4.4), we get Fig 4.12, which shows calculated dissolution loss vs. depth at core site. The trend, indicated by the solid line, appears to begin at 3000 m.

Scatter from the trend in Fig 4.12 is surprisingly small. ERDC 141 and ERDC 77 are the only cores out of 11 which depart significantly.

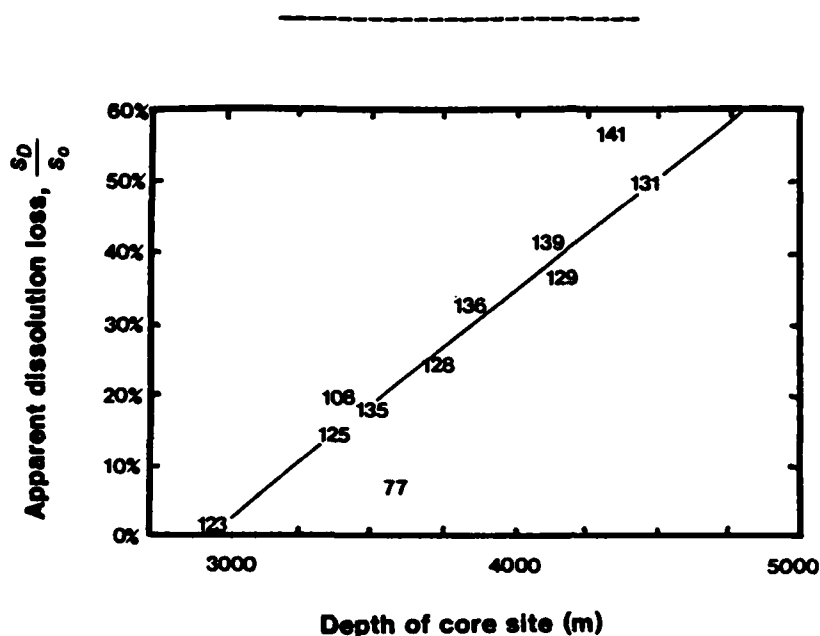


Fig 4.12. Calculated Holocene dissolution loss vs. depth at core site for the ERDC cores. We use eq (4.4) with $n_0=86\%$. The n in this equation are the Holocene averages in Table 4.1. The solid line shows the trend.

Proportional to the total change, the scatter introduced by even these two cores is small compared to that in Figs 4.10 and 4.11.

Why the scatter is small is not immediately obvious. To appreciate this, we calculate an s_0 from the losses ($\frac{s_D}{s_0}$) and from the reported accumulation rates (s_r) in Table 4.1. Since we have assumed that horizontal influx and winnowing are small,

$$s_r \approx s = s_0 - s_D = s_0 - \frac{s_D}{s_0} s_0.$$

or,

$$s_o = \frac{s_r}{1 - \frac{s_D}{s_o}}.$$

Fig 4.13 shows s_o calculated in this way vs. latitude. The figure is analogous to Fig 4.10. Here we make no use of the mixed layer age. Fig 4.13 includes the shallow cores. For these cores, $s_o = s_r$, with no winnowing or horizontal influx. As before primary productivity averaged from Rotschi et al. (1972) is superimposed, the scale being relative to equatorial values. Two values for ERDC 77 are plotted; one uses the dissolution loss calculated from its carbonate fraction in Table 4.1; the other (in parenthesis) uses a loss interpolated at ERDC 77's depth from the trend in Fig 4.12.

The s_o in Fig 4.13 appear to decrease with latitude but the scatter is large. It is clear that one or more of our assumptions has been violated. The assumptions in computing the s_o in Fig 4.13 are

- 1) that winnowing, erosion, and horizontal influx
are negligible,
- 2) that changes in carbonate reflect changes in dissolution,
- 3) that $n_o = 86\%$ everywhere and always,
- 4) and that the ^{14}C dates at z_1 and z_2
in Table 4.1 straddle equivalent periods.

The last assumption is not very stringent, unless s_o or n_o varied greatly over longest period sampled. In the extreme case of ERDC 135, the deepest sample has a date of 22.3 kyr BP (Table 4.1). Can this penetration into the pre-Holocene be the reason that ERDC 135 shows a

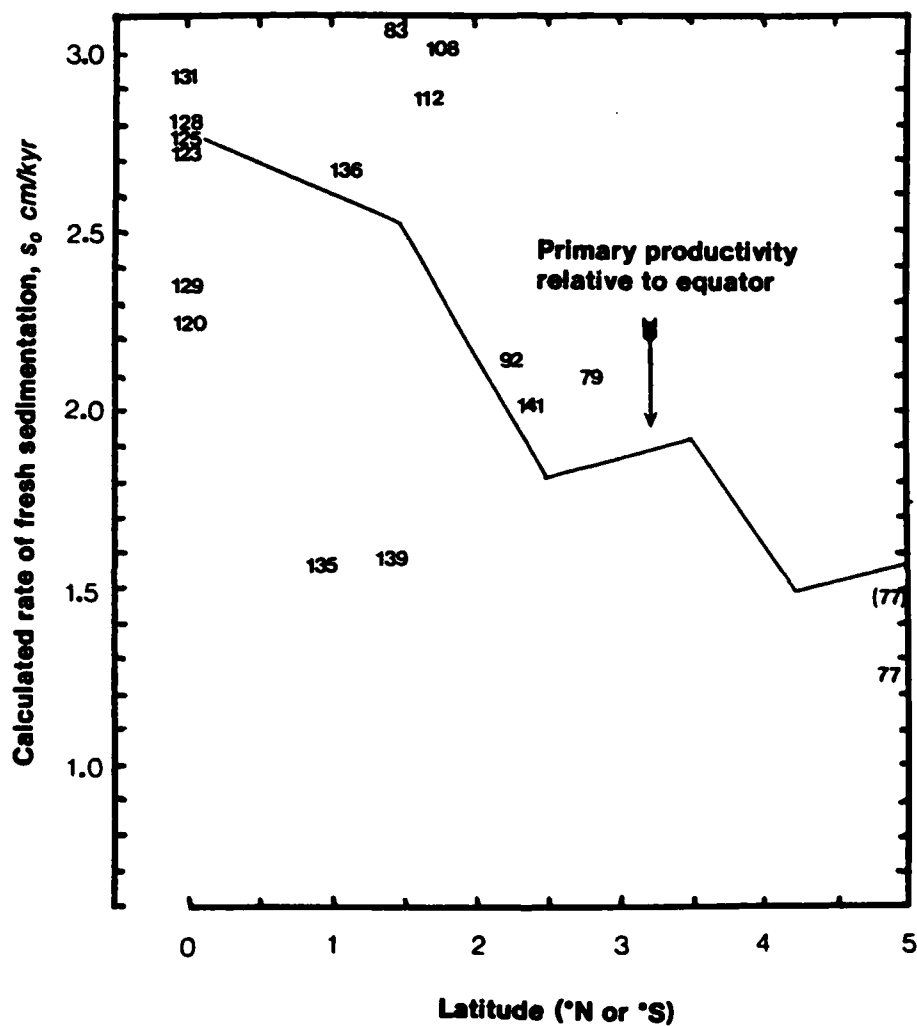


Fig 4.13. Calculated s_o vs. latitude, using dissolution loss from carbonate percentages and reported accumulation rates. Primary productivity averaged from Rotschi et al. (1972) is superimposed as in Fig 4.10. The two values for ERDC 77 are explained in the text.

low s_0 in Fig 4.13? No. With a Holocene rate of, say, 2.7 cm/kyr (from the "trend" in Fig 4.13), the pre-Holocene s_0 must have been essentially zero to give the s_0 calculated for ERDC 135. Zero, of course, is not a likely value. A similar argument can be made for ERDC 139. These two cores, and perhaps ERDC 120 and 129, have evidently suffered erosion between z_1 and z_2 .

Fig 4.13 also seems to indicate that some cores have gained material: ERDC 83, 108, and 112. That ERDC 108 has is not surprising, since it was recovered from the bottom of a major valley (Fig 4.1). On the other hand, it may be that n_0 on the equator is slightly higher than elsewhere. ERDC 120 does not show this but ERDC 123 has a short interval with carbonate fraction as high as 88% (Fig 4.8a). If this equatorial maximum is true, this would increase the calculated values of s_0 at the equator in Fig 4.13. For $n_0=88\%$, the increase in s_0 would be about 10%. This would shift the "trend" set by the primary productivity curve higher and so reduce the apparent horizontal influx to ERDC 83, 108, and 112.

Winnowing alone -- that is, without co-occurring horizontal influx -- does not appear to be responsible for the scatter in Fig 4.13. In fact, winnowing alone does not appear to have a significant effect on the accumulation rates on Ontong-Java Plateau. This follows from the carbonate values in Table 4.1. On average, with only winnowing and dissolution, the carbonate flux into and out of a stack of sediment must balance like this:

$$\text{accumulation} = \text{fresh flux} - \text{dissolution flux} - \text{winnowing flux}$$

or, in symbols,

$$ns = n_o s_o - s_D - n_w s_w . \quad (4.5)$$

Here n_w is the carbonate fraction in winnowed material. Using $s = s_o - s_D - s_w$, we solve for n :

$$n = \frac{n_o - \frac{s_D}{s_o} - n_w \frac{s_w}{s_o}}{1 - \frac{s_D}{s_o} - \frac{s_w}{s_o}} .$$

Table 4.3 shows some instructive calculations with this formula and the assumption that $n_o = 86\%$.

$\frac{s_D}{s_o}$	$\frac{s_w}{s_o}$	n	
		$n_w = 75\%$	$n_w = 60\%$
0.0	.1	87%	89%
	.2	89%	92%
0.3	.1	81%(.26)	83%(.17)
	.2	82%(.22)	88%(<0)

Table 4.3. Effect of winnowing on carbonate fractions. The calculations use eq (4.6) with $n_o = 86\%$. Numbers in parentheses are apparent dissolution loss without taking winnowing into account, i.e., loss found from eq (4.4).

If n_0 is indeed 86%, and if we neglect horizontal influx, then Table 4.3 and the Holocene carbonate averages, n , for the shallow cores clearly do not indicate quantitatively significant winnowing. Of the deeper cores only ERDC 77 appears to be strongly winnowed: The fractions in parentheses in Table 4.3 are the apparent dissolution losses $(\frac{s_D}{s_0})$ which we would calculate from the carbonate fraction, n , had we neglected winnowing. In Fig 4.11 we did just that -- neglected winnowing. Given that $n_w=75\%$, we might be able to attribute some of the scatter in Fig 4.11 to slight winnowing. But the tightness of the trend in that figure suggests that in general winnowing is of no quantitative significance in the long-term accumulation rates of the deeper cores.

A full description of winnowing should include measurements of coarse fraction. Such measurements are available for the ERDC box cores but are not included here. Sediment disaggregation for these measurements was done by ultrasonication. This process apparently results in coarse fraction values much smaller than disaggregation by a gentler method. We will discuss this in more detail shortly.

As it is, inter-core comparisons of the coarse fraction data are confusing. Take, for instance, the case of ERDC 77, whose carbonate content suggests 10-20% winnowing. The available coarse fraction data show this core to have finer Holocene sediment than ERDC 128 and 135, both of which are on the trend in Fig 4.12. If winnowing is indeed important at the site of ERDC 77, it should have a higher coarse fraction than either of these two cores. It may be that other processes are at work or it may be that the length of time of ultrasonication varied

from one core to another.

3.3.3. Isochronal layers

We turn now to isochronal layers, whose presence in a number of the ERDC cores seems to give further evidence for the importance of horizontal sediment influx.

ERDC 79 and 92 show several isochronal layers (Fig 4.6). ERDC 88 has one which is apparently 12 cm thick (see data in Krishnamurthy et al., in press). Also, photographs of core 120 (see Berger et al., 1977) show a distinct light-colored layer 5 cm thick; oxygen isotopes from this layer seem displaced (see Berger and Johnson, 1978).

Possible causes for these isochronal layers include:

- 1) turbidity currents and slumps,
- 2) holes dug by large animals which are later filled with local mixed layer material,
- 3) deep-burrowing in the sense modeled in Chapter 2; also deep burrows, which collapse and mix sediment in place;
- 4) and sudden decreases in mixed layer thickness,

Each of these possibilities has a signature in the ^{14}C record (Fig 4.14).

Most isochronal layers in ERDC 79 appear to have the signature of a turbidity current or slump which brings in sediment of the same age as the mixed layer. ERDC bathograms show that this core was taken in a small valley about 2 km from a 40° slope (Fig 4.1b). The walls of the

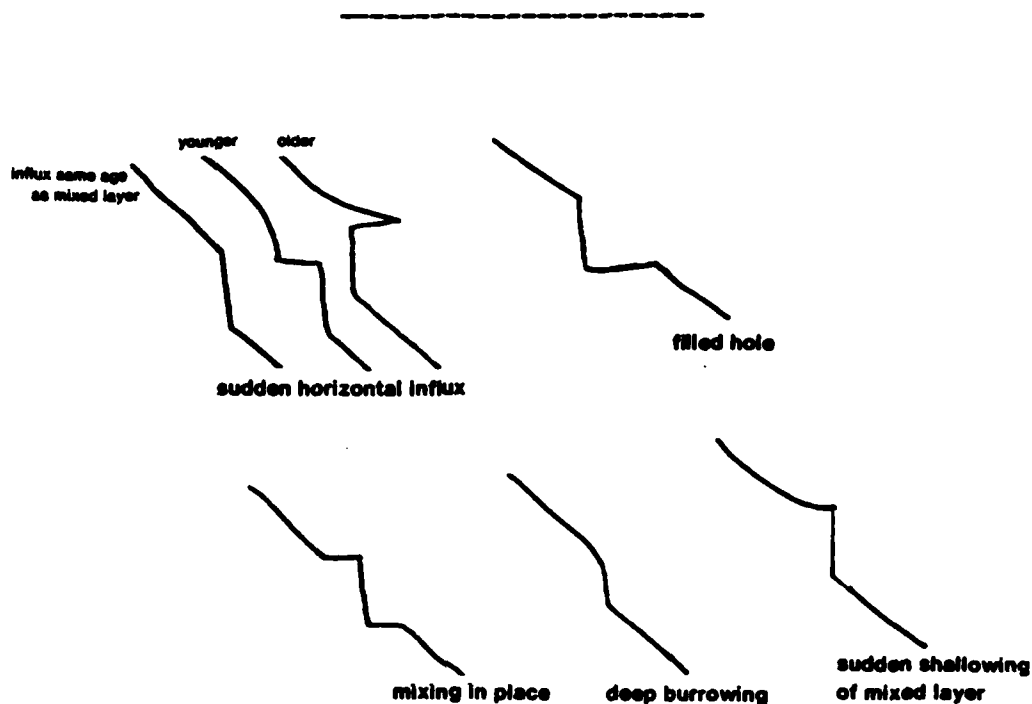


Fig 4.14. ^{14}C signatures of isochronal layers of various origins. Signatures are plotted as if in a figure such as Fig 4.6: The horizontal is reported ^{14}C and the vertical is depth in core. The isochronal layers shown are assumed to be a few to several cm thick.

valley at the point of this slope are about 80 m high.

A puzzling feature of the isochronal layers in ERDC 79 is that species abundances change within them (Fig 4.18a, below). Coarse fraction can change also (Fig 4.17, below); two of the layers -- the ones at 12 cm and 30 cm -- are distinctly coarse. This means that, if the layers do result from horizontal influx, the influx contains coarse material.

The isochronal layer in ERDC 92 (Fig 4.6) also appears to be due to a sudden horizontal influx. In this case, the influx may have been slightly older than the contemporaneous mixed layer. My interpretation (Fig 4.6) shows the post-influx mixed layer slowly recovering to the age set by the normal sedimentation. ERDC 92 may also have a second isochronal layer between 25 and 28 cm. My interpretation in Fig 4.6 ignores this. I wanted to show the gradual change in slope associated with a sudden change in s_0 ; the isochronal layer merely confuses the picture.

3.3.4. Summary of sedimentation rates

To sum up, the sedimentation rates on Ontong-Java Plateau apparently show local effects superimposed on a more general scheme. The general scheme consists primarily of a sharp decrease away from the equator and a linear decrease with depth. For the Holocene, the latitudinal breakpoint occurs between 1.5° and 2.5° latitude. Equatorward of this point, the supply of fresh sediment seems to be 2-3 cm/kyr; poleward, the supply seems to be about 1 cm/kyr.

The depth effect begins somewhere between 2500 m and 3000 m. Below this, accumulation rates decrease at about 1 cm/kyr/km. However, because local effects can account for 10-50% or more of the accumulation rate, these characterizations of the general scheme are only tentative.

The local effects themselves appear to consist of horizontal influx and erosion. The occurrence of isochronal layers in a number of cores suggests that slumps or turbidity currents may play an important role. Winnowing does not appear to be an obvious factor; if it occurs,

it occurs in conjunction with other local effects which mask its presence or it occurs to a similar degree in all cores.

4. ERDC box core stratigraphies

We are now prepared to examine ERDC box core stratigraphies. In the first part of this chapter, we learned from a discussion of the literature that "ground truth" was hard to come by in the western equatorial Pacific. In the second part, we verified that sediment mixing as described in Chapter 2 occurs on Ontong-Java Plateau, at least in the majority of the cores. We also learned that local effects are important there.

In the present chapter, we will look primarily at the stratigraphies of ERDC 79 and ERDC 83. ERDC 83 is from 2342 m and 1°24'N; ERDC 79 is from 2767 m and 2°47'N (Fig 4.1). According to the data in Table 4.1, the latitude of ERDC 83 in the Holocene has been one of high productivity; the core's depth has been one of minimal calcite dissolution. On the other hand, the latitude of ERDC 79 has been a latitude of distinctly lower productivity; its depth has been a depth of perhaps some dissolution (Fig 4.11).

In what follows, the order of business is this: First, we briefly consider methodology — how an assistant and I sampled the cores, how Sam performed, and how I processed its data. We then turn to the stratigraphy of dissolution and productivity in the box cores. In this context, ERDC 79 and ERDC 83 are not as instructive as ERDC 128 and 92. With the apparent changes in dissolution and productivity in mind, we finally discuss the machine-counted micropaleontology of ERDC 79 and

ERDC 83. The most important feature of this data is the abruptness and date of the deglacial transition and the variation of certain phenotypes.

4.1. Methods and data

4.1.1. Sampling; grain size and carbonate analyses

For ERDC 79 and 83, we extruded all the sediment from one of the subcores. (The subcores are plastic cylinders about 8 cm in diameter). We sliced the extruded material into disks about 1 cm thick. For ERDC 79, we cut these disks into 3 portions, A, B, and C. Portion A was about 10g wet and the other two were about 35g wet. We kept B and C separate always as replicates. Portion A we subdivided as replicates for grain size and carbonate analysis. Portions B and C we soaked for 30 minutes in a buffered 5% solution of H_2O_2 while on a 62 μ sieve. The fraction >62 μ we dried, weighed, and resieved at 355 μ and 840 μ . The fraction 355-840 μ went to Sam.

We treated ERDC 83 in a similar fashion except that we cut the extruded disks into only two portions (say, B and C). We did not do any grain size or carbonate analysis on this subcore. Some information on these two parameters was already available, although not at 1-cm intervals. The earlier grain size was done using an ultrasonicator to disaggregate the sediment. The analysis we did on portion A of ERDC 79 used the H_2O_2 technique described above for disaggregation. Fig 4.15 compares the analysis of portion A with an earlier analysis of a different subcore of ERDC 79 which used ultrasonication. The length of time which samples were ultrasonicated in the earlier analysis is un-

known but may have been as long as 5 minutes.

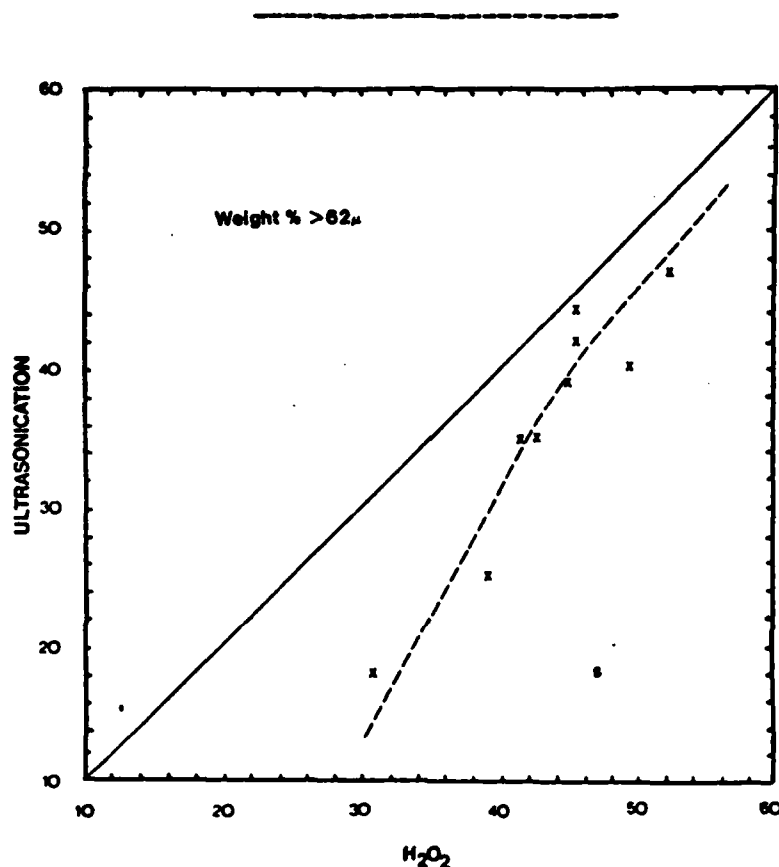


Fig 4.15. Comparison of grain size analyses for ERDC 79 done with two methods of disaggregation: ultrasonication and H_2O_2 . In the earlier measurements, D. Ripley ultrasonicated the samples for something less than 5 minutes to disaggregate the sediment; we used H_2O_2 . Values of weight percent >62 μ from the same depths in core are plotted against each other. The dashed line is the trend fitted by eye. The point marked S is the surface (0-1 cm) sample; the others, marked X, are distributed about every 4 cm down core.

Clearly, Fig 4.15 shows that the two methods of disaggregation

do not produce the same results. Largest differences are between finer samples. (The point marked S in Fig 4.15 is the sample from 0-1 cm; its value may be affected by water sloshing in core recovery (see Section 3.2 above), so it is not surprising that two different subcores have wildly different values at this level).

The two methods of disaggregation may yield different results for either or both of two reasons: First, ultrasonication may break many of the shells in the coarse fraction into fine fragments. That the difference between the two methods increases with increasing fine fraction supports this possibility; the increase in fines (in ERDC 79) is due for the most part to increasing dissolution, which weakens the coarser particles. The second reason for the difference is that the H_2O_2 may not clean the larger shells of all the fine particles trapped within. Microscopic observation does not show this to a noticeable extent.

For the 1-cm carbonate analysis of ERDC 79, we used the same technique which produced the data in Fig 4.8. The technique measures the volume of CO_2 evolved when a small sample (<1 g) is dissolved in, say, 3M HCl. A comparison of the earlier analysis of ERDC 79 (run by Dave Ripley and/or Matt Christiansen) and our own (run by Steve Vierra) appears in Fig 4.16. The comparison shows that the variance between technicians ($\sigma < 1.5\%$) is not much different from variance between replicates (Fig 4.17, below). Fig 4.16 appears to show a small (<1%) systematic difference between technicians.

The grain size and carbonate analyses from portions A of ERDC 79

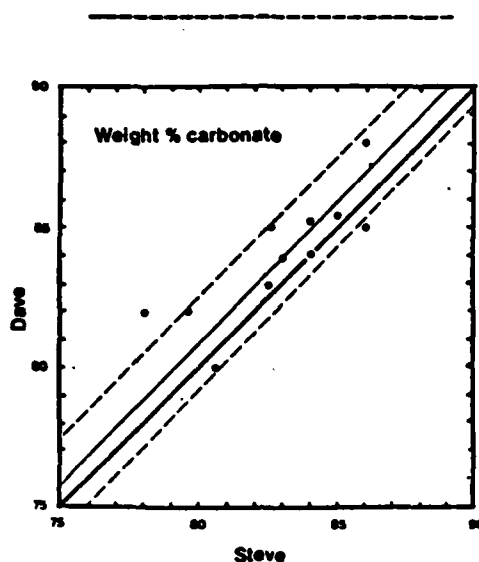


Fig 4.16. Comparison of carbonate measurements on ERDC 79 by two different technicians at widely separated times. Both technicians used the same technique. The thick solid line is the line of perfect agreement. The thin solid line is the trend line fitted by eye. The dashed lines are $\pm 1.5\%$.

appear in Fig 4.17. The points marked as 1 and 2 are the replicates Steve Vierra did at each level. The points marked M are the mean of the replicates. Plotting was done by a line printer so that resolution is one printer line; some of the replicates plot on top of each other or the mean, in which case only the M appears.

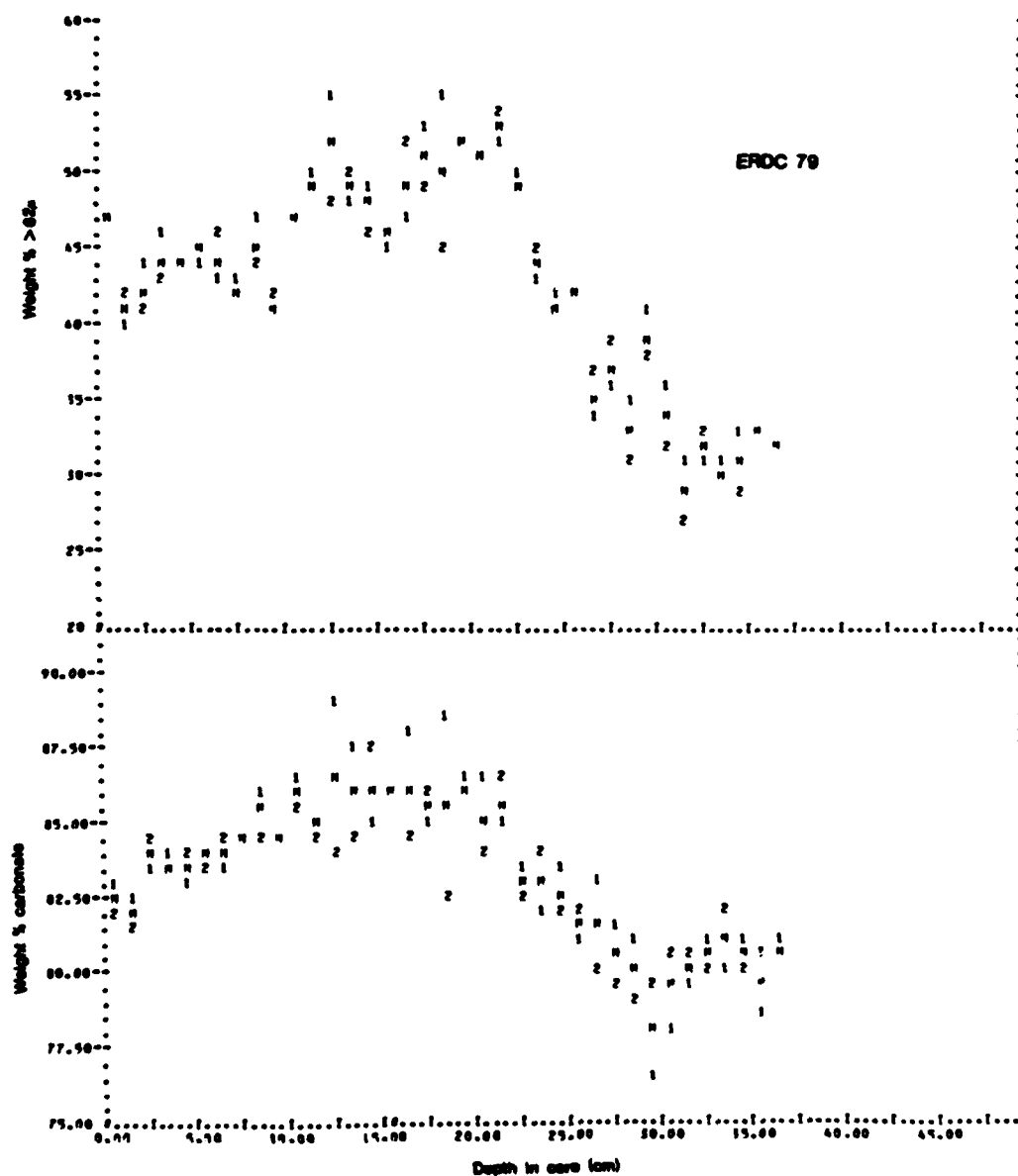


Fig 4.17. Grain size and carbonate analyses for ERDC 79. Digits represent replicates; the M's are their means. If a digit is missing at a given level, it was overprinted by the mean.

4.1.2. Sam's data and performance

For Sam, we split the 355-840 μ fraction of portions B and C with a microsplitter. These splits, of about 5000 shells each, constituted one run on the machine. The splits were about one-eighth of portion B or C, so that, not counting various mechanical "leaks" (see Chapter 3), there are of the order of 64,000 shells per cm in shallow ERDC box sub-cores (8 cm in diameter). For the two cores discussed in this chapter, total count was approximately 450,000 shells.

Fig 4.18a-s are Sam's output for ERDC 79 and 83. For a given curve, the plotted digits represent sample values, separate digits at a single depth in core being from the portions B and C. Solid curves are the means of B and C, if both were run, weighted by the relative counts. In this case, a Tektronix terminal did the plotting, so resolution is about 1/500th of the size of each-plot.

In Fig. 4.18a, ^{14}C data from Fig 4.6 is superimposed. The dashed vertical lines are what I estimate to be the limits of isochronal layers.

Some of the curves in Fig 4.18 show "measured" values. These are what Sam reported. Other curves show "calibrated" values. These curves have been corrected for Sam's bias, as discussed in Chapter 3. The few curves of measured abundance (Fig 4.18m,n,o,p) show dotted lines which represent 95% confidence limits from counting statistics at each level. These particular curves are shown because I expected them to be extreme cases. Other measured abundances indicate that the replicate portions fall within counting error and are not shown.

Fig 4.18a. Calibrated abundance of G. menardii and P. obliquiloculata in ERDC 79.

In these and the subsequent plots in this series, digits mark data points. Two points at the same depth in core are replicates from different portions of the one-cm thick disks of sediment extruded from each core. The core number is in the upper left-hand corner of each plot.

In these and subsequent plots, the X's pointed to by arrows are spot checks by manual count. Where necessary, a 95% confidence limit (based on the count size of the check) is attached to the X.

Fig 4.18a includes the profile of ^{14}C from Fig 4.6 with isochronal layers demarcated by vertical dashed lines. The profile here shows two ^{14}C curves: One is merely the data points connected by straight lines. The other is an interpretation which takes into account the 2-cm thickness of the samples. The interpretation shown is slightly different from that in Fig 4.6; it shows an isochronal layer between 22.5 and 24.5 cm.

Fig 4.18b. Calibrated abundance of G. menardii and P. obliquiloculata in ERDC 83. Notice that the scale for P. obliquiloculata in ERDC 83 (Fig 4.18b) is shifted 10% relative to that in ERDC 79 (Fig 4.18a).

Fig 4.18c. Calibrated abundance of G. dutertrei and ' in ERDC 79.

Fig 4.18d. Calibrated abundance of G. dutertrei and in ERDC 83.

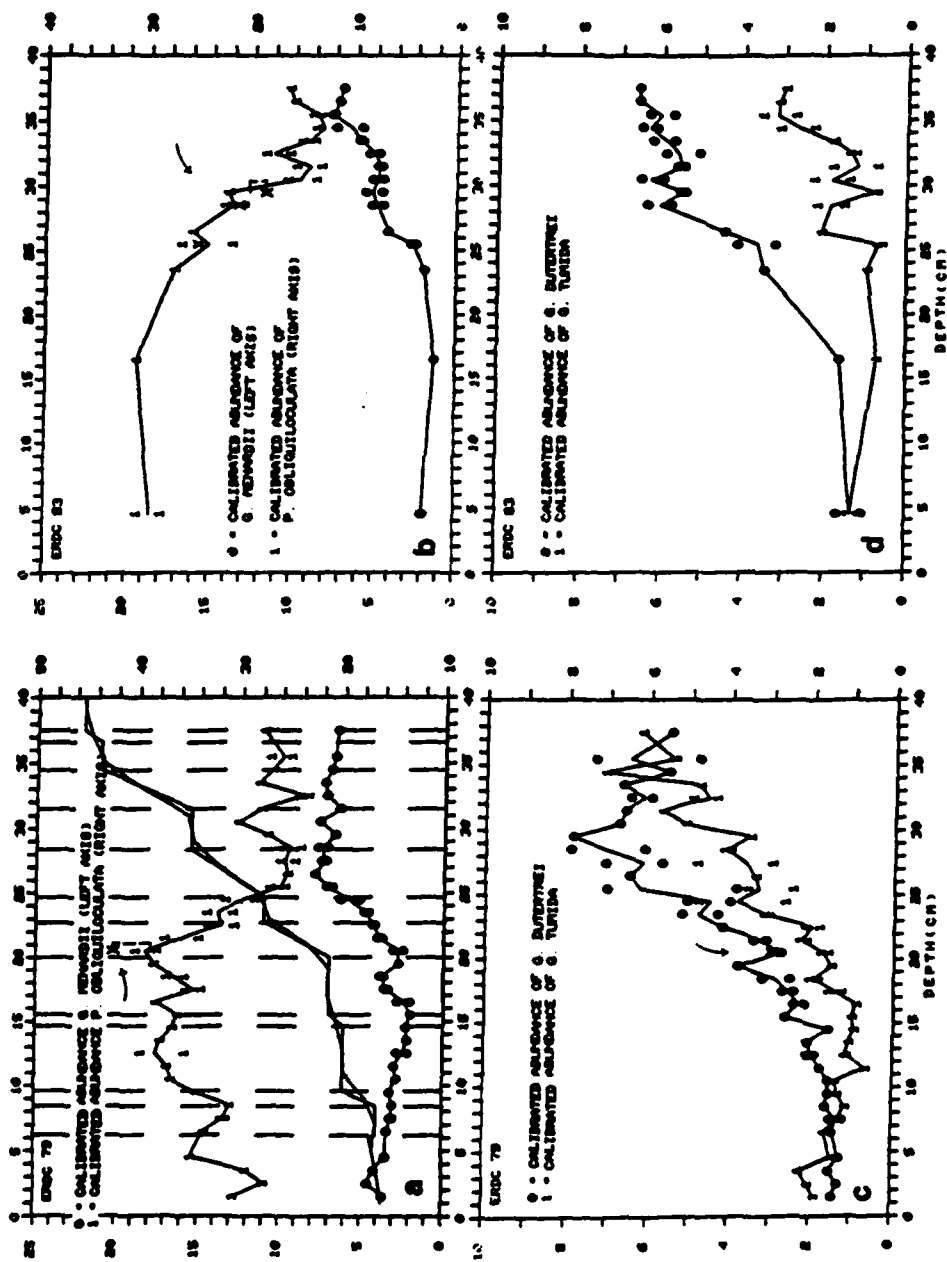


Fig 4.18e. Calibrated abundance of G. conglomerata in ERDC 79.

Fig 4.18f. Calibrated abundance of G. conglomerata in ERDC 83.

Fig 4.18g. Calibrated abundance of cold group and both phenotypes of G. sacculifer in ERDC 79.

Fig 4.18h. Calibrated abundance of cold group and both phenotypes of G. sacculifer in ERDC 83.

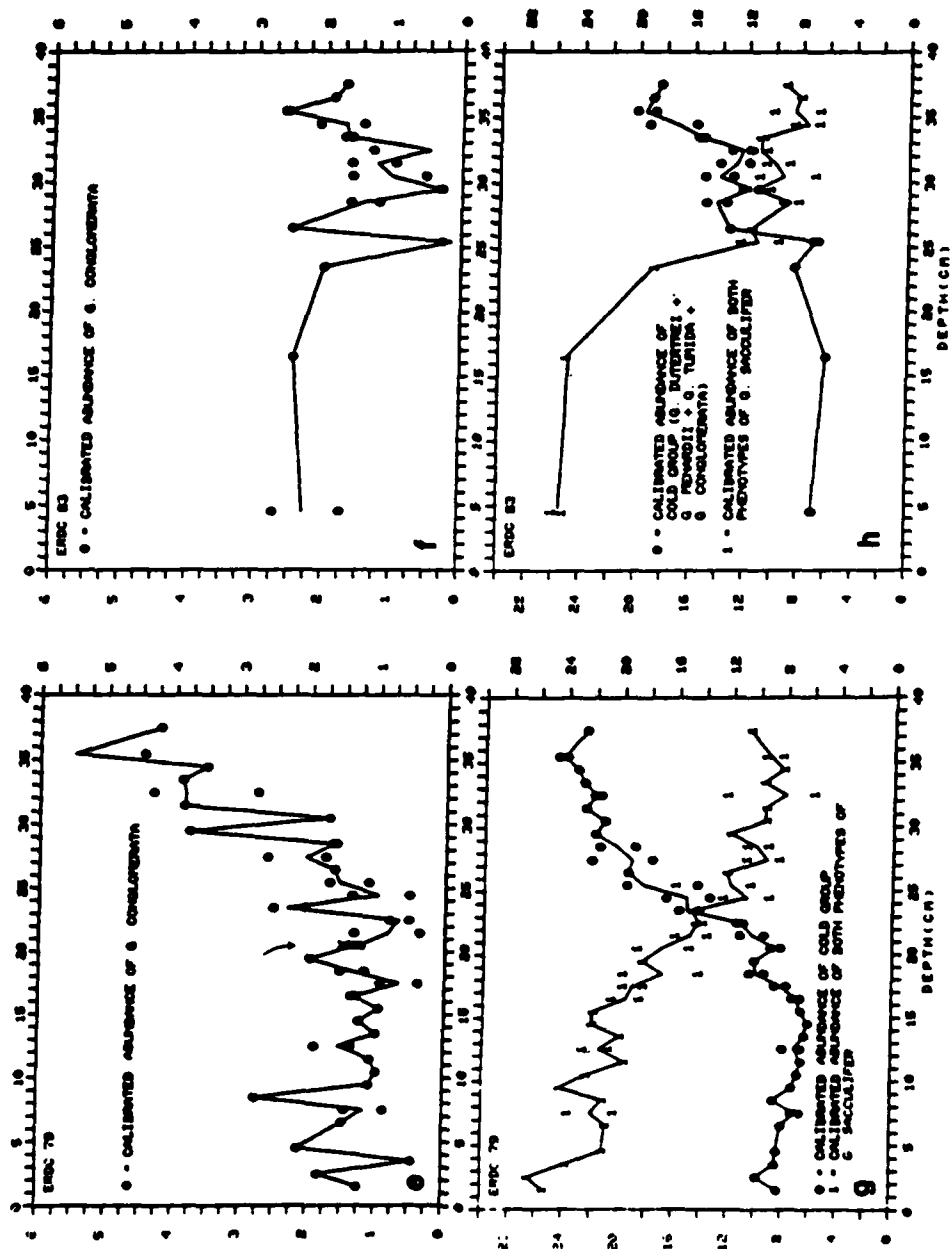


Fig 4.18i. Calibrated abundance of G. sacculifer trilobus and G. sacculifer sacculifer in ERDC 79.

Fig 4.18j. Calibrated abundance of G. sacculifer trilobus and G. sacculifer sacculifer in ERDC 83.

Fig 4.18k. Calibrated mean diameter of P. obliquiloculata, calibrated max diameter of G. sacculifer trilobus, and calibrated mean diameter of G. menardii in ERDC 79.

In this plot and the next (Fig 4.18l) and in Fig 4.18s, as well, the measurements are averages. That is, the measurements of maximum diameter are averages of the maximum diameter of, say, 500 specimens; the measurements of mean diameter are averages of the mean diameter of, say, 500 specimens. The actual number of specimens can be estimated by assuming that the total count for one replicate is 5000. Multiply this number times the species abundance and the counting efficiency (Table 3.5, p_{11}).

Fig 4.18l. Calibrated mean diameter of P. obliquiloculata, calibrated max diameter of G. sacculifer trilobus, and calibrated mean diameter of G. menardii in ERDC 83.

Fig 4.18m. Measured fragment abundance in ERDC 79. In this and the other plots on this page, the dotted lines are 95% confidence

Fig 4.18n. Measured fragment abundance in ERDC 83.

Fig 4.18o. Measured abundance of G. aequilateralis and ratio of radii of ultimate and penultimate chambers in kummerform G. aequilateralis in ERDC 79.

Fig 4.18p. Measured abundance of G. aequilateralis and ratio of radii of ultimate and penultimate chambers in kummerform G. aequilateralis in ERDC 83.

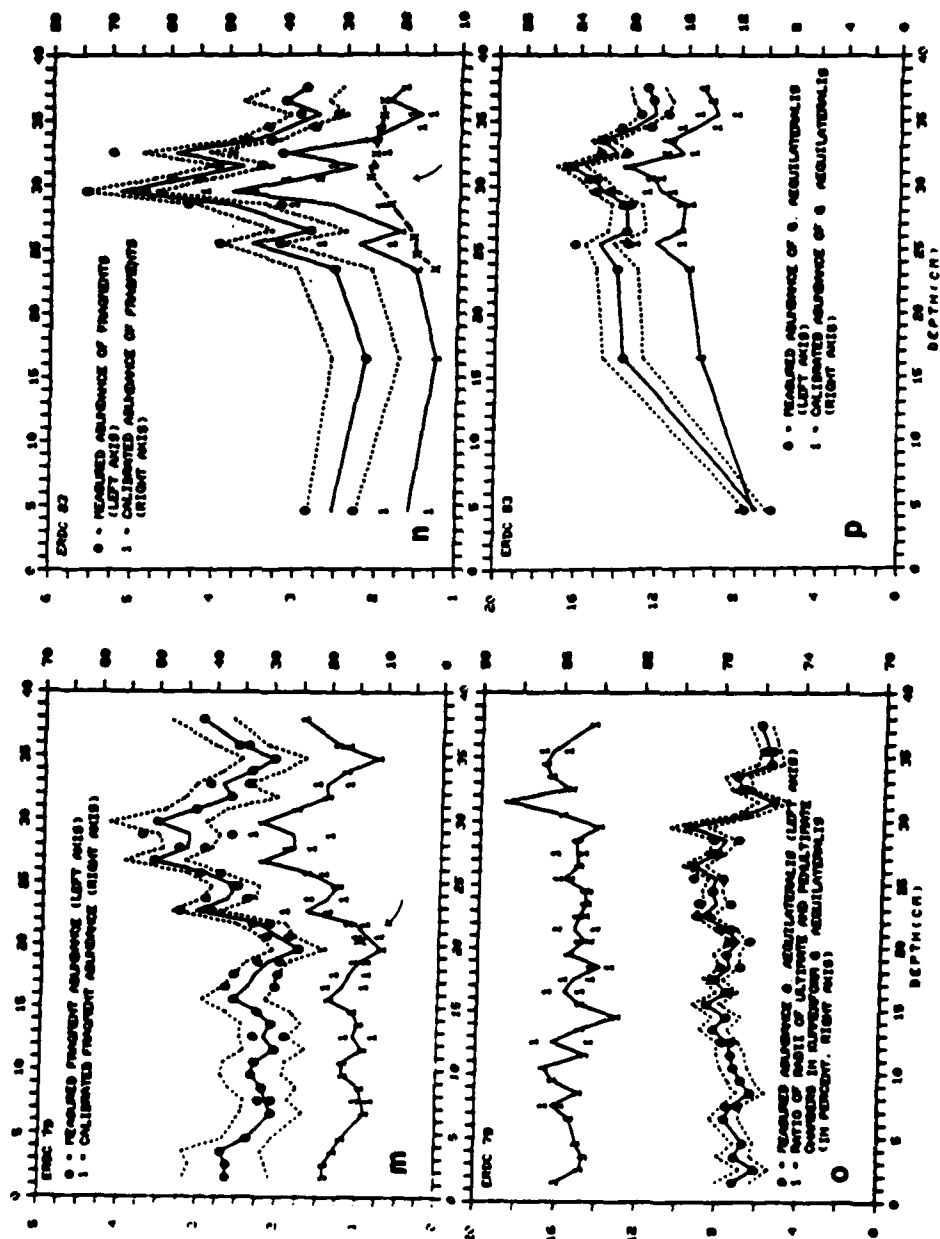
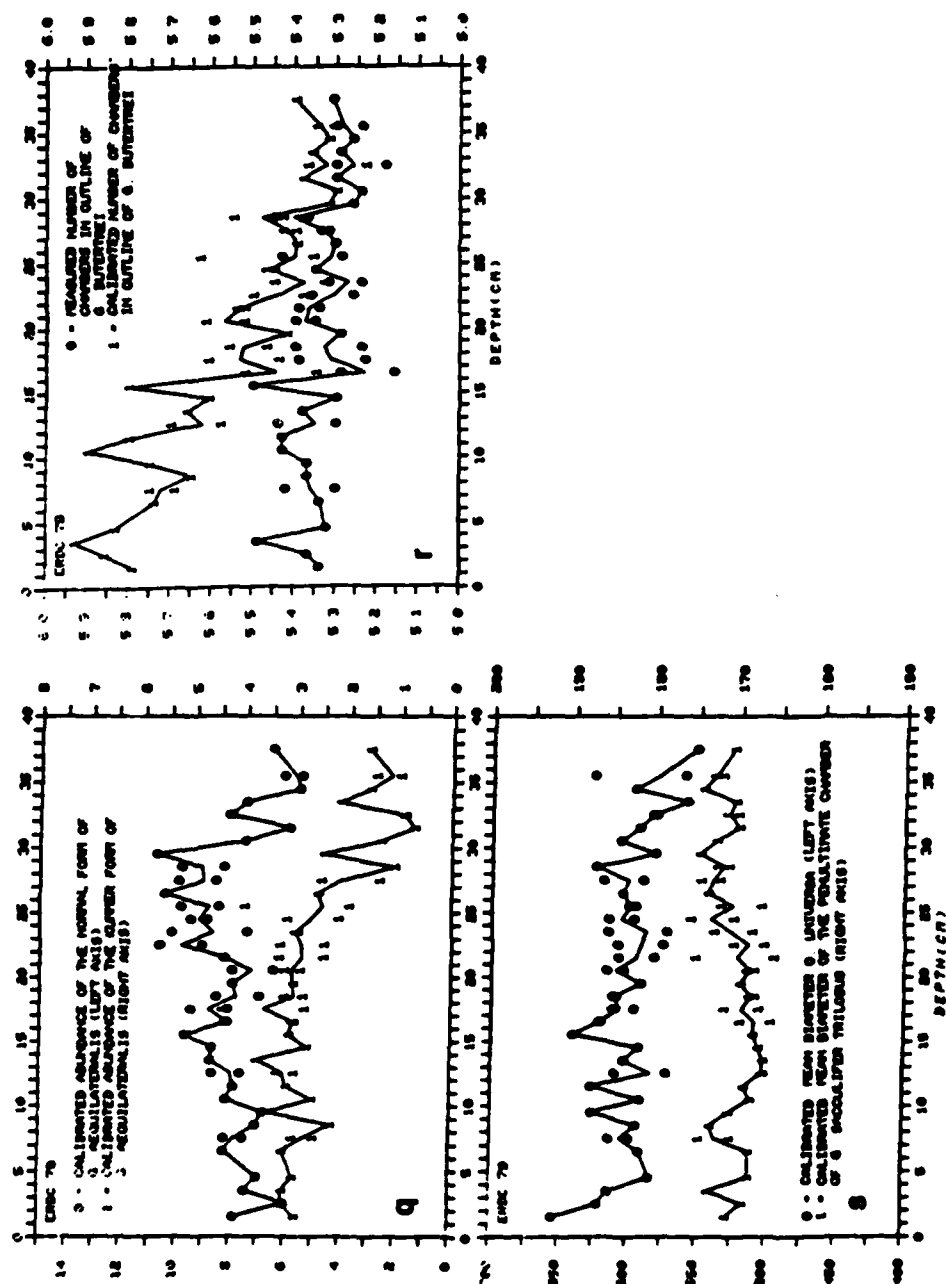


Fig. 4.18q. Calibrated abundance of the normal form and kummerform of G. aequilateralis in ERDC 79.

Fig 4.18r. Measured and calibrated number of chambers in the outline of G. dutertrei in ERDC 79

Fig 4.18s. Calibrated mean diameter of O. universa and calibrated mean diameter of penultimate chamber f G. sacculifer trilobus in ERDC 79.



In general, the measured values uncorrected for bias are of no particular interest. Two cores which show different measured abundances of some species, say, species A, can in fact have the same true (or calibrated) abundances for this species. Thus, if species B Sam sometimes calls A, and if B but not A varies between the two cores, the "measured" abundance of A will vary but (if the original calibration is correct) the "calibrated" value of A will not.

4.1.2.1. Sam's performance

Sam seems to have performed reasonably well. Its most notable characteristic is consistency. When I ran random splits from the same portion, the results consistently fell within counting error. This was true even when the runs were separated by weeks. Thus, drift in light intensity and digitizer noise did not seem to affect the counts. (On some early runs -- not included here -- I did have a problem with temperature drift in the TV camera. The solution was to leave the camera on continuously, with a fan to keep it cool.)

The replicates in Figs 4.18a-s include variance due to washing and sieving. Most of this variance must come from fragmentation. According to Table 3.5, Globigerinella aequilateralis is the most sensitive species in this size fraction. This is also the species whose fragments Sam recognizes best (Table 3.5).

Figs 4.18m,n show the measured fragment abundance and the 95% confidence limits from counting statistics. The limits are based on the total count at each level, so that each replicate (which is about one-half the total count) has limits 1.4 times as large. For ERDC 79, only

two samples (out of 48) fall outside the limits.

Figs 4.18o,p show the measured abundance of G. aequilateralis and its 95% confidence limits. For ERDC 79 (Fig 4.18o), 7 samples fall outside the limits as drawn but only one falls outside limits 1.4 times as large.

These figures seem to indicate that washing and sieving (as we did it) does not add enough sample-to-sample variance to this particular foraminiferal assemblage to be detectable at counts of about 8,000.

Sam counts the species in Figs 4.18a,b efficiently (79% hit rate for Pulleniatina obliquiloculata and 74% hit rate for Globorotalia menardii; Table 3.2). For this reason the curves appear smooth. Figs 4.18e,f show a species which Sam counts inefficiently (hit rate 26%). The process of converting "measured" values to "calibrated" values mostly multiplies the actual value by the inverse of the efficiency — that is, attenuation is usually more important than cross-talk as Sam is now programmed. This has the effect of amplifying the counting noise. Figs 4.18e,f show this.

Spot checks of Sam's "calibrated" counts appear as X's in Figs 4.18a-n. (For convenience, a small arrow points to the X's). In these checks, I counted about 1000 specimens under an ordinary microscope. Where necessary (Figs 4.18a,b), I have attached a 95% confidence interval based on the counting statistics of the check-count.

For the most part, the spot checks agree with Sam's "calibrated" count. The notable exception is Fig 4.18n. Here Sam's count shows a

large error in fragment abundance at 28-31 cm. The source of this error is a stain on the shells in this interval. The stain -- probably MnO_2 -- decreased the visual contrast between some of the shells and the background. As a consequence, the video digitizer reported ragged outlines to Sam. Since ragged outlines are one of the characteristics of fragments, Sam classified some of these stained shells as fragments.

At 29 cm, the worst case, Sam counted 5-6% fragments, about 3% more than it should have. Due to the 90% attenuation in its ability to recognize fragments (Table 3.2), calibration amplified the additional 3% into 30%. Instead of the correct value of about 25% fragments, the "calibrated" value at 29 cm is about 55%.

The staining may have affected Sam's counts of other "species" slightly. The slightly low value for Pulleniatina obliquiloculata at 29 cm (Fig 4.18b) may be an example. Other species show slight perturbations at this level (Fig 4.18h).

A stained layer appears in ERDC 79, as well. The depth is about the same as in ERDC 83. Fortunately, this level in ERDC 79 is an isochronal layer and is of little stratigraphic consequence. For this reason, I have not checked Sam's counts in this part of the core.

Another possible error on Sam's part is shown in Fig 4.18r. This figure shows the "measured" and "calibrated" number of chambers in the outline of Globoquadrina dutertrei. The difference between these two curves would seem to indicate that cross-talk holds measured values at about 5.35 chambers for depths less than 20 cm; calibration supposedly removes the cross-talk. However, this does not appear to be the

case. I counted the number of 5- and 6-chambered G. dutertrei's under a microscope and came up with an average of 5.3 chambers at 3.5 cm.

Why Sam made this particular error, if it is an error, is not clear. G. dutertrei has a progressively smaller abundance below 25 cm (Fig 4.18c); cross-talk from a relatively abundant species should become more and more important. Any error in the p_{ij} in the calibration matrix (Table 3.2) should also become more and more important. In this case, the p_{ij} are those in column 3 in Table 3.2, namely, the p_{3j} . The only significant sources of cross-talk are from species 0 (miscellaneous), 10 (Globigerinoides conglobatus), 12 (Globigerinella aequilateralis kummerform), and 20 (Candeina nitida); none of these is particularly abundant in ERDC 79.

It is not impossible that Sam is seeing something real: what I see as the number of chambers in the final whorl is not necessarily what it sees; there is sometimes half a chamber extra. Sam may be including this in its chamber count.

In any case, the way to resolve a problem such as this is to sit down with Sam and check its identifications as it makes them. This should be done with G. dutertrei before taking the chamber counts seriously. [Sam's counts of G. dutertrei itself appear to be acceptable, according to a spot check (Fig 4.18c) and to the original calibration (Table 3.4)].

4.2. Stratigraphy

We at last examine the stratigraphy of the ERDC cores. That

this turns out to be an anticlimax should by now come as no surprise. The local effects apparent in the ^{14}C data must likewise confuse stratigraphies; the lack of "ground truth" in the literature makes our conclusions unverifiable; and the sensitivity of the computations to observational error limits the scope of analysis. In what follows, we will consider first the stratigraphy of dissolution, then that of productivity, and finally that of foraminifera.

4.2.1. The stratigraphy of dissolution

Fig 4.7 summarizes the stratigraphy of dissolution. We will see that the period covered is the last 17 or so thousand years. The figure shows data from ERDC 128 but we will see that the same features appear in other cores.

The data in Fig 4.7 are coarse fraction percentages. As in Fig 4.5, such data may monitor fragmentation, which in turn may monitor dissolution (Berger, 1973).

Fig 4.7 suggests that dissolution was low at the very bottom of the core, high between, say, 40 and 30 cm, low between 30 and at least 15 cm, and high again after 12 cm. There are possibly two slumps, one at 26-28 cm and one at 12-15 cm.

If we assume that there was no dissolution (and no winnowing) between 30 and 12 cm, then eq (1.1) may suffice to remove the effects of mixing from the coarse fraction curve. The figure shows such a reconstruction (with $Z=5.5$ cm; see Section 3.1). The reconstruction suggests that dissolution decreased suddenly at the time when the sediment now at

30 cm was at the bottom of the mixed layer. The subsequent interval, until at least 15 cm, appears to have been more or less uneventful. The small peak in the reconstructed coarse fraction depends on a measurement precision which is probably not present.

The apparent slump at 26-28 cm may contribute to the sharpness of the change -- that is, the lower limit of the slump may be 30 cm. On the other hand, the apparent slumps may not be slumps at all but peaks in preservation. In such an interpretation, we would have to imagine a certain amount of dissolution continuing from 30 to 15 cm.

The decrease in coarse fraction beginning at about 12 cm appears to mark the onset of late Holocene dissolution. The onset appears sudden but removing the effects of mixing correctly requires knowledge of the rates of fragmentation, $K(z)$, and dissolution, $s_D(z)$. As yet, we do not have data sufficient to deduce these parameters. Thus, Fig 4.7 does not show a reconstruction in the late Holocene. The same applies to the beginning of "deglacial dissolution" at the bottom of the core. No reconstruction is shown but the change -- apparently starting at about 45 cm -- appears sudden too.

The stratigraphy of dissolution shown in Fig 4.7 appears in Thompson's (1976) data (Fig 4.5), in ERDC carbonate data (Fig 4.8), and in Sam's data (Figs 4.18m,n). Thompson's (1976) data shows at the top of V28-238 a sequence similar to that of ERDC 128: low dissolution, high dissolution, low dissolution, and the beginning of high dissolution.

Sam's fragment counts, Figs 4.18m,n, display the same sequence. Correlation of these counts with ERDC 128 coarse fraction (Fig 4.7)

provides the basic chronology. Before discussing this chronology, however, we must verify that the change in fragment abundance is due to a change in dissolution, not a change in the fragmentability of the faunal assemblage, which, as we will see below, happens to change at about the same time.

First, consider an example. Suppose that the fauna in a core consist of two species, P. obliquiloculata and G. aequilateralis. For argument's sake, take an instance where the corrosiveness of bottom waters remains constant but the faunal assemblage changes. Suppose at time t_1 fresh sediment contains 100% P. obliquiloculata; at a later time t_2 it contains 100% G. aequilateralis. What will the record of fragment abundance show?

Now, Table 3.5 in Chapter 3 indicates that the degree of fragmentation (in ERDC 79, 4-5 cm and 34-35 cm) of P. obliquiloculata is about 16%; that of G. aequilateralis is about 60%. We defined the degree of fragmentation there as the number of a species' fragments divided by the number of its whole shells. A reasonable guess, then, for the fragment abundance in the hypothetical core (neglecting mixing effects) is 13% at t_1 ($87\% \times 16\% = 13\%$) and 37% at t_2 ($63\% \times 60\% = 37\%$). The example would thus show a large change in fragments without any change in bottom water corrosiveness.

Table 4.4 follows this same procedure with six species from ERDC 83. (Table 3.5 shows that these species account for over 90% of the fragments in ERDC 79). The abundances in Table 4.4 are from Fig 4.18. The "deglacial" abundances are from levels slightly deeper than 31 cm in

ERDC 83. We use the degree of fragmentation from Table 3.5 as the fragmentability of each species. We thus assume that the fragmentability changes little with the amount of dissolution.

Species	fragment- ability (%)	Holocene abundance (%)	"Expected" Holocene fragments (%)	Deglacial abundance (%)	"Expected" deglacial fragments (%)
Pul	15.8	30	4.8	15	2.4
dut	8.4	2	.2	6	.5
aeq	59.7	14	8.4	15	9.0
sac	17.2	26	4.2	10	1.7
men	26.7	2	.5	5	1.4
tum	26.8	1	.3	2	.5
total			18.4		16.9

Table 4.4. Expected fragment change in ERDC 83 with no change in dissolution. The expected fragment abundance of a given species is the product of the abundance of whole shells of the species and its fragmentability. Fragmentabilities are the degrees of fragmentation shown in Table 3.5. See Table 3.1 for names corresponding to abbreviations.

We see from Table 4.4 that if dissolution had not changed in ERDC 83 between the "deglacial" time and the Holocene, we would have expected slightly more fragments in the Holocene. In fact, we find the reverse. This confirms that the fragment record in ERDC 83, at least, is a record of dissolution.

With this behind us, we can turn now to the chronology of the dissolution stratigraphy. The change in fragment abundance at 26 cm in

ERDC 79 is more or less simultaneous with the sudden increase in P. obliquiloculata (Fig 4.18a). Below we will date this latter event at about 9.5 kyr BP. To precisely date the fragment change, we must take into account changes in the coarse fraction and reconstruct the fragment signal according to eq (2.4). The fragment count is obviously too noisy for this (see Chapter 1).

The fragment count for ERDC 83 (4.18n; my count, not Sam's) is also more or less simultaneous with the change in P. obliquiloculata (Fig 4.18b). Since the accumulation rate in this core is 2-3 cm/kyr, we can argue that the dissolution decrease is within 1000 yrs of the P. obliquiloculata increase.

The grain size and carbonate analyses for ERDC 79 (Fig 4.17) also support the idea that dissolution decreased at about 26 cm. On the other hand, the relatively high coarse fraction at the bottom of ERDC 128 (Fig 4.7) does not appear in the ERDC 79 grain size analysis (Fig 4.17). However, there is a decrease in carbonate beginning at about 34 cm and an increase in fragments beginning at the same depth (Fig 4.18m). Fig 4.6 shows a reported age of 21 kyr BP for this depth. If the contemporaneous mixed layer age was about what it is today (4.4 kyr, according to Table 4.1), and if the change indeed came when the sediment now at 34 cm was at the bottom of the mixed layer, then the actual date of the change of dissolution would be about 16.6 kyr BP [$t = t_r - t_{ML}$; eq (2.7)]. Thus, if 34 cm in ERDC 79 correlates with, say, 45 cm in ERDC 128, then the period 16.6 kyr BP to 9.5 kyr BP is one of higher dissolution. Since this period roughly corresponds to the period when the ice sheets apparently melted (Fig 4.2), we will hereinafter refer to this

period as "deglacial times" and call the dissolution episode "deglacial dissolution."

The rate of dissolution during this episode was apparently lower than the late Holocene episode (see below). From the above dates and depths, we deduce an accumulation rate of about 1.7 cm/kyr for the deglacial period at ERDC 128. This takes into consideration the possible slump from 32-35 cm (Fig 4.7). The rate of supply of fresh sediment, S_0 , during this period may have been somewhat lower than that of the Holocene (see below). A value closer to 2 cm/kyr than 3 cm/kyr is likely.

Another source for dating the dissolution sequence is the ^{14}C date at 22.5 cm in ERDC 128 (Table 4.1). The reported age at this level is 12 kyr BP. In terms of the reconstructed coarse fraction discussed above (Fig 4.7, heavy dashed line), this level is actually about 8.6 kyr BP: The present mixed layer age is 4 kyr but this may be affected by dissolution (see Section 3, above). Shallower ERDC 123 today has a mixed layer age of about 3.4 kyr. This may be a better estimate of the mixed layer age when the sediment now at 22.5 cm in ERDC 128 was at the bottom of the mixed layer. Subtracting this 3.4 kyr from the reported age at 22.5 cm gives a date of 8.6 kyr BP.

To date the dissolution change at 30 cm in ERDC 128 we extrapolate downward from 22.5 cm. The problem is confounded by the apparent slump at 26-28 cm and by the uncertainty of the accumulation rate. If the slump encompasses 2 cm, there is 5.5 cm of steady accumulation to account for. According to Section 3.3, average Holocene rates of fresh

sedimentation, s_0 , on the equator (ERDC 128's latitude) are 2-3 cm/kyr. We will see below that s_0 may have been higher than average just after about 10 kyr BP. So 2 cm/kyr is certainly a minimum and 3 cm/kyr is not an unreasonable maximum. Now since dissolution at ERDC 128 was presumably low during the period in question, the accumulation rate, s , should be more or less equal to s_0 , barring winnowing and horizontal influx other than the slump. We therefore get an age of 10.4-11.4 kyr BP for the change in dissolution rate at 30 cm in ERDC 128. [Fig 4.7 shows a date of 10.6 kyr BP, which assumes $s=2.8$ kyr BP; this is more in line with s in ERDC 123 at the time (Fig 4.6)].

This date, 10.4-11.4 kyr BP, is 1-2 kyrs earlier than the change in *P. obliquiloculata* and fragments in ERDC 79. It may be that dissolution decreased at the deeper sites first. A more likely reason for the difference in dates is that the apparent slump at 26-28 cm in ERDC 128 is thicker than 2 cm.

The ^{14}C date at 22.5 cm in ERDC 128 also enables us to estimate the date when the late Holocene dissolution began. For this we assume that the interval 12-15 cm is a slump and that dissolution began after the slump. This gives us 7.5 cm of steady accumulation to account for. With $s=2-3$ cm/kyr, we get a date of 4.9 to 6.1 kyr BP for the onset of late Holocene dissolution. (Fig 4.7 shows 5 kyr BP with $s=2.1$ cm/kyr, which is more in line with s in ERDC 123 at about the same time; see Fig 4.6).

The bottom of ERDC 128's mixed layer being at 5.5 cm (Table 4.1), we find that during the late Holocene dissolution, $s=1.2$ cm/kyr.

The dissolution loss, s_D , is then about 1 cm/kyr, or about 50% of s_0 . This estimate is in agreement with that suggested by the carbonate data: Fig 4.12 indicates that the loss for the Holocene (0-22.5 cm) is 25%, or 5.6 cm of sediment; spread over 5 kyr, this is 1 cm/kyr.

The ^{14}C profile for ERDC 123 (Fig 4.6) suggests a later date for the beginning of late Holocene dissolution. The apparent accumulation rate shown by the profile, $\frac{dz}{dt_r}$, shows a sudden change at a reported age of 5 kyr BP. At this point, dissolution apparently sets in; the rate drops to about 1 cm/kyr. Subtracting a mixed layer age of 3.4 kyr (the present mixed layer age) from the reported age gives a date of 1.6 kyr BP for this change.

However, the carbonate curve for ERDC 123 (Fig 4.8a) shows a decrease beginning at 12 cm. This indicates that a second interpretation of the ERDC 123 ^{14}C profile is possible (Fig 4.19). In this interpretation, late Holocene dissolution makes the mixed layer older, starting at 12 cm. (As we discussed in Section 3.3.1 above, dissolution of young carbonate may cause this [$c_D > c$ in eq (2.8b)]). Fig 4.19 shows an extreme case. Here $s=1.6$ cm/kyr, $s_0=2.3$, and $c_D=c_0$: i.e., the dissolution rate is .7 cm/kyr and all the dissolving material is fresh. Other interpretations are possible by changing the depth where dissolution begins.

With the interpretation shown in Fig 4.19, the change in the age of the mixed layer is about 1000 yrs. At the beginning of dissolution, the mixed layer age would have been about 2.6 kyr. Since the reported age at 12 cm is 6.4 kyr BP (Fig 4.6), the actual date of the beginning

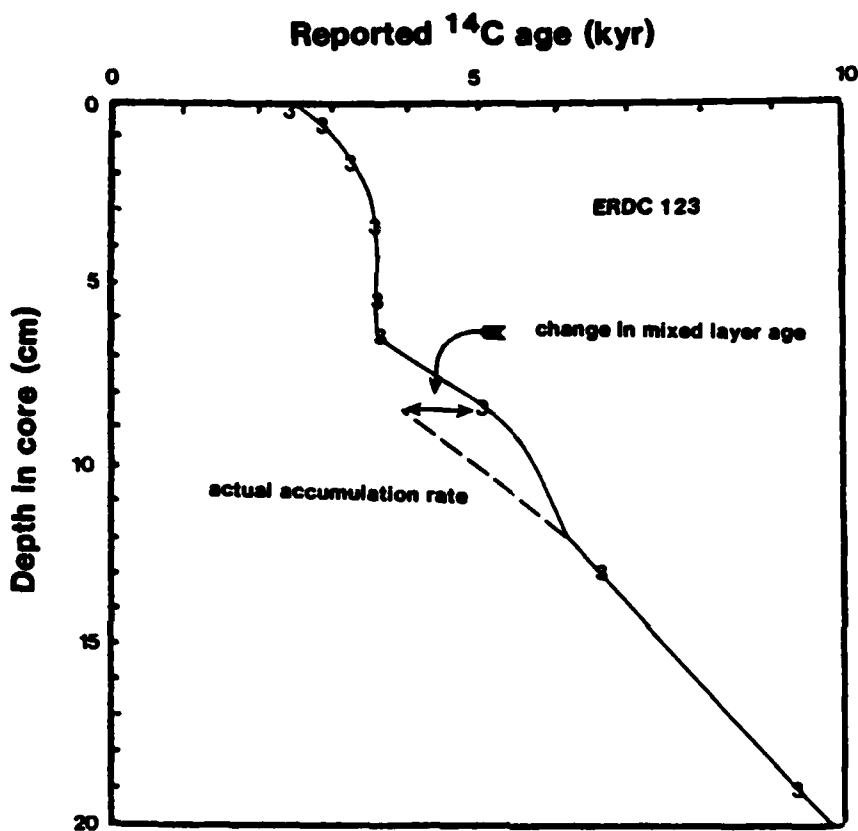


Fig. 4.19. Second interpretation of the near surface ^{14}C profile of ERDC 123. Points marked with a 3 are actual data points. Solid line is interpretation. Dashed line shows actual accumulation rate above 12 cm. In this interpretation, the difference between the actual accumulation rate and the reported profile is due to changing mixed layer age caused by dissolution beginning at the time when the sediment now at 12 cm was at the bottom of the mixed layer.

of dissolution at ERDC 123 may have been closer to 3.8 kyr BP.

This date is more compatible with the 5 kyr BP date at ERDC 128. However, the 2.6 kyr age for the mixed layer is probably too small. It

is the age given by eq (2.8c) with $Z=7$ cm, $n=n_0$, and $s_0=2.3$ cm/kyr. It does not include deep burrowing, which is likely to add, say, 500 yrs. In short, 3.8 kyr BP is on the early side.

In ERDC 79 and 83, late Holocene dissolution is visible as a slight increase in fragments (Figs 4.18m,n). This increase occurs in spite of a decrease in *G. aequilateralis* (Figs 4.18p,q), the main source of fragments (Table 4.4). Dating the beginning of late Holocene dissolution in these cores is not possible due to the weakness of the signal in ERDC 83 and due to the isochronal layers in ERDC 79.

In summary, the ERDC box cores show two episodes of carbonate dissolution, a deglacial episode and a late Holocene episode. The deglacial episode may have begun near 17 kyr BP and ended near 10 kyr BP. The late Holocene episode may have begun between 2 and 6 thousand years ago; it continues today. Most certain of these dates is the end of the deglacial episode. It is not certain to within 1000 yrs.

4.2.2. The stratigraphy of productivity

Changes in productivity — here considered equivalent to changes in the rate of supply of fresh sediment, s_0 , — are not as easily discerned as the changes in dissolution. The only more or less direct evidence available is that in Fig 4.6. ERDC 92 shows a distinct sequence of changes in accumulation rate: The rate goes from about 1 cm/kyr at the bottom of the core to about 2.8 cm/kyr from, say, 28 cm to 22 cm and then goes back to about 1.6 cm/kyr above 22 cm.

We will demonstrate shortly that these accumulation rates are

essentially rates of fresh sedimentation (i.e., that $s=s_0$). First, however, let us assume that this is true and attach dates to the changes.

The reported age of the change at 28 cm is about 14.5 kyr BP (Fig 4.6). The contemporaneous mixed layer was probably slightly older than today, since s_0 was smaller then. A value between 4.5 kyr and 5 kyr is likely. This gives a date of 9.5-10 kyr BP for the change at 28 cm.

However, as mentioned above, an isochronal layer may exist from 25 cm to 28 cm. This may confuse the exact date of the change in accumulation rate. In fact, it is not inconceivable that the relatively steep slope in the ^{14}C profile just above 25 cm is an adjustment of the contemporaneous mixed layer to horizontal influx that was younger than itself (Fig 4.14). But it is difficult to imagine a mechanism for creating young horizontal influx in this case.

If the change in accumulation rate at 22 cm in ERDC 92 is real, we can date it in the usual way: The reported age is 12 kyr BP; a contemporaneous mixed layer age of 3-4 kyr yields a date of 8-9 kyr BP. Thus, if real, the interval of high accumulation rate lasted no more than 2 kyr.

ERDC 92, recovered from the top of the plateau (Fig 4.1b), may have suffered winnowing (Berger et al., 1977b). If this is true, then the changes in accumulation rate shown in Fig 4.6 may be due to changes in winnowing.

To test this hypothesis, we can consider the core's carbonate

record (Fig 4.8a). In ERDC 92, carbonate ranges from 83 to 86%, except in the mixed layer, where the surface sample shows a value of 90%. This high value could be due to water sloshing in the corer during retrieval (see above) or, perhaps, to the presence of aragonite in the fine fraction.

Now, assuming that the rate of calcite dissolution is small at ERDC 92's depth (1598 m) and assuming that aragonite does not confuse the issue, eq (4.5) becomes

$$ns = n_o s_o - n_w s_w.$$

With $s_w = s_o - s$, we find that

$$s_o = \frac{n - n_w}{n_o - n_w} s. \quad (4.6)$$

Consider the 1 cm/kyr accumulation rate (s) at the bottom of ERDC 92. It is not impossible that at this level $n_o = 80\%$. (The other shallow cores suggest a decrease to this value during the deglacial period (Fig 4.8a) — due perhaps to an increased concentration of terrigenous minerals in surface waters). Taking $n_w = 60\%$ (a likely value) and taking $n = 86\%$ (the worst case), we see from eq (4.6) that for $s = 1$ cm/kyr, s_o could have been 1.3 cm/kyr; with $n_w = 75\%$ (an unlikely value), s_o could have been as high as 2.2 cm/kyr. Thus, even with an unlikely value for n_w , deglacial winnowing cannot bring s_o up to the early Holocene accumulation rate of 2.8 cm/kyr.

We have so far assumed that the supply and dissolution of aragonite do not cause the variations in accumulation in ERDC 92. Berger (1977) has found aragonite at various levels. Could it be that the

increase in accumulation rate at 10 kyr BP is due to decreased dissolution of aragonite? Apparently not. The carbonate curve (Fig 4.8a) shows a decrease, not an increase, in carbonate at this time. Likewise, the decrease in accumulation rate in the late Holocene of ERDC 92 cannot be due to dissolution of aragonite: the core shows an increase in carbonate at this time.

In short, the changes in accumulation rate in ERDC 92 appear to be changes in productivity (s_o).

The profiles of ^{14}C for ERDC 79 and 123 (Fig 4.6) do not have the resolution to verify these changes. For logical consistency, my interpretations of the profiles in Fig 4.6 include such changes. It is noteworthy, though, that ERDC 79 (without interpretation) shows a very low accumulation rate ($<.5$ cm/kyr) at 34 cm.

In summary, ^{14}C data from ERDC 92 suggest that productivity was low prior to about 10 kyr BP, high from about 8 to 10 kyr BP, and moderate from about 8 kyr BP to the present. ERDC 79 indicates that the low interval may extend at least through the entire deglacial interval.

4.2.3. The stratigraphy of planktonic foraminifera

We have seen so far that both dissolution and productivity changed sharply about 10,000 years ago. We will now see that the planktonic foraminiferal assemblage also changed sharply at about the same time. The change in flux of some species was large, that of others less so, or perhaps zero.

Our data is from ERDC 79 and 83 (Fig 4.18). To remove the

effects of mixing, we must take into account changes in carrier fraction (Chapter 2, Section 2). In the case of the abundances shown in Fig 4.18, the carrier fraction is the fraction between 355 and 840 μ . Fig 4.20 shows how this fraction changes in ERDC 79 and 83. The grain size measurements for ERDC 83 are actually of the fraction >420 μ . Probably 10-20% by weight of the material 355-840 μ is between 355 and 420 μ . This may account for some of the difference between the curves for ERDC 79 and 83. Also the ERDC 83 sediment was disaggregated by ultrasonication, which tends to reduce the larger sizes (Fig 4.15). On the other hand, there may be real differences between the two curves. For this reason, and for convenience, we will use the two curves as if prepared equivalently.

The most obvious changes in the foraminiferal abundances in Fig 4.18 are in those of P. obliquiloculata and G. menardii (Fig 4.18a,b). Isochronal layers obfuscate ERDC 79 but a reasonably undisturbed window occurs in this core between 20 and 28 cm (Fig 4.18a). This is fortunate because the major faunal change is at 26 cm. A small isochronal layer may exist from about 22-24 cm but we will not worry about this here.

Fig 4.21 shows a reconstruction a la Chapter 2, of the interval 20-28 cm in ERDC 79. The reconstruction uses eq (2.2) and (2.4) with a mixed layer thickness, Z , of 4 cm. As mentioned above, this choice of Z is based on the lack of homogeneity below 4 cm in the abundance of P. obliquiloculata. The reconstruction assumes no winnowing, dissolution, horizontal influx, or fragmentation. Shown also in Fig 4.21 is a time scale from Fig 4.6. I have subtracted mixed layer ages of 4-4.5 kyr from the reported ages. According to Fig 4.21, both P. obliquiloculata

AD-A089 064

SCRIPPS INSTITUTION OF OCEANOGRAPHY LA JOLLA CA

F/G 8/7

ONE-CENTIMETER STRATIGRAPHY IN FORAMINIFERAL OOZE: THEORY AND P--ETC(U)

AUG 80 R F JOHNSON

N00014-75-C-0152

SIO-REF-80-18

NL

UNCLASSIFIED

3 OF 3

AL 00014-75-C-0152



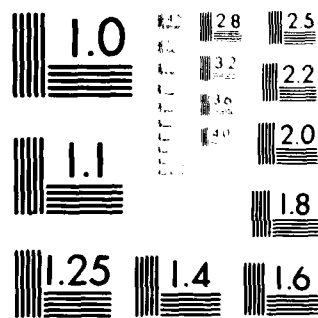
END

DATE

FILMED

10-80

DTIC



MICROCOPY RESOLUTION TEST CHART
NATIONAL BUREAU OF STANDARDS-1963-A

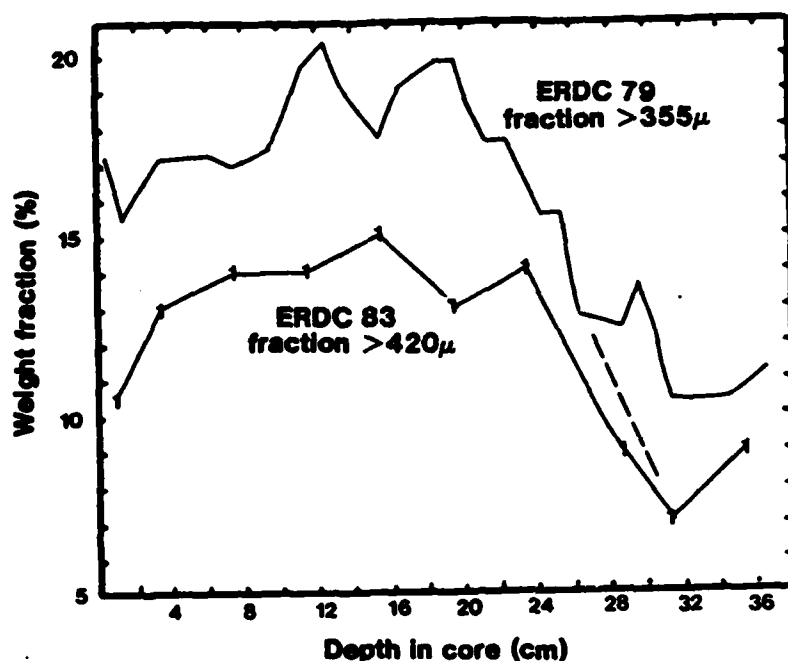


Fig 4.20. Variation of carrier fraction for species abundances in Fig 4.18. Dashed line is line of stratigraphic correlation.

and G. menardii changed simultaneously about 9500 yrs ago. The change in G. menardii took place in less than 1000 yrs. The change in P. obliquiloculata appears two-staged. This, however, may be a local effect; ERDC 83 does not exhibit such a change, as we will see shortly. Related to this local effect may be the small decrease in the mean diameter of P. obliquiloculata from 19–22 cm (Fig 4.18k). Perhaps the core site was in a slight depression during this period, so that the small round shells of P. obliquiloculata tended to collect there.

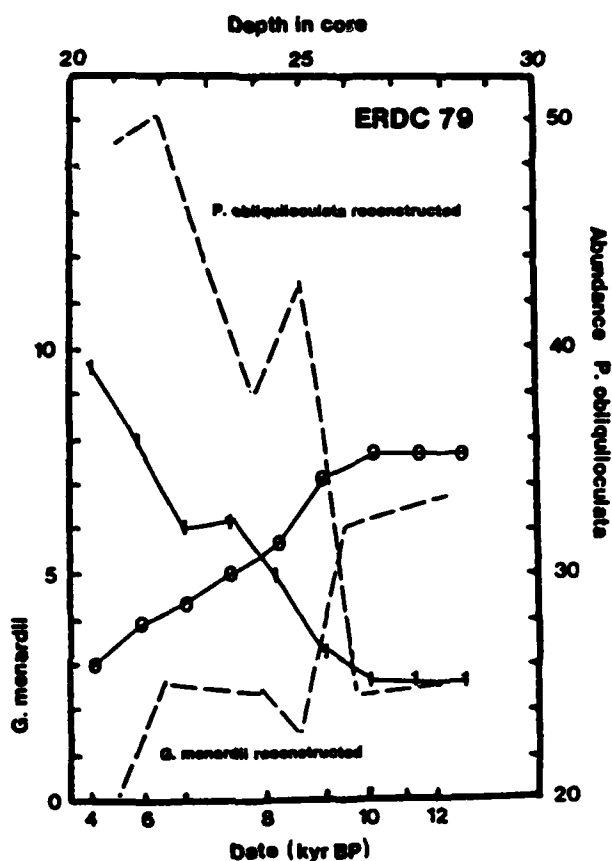


Fig 4.21. Reconstruction of the abundances of *P. obliquiloculata* and *G. menardii* in the interval 20-28 cm in ERDC 79. The reconstruction (dashed lines) uses data from Figs 4.18a and 4.20. Mixed layer thickness is taken as 4 cm. Digits 0 are observed values of *G. menardii* abundance; digits 1, observed values of *P. obliquiloculata* abundance.

Analogous to Fig 4.21 is Fig 4.22, which shows the same changes in ERDC 83. The Holocene accumulation rate of ERDC 83 is about 3 cm/kyr (Table 4.1). Details of changes should therefore be more visible. Even in this core, the change in *P. obliquiloculata* is very sharp, perhaps

occurring in 1 cm (about 400 yrs). The change in G. menardii appears more gradual. However, both reconstructions in this figure (as in Fig 4.21) depend strongly on the changes in carrier fraction. As Figs 4.15 and 4.17 show, measurements of this parameter have a great deal of noise. Furthermore, in the case of ERDC 83, the sample interval of the grain size analysis is 3-4 cm.

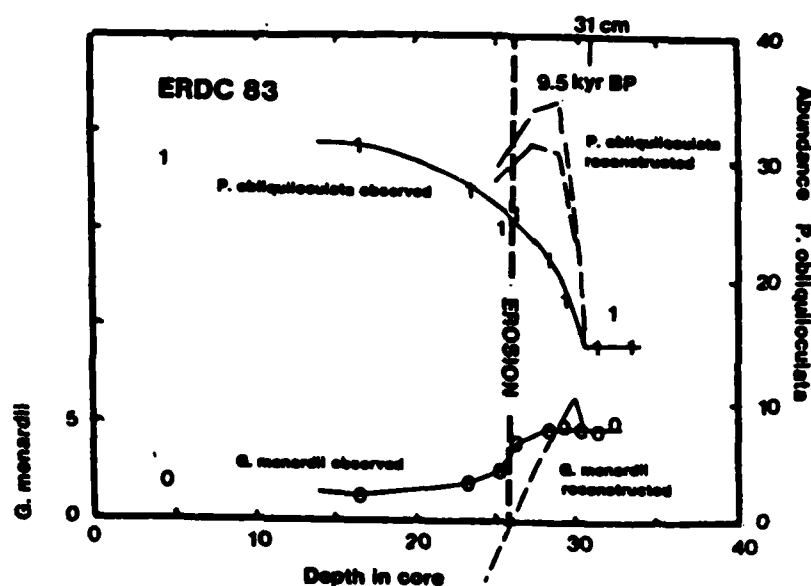


Fig 4.22. Like Fig 4.21, except for ERDC 83. The reconstruction of the P. obliquiloculata record uses two mixed layer thicknesses, 4.5 cm (the dashed line with the lower peak) and 7 cm.

The importance of changes in carrier fraction (Fig 4.20) is emphasized by the G. menardii reconstruction in Fig 4.22. Here the observed abundance appears to change not at all in the interval 29-31 cm; the reconstruction, though, which includes changes in carrier fraction, shows a brief increase, followed by a continuous decrease.

The magnitudes of the changes in grain size (Fig 4.20) and abundance of P. obliquiloculata (Figs 4.21 and 4.22) indicate that we must reconsider the conclusions we published earlier on the isotopic "meltwater spike" (Berger et al., 1977a). The carrier fraction relevant to this work is P. obliquiloculata >295 μ . The concentration (shells/cm³) of this carrier probably changed by a factor of 2-4 in the cores used. In our reconstructions of the "meltwater spike," we assumed that the concentration of P. obliquiloculata >295 μ remained constant. On reconsideration, therefore, it may be that the data show no "spike." However, deglacial isotopic changes are beyond the scope of this chapter (and report).

More relevant to this chapter is the apparent erosion in ERDC 83 at about 26 cm (Fig 4.22). The G. menardii change is so sharp at this level that the reconstruction goes negative. An unusually sharp change appears in the G. tumida data, as well (Fig 4.18d). The reconstruction of P. obliquiloculata likewise seems disturbed (Fig 4.22). G. sacculifer (Fig 4.18h) displays a sharp change at 24 cm, so the disturbed interval may extend over several cm.

The ¹⁴C data at 22.5 cm in ERDC 83 confirm the existence of erosion. The reconstructed age at 22.5 cm (t_{ML} =3.4 kyr; t_p =8.9 kyr BP, Table 4.1) is 5.2 kyr BP. ERDC 79 shows that the change in P. obliquiloculata occurs at 9.5 kyr BP. Therefore, in ERDC 83 only 8.5 cm accumulated between 5.2 kyr BP and 9.5 kyr BP (s =2 cm/kyr). With a more likely accumulation rate of, say, 2.8 cm/kyr, we would expect about 12 cm.

In spite of this disturbance in ERDC 83 and those in ERDC 79, it is clear that the major stratigraphical change in the cores came about 9,500 yrs ago. However, both ERDC 79 and ERDC 83 show changes at other times. Both suggest that G. sacculifer increased in abundance at a later time than P. obliquiloculata (Fig 4.18g,h). Due to the disturbances in the cores, however, the exact date is not obvious. 8 kyr BP is a guess. Of the two phenotypes of G. sacculifer, the one bearing a "sack" appears to have been the most reluctant to change at 9.5 kyr BP (Fig 4.18i,j).

Several species show changes prior to 9.5 kyr BP. Most obvious are G. conglomerata (Fig 4.18e) and G. tumida (Fig 4.18c). Together, they cause the "cold group" (G. tumida, G. conglomerata, G. dutertrei, and G. menardii) to peak at 35 cm in ERDC 79. As we saw earlier, reconstructed events at this level occurred at 16-17 kyr. Because of the noise in the data, we do not attempt a reconstruction of the G. tumida and G. conglomerata curves. In ERDC 83, G. tumida and G. menardii show early changes, too, but without more ^{14}C data and without a more detailed grain size analysis, it would be best not to draw any conclusions from this.

The stratigraphy of G. aequilateralis is peculiar (Figs 4.18o,p,q). The observed abundance reaches a peak just prior to 9.5 kyr BP. In ERDC 79 (Fig 4.18q), an increase comes after 35 cm but before 28 cm (i.e., 12-16 kyr BP according to Fig 4.6 with $t_{ML}=4.5$ kyr). The details of the change are lost in the disturbances between these levels. In ERDC 83, a reconstruction would show a sharp decrease of G. aequilateralis after 9.5 kyr BP.

If we consider the amount of fragmentation of G. aequilateralis (Table 4.4), it is apparent that G. aequilateralis is the dominant species during deglacial times, at least in the at ERDC 83's site. That this species particularly enjoys this period is supported by the low abundance of kummerform individuals (Fig 4.18q). (A kummerform individual has a penultimate chamber larger than ultimate. Berger (1971) has suggested that kummerformism is a sign of unhappiness). In ERDC 79, the ratio of normal form to kummerform abundances varies from 4 at 35 cm to 2.3 at the surface. It is interesting to note that meanwhile the kummerformity of the kummerforms -- the average ratio of the radii of the ultimate and penultimate chambers -- remains constant at 86%.

Shell diameters of some of the species exhibit a weak stratigraphy (Figs 4.18k,l). In this case, ERDC 79 and 83 do not agree particularly well. The mean diameter of P. obliquiloculata is smaller at the bottom of ERDC 83 by 30 μ but (ignoring the point at 33.5 cm) ERDC 79 shows a much smaller change, if any. In both core tops, the maximum diameter of G. sacculifer trilobus is smaller by 10-20 μ than that just prior to 9.5 kyr BP. The mean diameter of G. menardii varies considerably in ERDC 83 but much less in ERDC 79.

Bé et al. (1973) found the diameter of O. universa to be correlated with sea surface temperature. The relation is about 20 μ /°C. If this relation holds in the ERDC data, Fig 4.18s demonstrates no change in temperature at 9.5 kyr BP. However, the relation may not hold over Ontong-Java Plateau; the data of Bé et al. (1973) shows no significant correlation in waters >25°C. Also, for a mean diameter of 600 μ (the ERDC value, Fig 4.18s), the data of Bé et al. predict a temperature of

about 23°C even today, which is 6°C too cool.

Other measurements besides shell diameter also show a stratigraphy in the ERDC cores. The mean diameter of the penultimate chamber of G. sacculifer trilobus is an example (Fig 4.18s). This particular measurement correlates strongly with shell diameter, as you can see by comparing Fig 4.18s and Fig 4.18k. In general, however, the significance of these changes in chamber size and shell diameter are at present uncertain. Laboratory culture of the organisms may ultimately resolve this.

In the way of a summary, Table 4.5 provides a broad view of the faunal changes at Ontong-Java Plateau. The table compares the "fluxes" of five important species in the Holocene and deglacial. "Flux" here is the product of accumulation rate, s , carrier fraction, n , and observed abundance, c . The true flux of the species is this "flux" plus a flux lost to fragments. Units of the "flux" are mm of sediment per kyr.

We neglect mixing effects by choosing intervals where changes are small; here we choose a brief interval just prior to 9.5 kyr as the deglacial interval (26-28 cm in ERDC 79, 31-33 cm in ERDC 83) and the top two data points in ERDC 83 as the Holocene. The amount of disturbance in the upper part of ERDC 79 prevents us from finding a Holocene value in this core.

For convenience, we assume a constant sedimentation rate: 1 cm/kyr for ERDC 79 and 2.5 cm/kyr for ERDC 83. These numbers are probably not accurate in an absolute sense but are not unreasonable in a relative sense (Fig 4.10). We should keep in mind that the deglacial

sedimentation rates may have been considerably lower than the Holocene rates (see above).

For carrier fraction (fraction $>355\mu$), we use 12% for deglacial ERDC 79. For deglacial and Holocene ERDC 83, we use 9% and 16%, which includes a slight addition to that shown in Fig 4.20, for the fraction 355-420 μ .

Core	Species	Deglacial abundance (%)	Deglacial "flux" (mm/kyr)	Holocene abundance (%)	Holocene "flux" (mm/kyr)
ERDC 83	Pul	15	.34	31	1.24
	aeq	16	.36	14	.56
	men	5	.11	1.5	.06
	dut	6	.14	1.5	.06
	sac	10	.23	25	1.00
	tri	4	.09	7	.28
	sacsac	6	.14	18	.72
ERDC 79	Pul	25	.30		
	aeq	11	.13		
	men	7	.08		
	dut	6	.07		
	sac	10	.12		
	tri	5	.06		
	sacsac	5	.06		

Table 4.5. "Fluxes" of five important species in the fraction 355-840 μ . See Table 3.1 for abbreviations of species names.

Table 4.5 indicates that

- 1) in ERDC 83, the "flux" of P. obliquiloculata and G. sacculifer increased by a factor of 4 from deglacial to Holocene; if the deglacial sedimentation rate was lower than the Holocene, as ERDC 92 suggests, then this change in flux was larger;
- 2) the "flux" of G. sacculifer trilobus increased by a factor of 3 from deglacial to Holocene while that of G. sacculifer sacculifer increased by a factor of 5.
- 3) the "flux" of G. menardii and G. dutertrei decreased by a factor of 2 from deglacial to Holocene; if the deglacial sedimentation rate was lower, then this change in flux was smaller;
- 3) the deglacial "flux" of P. obliquiloculata at ERDC 83 was about the same as that at ERDC 79;
- 4) the deglacial "flux" of G. menardii and G. dutertrei at ERDC 83's site was greater than that at ERDC 79's; the same can be said of G. aequilateralis and G. sacculifer;

Fragmentation by dissolution acts to reduce the "flux" of G. aequilateralis and G. sacculifer. Thus, the actual deglacial flux of G. aequilateralis may be about the same as the Holocene flux. Likewise, the change in actual flux of G. sacculifer may be somewhat smaller than the change of "flux" shown in Table 4.5. Dissolution also reduces the "flux" of G. aequilateralis and G. sacculifer to ERDC 79.

W.H. Berger has suggested (in, e.g., Berger and Killingley, 1977) that G. dutertrei is an indicator of high productivity in surface waters. The evidence here is contradictory. The deglacial "flux" of

this species at ERDC 83 is certainly higher than that at ERDC 79. This is in agreement with ERDC 83 having higher productivity than ERDC 79 (e.g., Fig 4.10). [Keep in mind that since G. dutertrei does not fragment easily (Table 3.5) the "flux" for this species is close to the actual flux]. However, if a flux x of G. dutertrei corresponds to a productivity y , then Table 4.5 indicates that the Holocene productivity at ERDC 83 should be the same as the deglacial productivity at ERDC 79. This is very unlikely.

4.3. Conclusions from the stratigraphies

The objective of this chapter was to reconstruct a deep-sea record at 1-cm intervals consistent with published history. We have partly succeeded at this. The dramatic changes about 9500 yrs ago over Ontong-Java Plateau may be associated with the dramatic changes elsewhere. The changes we see in the rest of the record are more tentative.

To reiterate, the stratigraphies show this: From about 17 kyrs ago (the bottom of ERDC 79 and 128) to 9500 yrs ago -- through the interval we have called deglacial times -- dissolution at a given depth was moderate, sea surface productivity was low, and P. obliquiloculata and G. aequilateralis dominated the foraminifera. 9500 yrs ago, the flux of P. obliquiloculata as much as quadrupled in a period of as little as 300 yrs. From this point until about 8000 yrs ago, carbonate productivity was high and dissolution, low. At about 8 kyr BP, G. sacculifer increased its output but in general productivity decreased. Dissolution remained low. At a point some 2 to 6 thousand years ago, dissolution increased to its present high value.

What these changes mean in terms of climate is unknown. The low productivity during the deglacial period suggests that the doldrums (Fig 4.3) were at the equator more often than today. This is not unreasonable if we think of this period as an epoch analogous to November or April -- not the dead of winter (northeasterlies south of the equator) and certainly not late summer (southeasterlies north of the equator). The high productivity of the short period following 9.5 kyr BP suggests that this was a September epoch, with the doldrums relatively far north and the southeasterlies at the equator for a longer interval than today. The period subsequent to 8 kyr BP appears to have been more or less the same as today.

That it is P. obliquiloculata and G. sacculifer which respond most strongly to the climate changes is no doubt significant. P. obliquiloculata seems to be a species relatively insensitive to latitude (Table 4.5). The changes that affected it probably involved more than changes in upwelling. Perhaps this species reflects changes in the mean thickness and temperature of the sea surface mixed layer. On the other hand, if the doldrums spent more time on the equator in the western Pacific, then surface circulation may have been different. For instance, the south equatorial current may have contributed less volume flow to the area and a weakened undercurrent may have surfaced more often. Such changes in circulation may have been responsible for the changes in species fluxes. That the change at 9.5 kyr BP was primarily a temperature change is unlikely, since, prior to this time, "cooler" species such as Globorotalia truncatulinoides were not abundant. In particular, there is no evidence here for the 20°C surface temperatures

suggested by the New Guinea cirque data.

An exact interpretation of the stratigraphical changes must await a better understanding of the environmental responses of the species.

5. Summary of observations

We summarize here what we have observed in the ERDC box cores.

- 1) Where present, mixed layer thicknesses, Z , are 4-9 cm. A narrower range 4-7 cm is not unlikely; these values are less than we published earlier (Berger and Johnson, 1978). Out of the 18 box cores, 3 definitely do not show a mixed layer (ERDC 102, 129, 141). ^{14}C profiles (Fig 4.6) and carbonate curves (Fig 4.8) indicate that at least 8 of the other cores have a mixed layer (ERDC 79, 92, 123, 125, 128, 135, 136, 139).
- 2) ^{14}C profiles (Fig 4.6) suggest mixing rates as low as $5 \text{ cm}^2/\text{kyr}$ [Guinasso and Schink's (1975) $G=1$]. However, this estimate is based on changes in the ^{14}C distribution at the very core top. Observations of carbonate and grain size (Figs 4.8, 4.15, 4.17, 4.20) indicate that the 0-1 cm layer, at least, may be disturbed by core recovery or by processes not considered here.
- 3) Mixed layer ages are older than eq (2.8c) would lead us to expect. The deeper cores show this most obviously (Fig 4.10). In these cores, preferential dissolution of young sediment may be important but it cannot explain all the oldness. In the shallow cores, it is as yet impossible to say whether the

oldness is due to a small horizontal influx of carbonate without ^{14}C or a large influx of carbonate with the age of the ambient mixed layer (Table 4.2).

- 4) The Holocene rate of supply of fresh sediment, s_o , over Ontong-Java Plateau changes sharply with latitude. Cores poleward of about 2.5° show an s_o certainly less than 2 cm/kyr and perhaps as low as 1 cm/kyr or less. Cores equatorward of 1.5° may have rates as high as 3 cm/kyr. The supply of non-carbonates is correlated with the supply of carbonates. Since biogenous silica is a small part of the preserved sediment in the ERDC cores, this correlation suggests that the flux of terrigenous minerals is via fecal pellets.
- 5) The Holocene rate of dissolution seems to increase linearly with depth over Ontong-Java Plateau (Figs 4.11, 4.12). The linear increase begins at a depth between 2.5 and 3 km.
- 6) For most of the cores, including the shallowest, ERDC 92; winnowing, s_w , is not an important component of the accumulation rate (Table 4.3). This observation is tentative, awaiting a re-analysis of grain size.
- 7) Horizontal influx is an important component of the accumulation rates. In ERDC 79, for instance, influx from slumps or turbidity currents accounts for over half the accumulation in the core. This accumulation appears as isochronal layers. Several other cores show such layers. As already mentioned, steady horizontal influx may be partly responsible for the oldness of some

of the ERDC mixed layers. This steady influx may amount to up to half the accumulation (Table 4.2).

- 8) The stratigraphy of the box cores appear to exhibit at least two episodes of dissolution. One episode may have begun about 17 kyr BP and ended at 10 kyr BP. The other began 2-6 thousand years ago and continues today.
- 9) The productivity of the surface waters may have followed this sequence: low from before 16 kyr BP to 10 kyr BP; high from 10 kyr BP to 8 kyr BP; and moderate from 8 kyr BP to present.
- 10) The flux of several species of foraminifera changed sharply over Ontong-Java Plateau 9,500 yrs ago. One of the largest of these changes was in the flux in P. obliquiloculata. The change was sudden, taking perhaps no more than 300 yrs. There were changes in other species earlier and later than the change in P. obliquiloculata. A large change in the flux of G. sacculifer may have come at about 8 kyr BP. For this species, the "sack" bearing phenotype showed the most change, becoming relatively more abundant during the Holocene. G. aequilateralis especially thrived in the interval 17-10 kyr BP.
- 11) The ERDC box core stratigraphies show erosive events and slumps, suggesting, like the ^{14}C data, that local effects play an important role in the accumulation of ooze on Ontong-Java Plateau.

CHAPTER 5

CONCLUSIONS

In Chapter 4, we detected the change in Pulleniatina obliquiloculata at 10 kyr BP to within 1-cm in two cores (Figs 4.21, 4.22). That we were able to do this suggests that 1-cm stratigraphy in foraminiferal ooze is feasible and worthwhile. Dramatic changes in an abundant, dissolution resistant species present no difficulties to the theory described in Chapter 2 or the machinery developed in Chapter 3. Tracking and reconstructing such changes is an immediate application of the theory and machinery.

Changes of a more subtle sort offer more challenge. For instance, even though we were able to show that the change in P. obliquiloculata was large and sudden, we could not demonstrate that the change was a step-function. Effects local to ERDC 79 and 83 perturbed the observations at critical points. Furthermore, noise in the measurements of coarse fraction propagated significantly into the reconstructions.

Of these last two obstacles -- local effects and inaccurate grain size analysis -- local effects may turn out to be the major stumbling block to 1-cm stratigraphy. The only difficulty in improving grain size analysis is the fragility of some of the foraminiferal shells.

Eliminating local effects is more of a problem. The answer may lie in taking more cores. Replicate cores in slightly different topo-

graphic settings would be illuminating. Not only would this permit more precise stratigraphies but it would also teach us something about the scale and nature of the local processes.

In short, this research has solved a few of the problems; others face us.

REFERENCES

- Adelseck, C.G., Jr., and Berger, W.H., 1975. On the dissolution of planktonic foraminifera and associated microfossils during settling and on the seafloor. In: Sliter, W.V., Bè, A.W.H. and Berger, W.H. (Editors), *Dissolution of Deep-Sea Carbonates*, Cushman Foundation for Foraminiferal Research, Spec. Publ. 13, pp. 70-81.
- Aller, R.C. and Cochran, J.K., 1976. $^{234}\text{Th}/^{238}\text{U}$ disequilibrium in nearshore sediment: particle reworking and diagenetic time scales. *Earth and Planet. Sci. Lett.*, 29: 37-50.
- Arrhenius, G.O.S., 1952. Sediment cores from the east Pacific. *Swedish Deep-Sea Exped.*, 1947-1948, Repts, 5: 1-91
- Arrhenius, G.O.S., 1963. Pelagic sedimentation. In: Hill, M.N. (Editor), *The Sea*, vol. 3. John Wiley, NY, pp. 655-727.
- Barnett, T.P., 1978. The role of the oceans in the global climate system. In: Gribbin, J. (Editor), *Climate Change*, Cambridge Univ. Press, Cambridge, pp. 157-177.
- Bè, A.W.H., Harrison, S.M. and Lott, L., *Orbulina universa* d'Orbigny in the Indian Ocean. *Micropaleo.*, 19: 150-192.
- Berger, W.H., 1969. Planktonic foraminifera: basic morphology and ecological implications. *J. Paleontol.*, 43: 1369-1383.
- Berger, W.H., 1971. Planktonic foraminifera: sediment production in an oceanic front. *J. Foram. Res.*, 1: 95-118.
- Berger, W.H., 1973. Deep-sea carbonates: carbonate dissolution cycles. *J. Foram. Res.*, 3: 187-195.
- Berger, W.H., 1974. Deep-sea Sedimentation. In: Burk, C.A. and Drake, C.L. (Editors), *The Geology of Continental Margins*, Springer-Verlag, NY, pp. 213-241.
- Berger, W.H., 1975. Dissolution of deep-sea carbonates: an introduction. In: Sliter, W.V., Bè, A.W.H. and Berger, W.H. (Editors), *Dissolution of Deep-sea Carbonates*, Cushman Foundation for Foraminiferal Res., Spec. Pub. 13: 7-10.
- Berger, W.H., 1977. Deep-sea carbonates and the deglaciation preservation spike in pteropods and foraminifera. *Nature*, 269: 301-304.
- Berger, W.H., 1978. Deep-sea carbonate: pteropod distribution and the aragonitic compensation depth. *Deep-sea Res.*, 25: 447-452.
- Berger, W.H., 1978. Oxygen-18 stratigraphy in deep-sea sediments: additional evidence for the deglacial meltwater effect. *Deep-Sea Res.*

25: 473-480.

- Berger, W.H. and Heath, G.R., 1968. Vertical mixing in pelagic sediments. *J. Mar. Res.*, 26: 134-143.
- Berger, W.H., Johnson, R.F. and Killingley, J.S., 1977a. "Unmixing" of the deep-sea record and the deglacial meltwater spike. *Nature*, 269: 661-663.
- Berger, W.H., Johnson, T.C. and Hamilton, E.L., 1977b. Sedimentation on Ontong Java Plateau: Observations on a classic "carbonate monitor". In: Anderson, N.R. and Malahoff, A. (Editors), *The Fate of Fossil Fuel CO₂ in the Oceans*, Plenum, NY, pp. 543-567.
- Berger, W.H. and Killingley, J.S., 1977. Glacial-Holocene transition in deep-sea carbonates: selective dissolution and the stable isotope signal. *Science*, 197: 563-566.
- Berger, W.H. and Johnson, R.F., 1978. On the thickness and the ¹⁴C age of the mixed layer in deep-sea carbonates. *Earth and Planet. Sci. Lett.*, 41: 223-227.
- Berger, W.H., Killingley, J.S. and Vincent, E., 1978. Stable isotopes in deep-sea carbonates: box core ERDC 92, west equatorial Pacific. *Oceanologica Acta*, 1: 203-216.
- Berger, W.H., Ekdale, A.A. and Bryant, P.P., 1979. Selective preservation of burrows in deep-sea carbonates. *Mar. Geol.*, 32: 205-230.
- Berger, W.H., Johnson, R.F. and Killingley, J.S., in preparation. Box cores from the equatorial Pacific: ¹⁴C sedimentation rates and benthic mixing.
- Berner, R.A., 1978. Rate control of mineral dissolution under earth surface conditions. *Am. J. Sci.*, 178: 1235-1252.
- Bernstein, B.B., Hessler, R.R., Smith, R. and Jumars, P.A., 1978. Spatial dispersion of benthic foraminifera in the abyssal central North Pacific. *Limnol. Oceanog.*, 23: 401-416.
- Bloom, A.L., 1971. Glacial-eustatic and isostatic controls of sea-level since the last glaciation. In: Turekian, K.K. (Editor), *Late Cenozoic Glacial Ages*, Yale Univ. Press, New Haven, pp. 355-379.
- Bowler, J.M., Hope, G.S., Jennings, J.N., Singh, G. and Walker, D., 1976. Late Quaternary climate of Australia and New Guinea. *Quaternary Res.*, 6: 359-394.
- Bradshaw, J.S., 1959. Ecology of living planktonic foraminifera in the north and equatorial Pacific Ocean. *Cushman Foundation Foram. Res. Contr.*, 10: 25-64.
- Bramlette, M.N. and Bradley, W.H., 1941. *Geology and biology of North*

- Atlantic deep-sea cores between Newfoundland and Ireland, Part I, Lithology and geologic interpretations. USGS Prof. Paper 196: 1-34.
- Broecker, W.S., Turekian, K.K. and Heezen, B.C., 1958. The relation of deep-sea sedimentation rates to variations in climate. *Amer. J. Sci.*, 256: 503-517.
- Broecker, W.S. and Olson, E.A., 1959. Lamont radiocarbon measurements, VI. *Amer. J. Sci. Radiocarbon Suppl.*, 1: 111-132.
- Broecker, W.S., Ewing, M., and Heezen, B.C., 1960. Evidence for an abrupt change in climate close to 11,000 years ago. *Am. J. Sci.*, 258: 429-448.
- Chave, K.E., 1965. Carbonates: association with organic matter in surface seawater. *Science*, 148: 1723-1724.
- Clark, J.A., Farrell, W.E. and Peltier, W.R., 1978. Global changes in postglacial sea level: a numerical calculation. *Quaternary Res.*, 9:265-287.
- CLIMAP, 1976. The surface of the Ice Age Earth. *Science*, 191: 1131-1137.
- Cochran, J.K., 1979. The geochemistry of ^{226}Ra and ^{228}Ra in marine deposits. Ph.D. thesis, Yale Univ., 260 pp.
- Coul, B.C., Ellison, R.C., Fleeger, J.W., Higgins, R.P., Hope, W.D., Hummon, W.D., Reeger, R.M., Sterrer, W.E., Thiel, H., and Tietjen, J.H., 1977. Quantitative estimates of the meiofauna from the deep-sea off North Carolina. *Mar. Biol.*, 39: 233-240.
- Craig, H., 1965. The measurement of oxygen isotope paleotemperatures. In: Tongiorgi, E. (Editor), *Proc. Stable Isotopes in Oceanographic Studies and Paleotemperatures*, Spoleto, 2:1-87.
- Cushman, J.A. and Henbest, C.G., 1941. Geology and biology of North Atlantic deep-sea cores between Newfoundland and Ireland, Part II, Foraminifera: 35-55.
- Dansgaard, W., Johnsen, S.J., Clausen, H.B., and Langway, C.C., Jr., 1971. Climatic record revealed by the Camp Century ice core. In: Turekian, K.K. (Editor), *Late Cenozoic Glacial Ages*, Yale Univ. Press, New Haven, pp. 37-56.
- Dansgaard, W. and Tauber, H., 1969. Glacier ^{18}O content and Pleistocene ocean temperatures. *Science*, 166: 499-502.
- Davies, T.A. and Gorsline, D.S., 1976. Oceanic sediments and sedimentary processes. In: Riley, J.P. and Chester, R. (Editors), *Chemical Oceanography*, v. 2, 2nd ed., Academic Press, London, pp. 1-80.
- DeMaster, D.J., 1979. The marine budgets of silica and ^{32}Si . Ph.D.

- thesis, Yale Univ., 307 pp.
- Dunbar, R.B. and Berger, W.H., 1979. Fecal pellet flux in Santa Barbara Basin (California) based on sediment trapping. GSA Annual Meeting, Program with Abstracts.
- Duplessy, J.-C., 1978. Isotope studies. In: Gribbin, J. (Editor), Climatic Change, Cambridge Univ. Press, Cambridge, pp. 46-67.
- Emery, K.O., 1969. The continental shelves. Scientific Amer., 221: 106-122.
- Emiliani, C., 1955. Pleistocene temperatures. J. Geol., 63: 538-578.
- Emiliani, C., Gartner, S., Lidz, B., Eldridge, K., Elvey, E.K., Huang, T.C., Stipp, J.J., and Swanson, M.F., 1975. Paleoclimatological analysis of late Quaternary cores from the northeastern Gulf of Mexico. Science, 189: 1083-1088.
- Emiliani, C., Rooth, C. and Stipp, J.J., 1978. The late Wisconsin flood into the Gulf of Mexico. Earth and Planet. Sci. Ltrrs., 41: 159-162.
- Faure, G., 1977. Principles of Isotope Geology, John Wiley, NY, 464 pp.
- Gardner, J.V. and Hays, J.D., 1976. Response of sea-surface temperature and circulation to global climatic changes during the past 200,000 years in the eastern equatorial Atlantic. Geol. Soc. Amer. Mem. 145: 221-246.
- Gates, W.L., 1976. Modeling the Ice-Age climate. Science, 191: 1138-1141.
- Gates, W.L., 1976. The numerical simulation of Ice Age climate with a global general circulation model. J. Atmos. Sci., 33: 1844-1873.
- Geitznauer, K.R., Roche, M.B. and McIntyre, A., 1976. Modern Pacific coccolith assemblages: derivation and application to late Pleistocene paleotemperature analysis. Geol. Soc. Amer. Mem. 145: 423-448.
- Goldberg, E.D. and Koide, M., 1962. Geochronological studies of deep-sea sediments by the thorium-ionium method. Geochim. Cosmochim. Acta, 26: 417-450.
- Guinasso, N.L., Jr., and Schink, D.R., 1975. Quantitative estimates of biological mixing rates in abyssal sediments, J. Geophys. Res., 80: 3032-3043.
- Haltiner, G.J. and Martin, F.L., 1957. Dynamical and Physical Meteorology, McGraw-Hill, New York, 470 pp.
- Heath, G.R. and Culberson, C., 1970. Calcite: degree of saturation, rate of dissolution, and the compensation depth in the deep oceans.

- Geol. Soc. Amer. Bull., 81: 3157-3160.
- Hecht, A.D. and Savin, S.M., 1972. Phenotypic variation and oxygen isotope ratios in Recent planktonic foraminifera. *J. Foram. Res.*, 2: 55-67.
- Hessler, R.R. and Jumars, P.A., 1974. Abyssal community analysis from replicate box cores in the central North Pacific. *Deep-Sea Res.*, 21: 185-209.
- Honjo, S., 1975. Dissolution of suspended coccoliths in the deep-sea water column and sedimentation of coccolith ooze. In: Sliter, W.V., Bè, A.W.H. and Berger, W.H. (Editors), *Dissolution of Deep-sea Carbonate*, Cushman Foundation for Foraminiferal Res., Sp. Pub. 13: 114-128.
- Johnson, J.W., Guinasso, N.L., Jr., and Schink, D.R., 1978. Biological mixing rates in the Atlantic abyssal sediments using plutonium as a tracer (abs.). 41st Ann. Meeting, ASLO, June 1978.
- Johnson, T.C., Hamilton, E.L. and Berger, W.H., 1977. Physical properties of calcareous ooze: control by dissolution at depth. *Mar. Geol.*, 24: 259-277.
- Jumars, P.A., 1978. Spatial autocorrelation with RUM (Remote Underwater Manipulator): vertical and horizontal structure of a bathal benthic community. *Deep-Sea Res.*, 25: 589-604.
- Keir, R.S., 1980. The dissolution kinetics of biogenic calcium carbonates in seawater. *Geochim. Cosmochim. Acta*, 44: 241-252.
- Kendall, T.R., 1970. The Pacific Equatorial Countercurrent. Ph.D. Thesis, Nova University. 19 pp + figs.
- Kennett, J.P., 1976. Phenotypic variation in some recent late Cenozoic planktonic foraminifera. In: Hedley, R.H. and Adam, C.G. (Editors), *Foraminifera*, vol. 2, Academic Press, NY, pp. 112-170.
- Kennett, J.P. and Shackleton, N.J., 1975. Laurentide ice sheet meltwater recorded in Gulf of Mexico deep-sea cores. *Science*, 188: 147-150.
- Kershaw, A.P., 1975. Late Quaternary vegetation and climate in north-eastern Australia. *Nature*, 251: 222-223.
- Krishnamurthy, R.V., Lal, D., Somayajulu, B.L.K., and Berger, W.H., 1979. Radiometric studies of box cores from the Ontong-Java Plateau. *Proc. Indian Acad. Sci.*, 88A, pt II: 273-283.
- Laughton, A.S., 1963. Microtopography. In: Hill, M.N. (Editor), *The Sea*, vol. 3. John Wiley, NY, pp. 437-472.
- Lisitzin, A.P., 1970. Sedimentation and geochemical considerations. In: Wooster, W.S. (Editor), *Scientific Exploration of the South*

- Pacific, National Academy of Science, Washington, DC, pp. 89-132.
- Löffler, E., 1972. Pleistocene glaciation in Papua and New Guinea. *Zeitschrift für Geomorphologie, Suppl.*, 13: 32-58.
- Luz, B. and Shackleton, N.J., 1975. CaCO_3 solution in the tropical east Pacific during the past 130,000 years. In: Sliter, W.V., Bè, A.W.H. and Berger, W.H. (Editors), *Dissolution of Deep-sea Carbonates*, Cushman Found. for Foraminiferal Res., sp. publ. 13, pp. 142-150.
- McCave, I.N. and Swift, S.A., 1976. A physical model for the rate of deposition of fine grained sediments in the deep sea. *Geol. Soc. Amer. Bull.*, 87: 541-546.
- McGowan, J.A., 1974. The nature of oceanic ecosystems. In: Miller, C. (Editor), *The Biology of the Oceanic Pacific*, Oregon State Univ. Press, Corvallis, pp. 9-28.
- Manabe, S. and Hahn, D.G., 1977. Simulation of the tropical climate of an Ice Age. *J. Geophys. Res.*, 82: 3889-3911.
- Mikkelsen, N., 1978. Preservation of diatoms in glacial to Holocene deep-sea sediments of the equatorial Pacific. *Geol.*, 6: 553-555.
- Molinari, R.L., Festa, J.F. and Behringer, D.W., 1978. The circulation of the Gulf of Mexico derived from estimated dynamic height fields. *J. Phys. Oceanog.*, 8: 987-997.
- Moore, T.C., Jr., Heath, G.R. and Kowsmann, R.O., 1973. Biogenic sediments of the Panama Basin. *J. Geol.*, 81: 458-472.
- Moore, T.C., Jr., Pisias, N.G. and Heath, G.R., 1977. Climate changes and lags in Pacific carbonate preservation, sea surface temperature and global ice volume. In: Anderson, N.R. and Malahoff, A. (Editors), *Fate of Fossil Fuel CO_2 in the Ocean*, Plenum, NY, pp. 145-165.
- Nozaki, Y., Cochran, J.K., Turekian, K.K. and Kellar, G., 1977. Radiocarbon and ^{210}Pb distribution in submersible-taken deep-sea cores from Project Famous. *Earth and Planet. Sci. Lett.*, 34: 167-184.
- Parker, F.L., 1962. Planktonic foraminiferal species in Pacific sediments. *Micropaleontol.*, 8: 219-254.
- Parker, F.L. and Berger, W.H., 1971. Faunal and solution patterns of planktonic foraminifera in surface sediments of the South Pacific. *Deep-Sea Res.*, 18: 73-107.
- Paul, A.Z., 1977. The effect of benthic biological processes on CO_2 carbonate system. In: Anderson, N.R. and Malahoff, A. (Editors), *Fate of Fossil Fuel CO_2 in the Ocean*, Plenum, NY, pp. 345-354.

- Peng, T.-H., Broecker, W.S., Kipphut, G., and Shackleton, N., 1977. Benthic mixing in deep sea cores as determined by ^{14}C dating and its implications regarding climate stratigraphy and the fate of fossil fuel CO_2 . In: Anderson, N.R. and Malahoff, A. (Editors), Fate of Fossil Fuel CO_2 in the Ocean, Plenum, NY, pp. 355-373.
- Peng, T.-H., Broecker, W.S. and Berger, W.H., 1979. Rates of benthic mixing in deep-sea sediment as determined by radioactive tracers. Quaternary Res., 11: 141-149.
- Petersen, M.N.A., 1966. Calcite: rates of dissolution in a vertical profile in the central Pacific. Science, 154: 1542-1544.
- Philander, S.G.H., 1973. Equatorial undercurrent: measurements and theories. Revs. Geophys. Space Phys., 11: 513-570.
- Phleger, F.B., 1942. Foraminifera of submarine cores from the continental slope. Geol. Soc. Amer. Bull., 53: 1073-1097.
- Porter, S.C., 1979. Hawaiian glacial ages. Quaternary Res., 12: 161-187.
- Quinn, W.H., 1971. Late Quaternary meteorological and oceanographic developments in the equatorial Pacific. Nature, 229: 330-331.
- Ralph, E.K. and Michael, H.N., 1974. Twenty-five years of radiocarbon dating. Amer. Scient., 62: 553-560.
- Rhoads, D.C., 1974. Organism-sediment relations on the muddy sea floor. In: Barnes, H. (Editor), Oceanog. and Mar. Biol., Ann. Rev., 12: 263-300.
- Riehl, H., 1954. Tropical Meteorology. McGraw-Hill, NY, 392 pp.
- Reid, J.L. and Arthur, R.S., 1975. Interpretation of maps of geopotential anomaly for the deep Pacific Ocean. J. Mar. Res., 33 (suppl.): 37-52.
- Robinson, M.K., 1976. Atlas of North Pacific Ocean Monthly Mean Temperatures and Mean Salinities of the Surface Layer, US Naval Oceanographic Office, Washington, DC.
- Rotschi, H., Hisard, Ph. and Jarrige, F., 1972. Les eaux du Pacifique occidental a 170°E entre 20°S and 5°N . O.R.S.T.O.M., Noumea, 113p.
- Rubin, M. and Suess, H.E., 1955. U.S. Geol. Surv. Radiocarbon dates, II. Science, 121: 481-488.
- Ruddiman, W.F., Dicus, R.L. and Glover, L.K., 1976. Elimination of bioturbation effects in deep-sea sediment cores by deconvolution processing (abs.). Geol. Soc. Amer., Ann. Meeting, Abstracts with Programs: 1079-1080.
- Sadler, J.C. and Harris, B.E., 1970. The mean tropospheric circulation

- and cloudiness over southeast Asia and neighboring areas. *Hawaii Inst. Geophys.*, HIG-70-26, 37 pp.
- Saidova, Kh.M., 1971. Distribution of foraminifera along the Pacific coast of South America. *Oceanology*, 11: 210-217.
- Sarnthein, M., 1978. Sand deserts during glacial maximum and climatic optimum. *Nature*, 272: 43-46.
- Savin, S.M. and Douglas, R.G., 1973. Stable isotopes and magnesium geochemistry of recent planktonic foraminifera from the South Pacific. *Geol. Soc. Amer. Bull.*, 84: 2327-2342.
- Savin, S.M. and Stehli, F.G., 1974. Interpretation of oxygen isotope paleotemperature measurements: effect of the $^{18}\text{O}/^{16}\text{O}$ ratio of sea water, depth stratification of foraminifera, and selective dissolution. *Centre Nat. Recherche Sc. Colloques Internat.*, 219: 183-191.
- Schink, D.R. and Guinasso, N.L., Jr., 1977a. Effects of bioturbation on sediment-seawater interaction. *Mar. Geol.*, 23: 133-154.
- Schink, D.R. and Guinasso, N.L., Jr., 1977b. Modelling the influence of bioturbation and other processes on calcium carbonate dissolution at the seafloor. In: Anderson, N.R. and Malahoff, A. (Editors), *Fate of Fossil Fuel CO_2 in the Ocean*, Plenum, NY, pp. 375-399.
- Schott, W., 1935. Die Foraminiferen in dem aquatorialen Teil des Atlantischen Ozeans: *Deut. Atlantischen Exped. Meteor 1925-1927*, 3: 43-134.
- Shackleton, N.J. and Opdyke, N.D., 1973. Oxygen isotope and paleomagnetic stratigraphy of equatorial Pacific cores V28-238: oxygen isotope temperatures and ice volumes on a 10^5 year and 10^6 year scale. *Quaternary Res.*, 3: 39-55.
- Shackleton, N.J. and Opdyke, N.D., 1976. Oxygen-isotope and paleomagnetic stratigraphy of Pacific core V28-239, late Pliocene to latest Pleistocene, *Geol. Soc. Amer. Mem.*, 145: 449-464.
- Smith, S., Albright, U., Psaroupoulos, G. and Lingley, R., 1975. Eurydice Expedition, leg 9, R/V Thomas Washington, Informal report and index of navigation, depth, magnetic and subbottom profiler data. SIO Geological Data Center, Scripps Institution of Oceanography.
- Street, F.A. and Grove, A.T., 1979. Global maps of lake-level fluctuations since 30,000 yr B.P. *Quaternary Res.*, 12: 83-118.
- Stuiver, M., 1971. Evidence for the variation of atmospheric ^{14}C content in the late Quaternary. In: Turekian, K.K. (Editor), *Late Cenozoic Glacial Ages*, Yale Univ. Press, New Haven, pp. 57-70.
- Stuiver, M., 1978. Radiocarbon timescale tested against magnetic and other dating methods. *Nature*, 273: 271-274.

- Sundquist, E., Richardson, D.K., Broecker, W.S., and Peng, T.-H., 1977. Sediment mixing and carbonate dissolution in the southeast Pacific Ocean. In: Anderson, N.R. and Malahoff, A. (Editors), *Fate of Fossil Fuel CO₂ in the Ocean*, Plenum, NY, pp. 429-454.
- Suess, E., 1970. Interaction of organic compounds with calcium carbonate. *Geochim. Cosmochim. Acta*, 34: 157-168.
- Sverdrup, H.U., 1947. Wind-driven currents in a baroclinic ocean; with application to the equatorial currents of the eastern Pacific. *Proc. Nat. Acad. Sci.*, 33: 318-326.
- Sverdrup, H.U., Johnson, M.W. and Fleming, R.H., 1942. *The Oceans, Their Physics, Chemistry, and General Biology*, Prentice-Hall, Englewood Cliffs, NJ, 1087pp.
- Thiel, H., 1975. The size structure of the deep-sea benthos. *Int. Revue ges. Hydrobiol.*, 60: 575-606.
- Thompson, D'A.W., 1917. *On Growth and Form*, Cambridge Univ. Press, Cambridge, 793 pp.
- Thompson, P.R., 1976. Planktonic foraminiferal dissolution and the progress towards a Pleistocene equatorial Pacific transfer function. *J. Foram. Res.*, 6: 208-227.
- Turekian, K.K., Cochran, J.K. and DeMaster, D.J., 1978. Bioturbation in deep-sea deposits: rates and consequences. *Oceanus*, 21: 34-41.
- U.S. Navy, 1977. *Marine Climatic Atlas of the World (NAVAIR 50-1C-529)*, v. 2, US Gov't Printing Office, Washington, DC, 388 pp.
- van Andel, Tj.H., 1973. Texture and dispersal of sediments in the Panama Basin. *J. Geol.*, 81: 434-457.
- Volat, J.-L., Pastouret, L. and Vergnaud-Grazzini, C., 1980. Dissolution and carbonate fluctuations in Pleistocene deep-sea cores: a review. *Mar. Geol.*, 34: 1-28.
- Webster, P.J. and Streten, N.A., 1978. Late Quaternary Ice Age climates of tropical Australasia: interpretations and reconstructions. *Quaternary Res.*, 10: 279-309.
- Williams, J., 1978. The use of numerical models in studying climatic change. In: Gribbin, J. (Editor), *Climatic Change*, Cambridge Univ. Press, Cambridge, pp. 178-190.
- Williams, J., Barry, R.G. and Washington W.M., 1974. Simulation of atmospheric circulation using the NCAR global circulation model with Ice Age boundary conditions. *J. Appl. Meteorol.*, 13: 305-317.
- Williams, P.M., Stenhouse, M.C., Druffel, E.M. and Koide, M., 1978. Organic ¹⁴C activity in an abyssal marine sediment. *Nature*, 276:

698-701.

Wyrtki, K., 1975. El Nino -- The dynamic response of the equatorial Pacific Ocean to atmospheric forcing. J. Phys. Oceanog., 5: 572-584.

Wyrtki, K. and Meyers, G., 1975. The trade wind field over the Pacific Ocean, Part 1. The mean field and the mean annual variation. HIG-75-1, Hawaii Institute of Geophysics, Univ. of Hawaii, 25pp.+figs.

APPENDIX 1

EXAMPLES OF OUTPUT FROM THE ANALYSIS PROGRAM

This appendix shows typical analysis for each species (except Globigerina calida) which Sam currently recognizes.

The upper half of the output describes the top view of the given specimen; the lower half describes the side view. Drawings are of the specimen's outline and of circles fitted to its chambers. Dimensions shown are in pixels (1 pixel = 2.675 μ here) and are abbreviated as:

DMAX = maximum diameter
DMIN = minimum diameter
DBAR = mean diameter
DX90 = diameter at 90° to maximum diameter
DN90 = diameter at 90° to minimum diameter
HEIGHT = maximum TV y value minus minimum TV y value
 = shell height when viewed from the side
H/W = height (side view) divided by DMIN (top view)
W/L = DMIN (top view) divided by DMAX (top view)
H/L = height (side view) divided by DMAX (top view).

In addition,

N = number of positive peaks in high-pass version of outline
L = number of chambers
SMIN = minimum value of high-pass version of outline (in pixels)
SCOUNT = count of troughs in high-pass version of outline which
 fall below -10 pixels

The high-pass version of each outline appears slightly to the right in each figure. The upper horizontal line represents the zero level, the level in which the difference between the smoothed version of the the outline and the outline itself is zero. The lower horizontal line has a value of -10 pixels. Smoothing window for these analyses is 1/10 of the circumference of each outline.

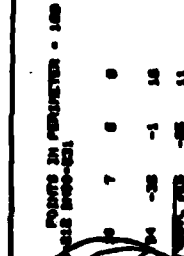
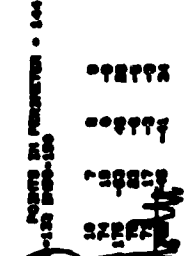

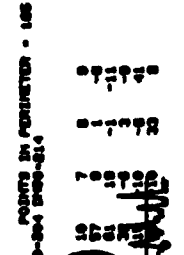
The table superimposed on each outline describes the chambers of

that outline. Each row corresponds to an arc between two sutures. If the arc meets certain qualifications, the program considers the arc part of a separate chamber and completely fills the table row. Chamber 1 follows clockwise from the first suture which is clockwise of the leftmost point in the outline.

Each column in the table of chamber descriptions is labelled with a number. These numbers are the code used by the identification program and represent the following:

- 1 = angle in degrees subtended by lines drawn from chamber center to chamber sutures
- 2 = chamber radius in pixels
- 3 = suture depth in pixels; i.e., peak height of high-pass version at suture point
- 4 = an index of suture depth divided by suture width
- 14 = chamber diameter divided by mean shell diameter (%)
- 12 = chordlength between sutures
- 11 = angle in degrees subtended by lines from shell center of gravity to chamber centers
- 10 = range of error in circle fit; error (in parts per thousand of chamber radius) is chamber radius minus distance from outline to chamber center; thus, positive error occurs when circle is outside of outline; range is maximum minus minimum error
- 7,8,9 = mean error in 1st, 2nd, and 3rd thirds of chamber (ordered clockwise)

Fig A1.1. Sample output from Sam for "species" 1-4. See text for explanation of format.

<p>FILE 010100 SHELL 0 20 COUNTS IN PERIMETER - 100 SPEC-213 SPEC-187 HEIGHT-180 SPEC-180 SPEC-180 SPEC-180-1 00 SPEC-180-1 00</p>  <p>IN 0 L-0 SPEC-180-1 00 SPEC-180-1 00 SPEC-180-1 00 SPEC-180-1 00 SPEC-180-1 00 SPEC-180-1 00 SPEC-180-1 00</p> <p>IN 0 L-0 SPEC-180-1 00 SPEC-180-1 00 SPEC-180-1 00 SPEC-180-1 00 SPEC-180-1 00 SPEC-180-1 00 SPEC-180-1 00</p> <p>1 Cyclic universe</p>	<p>FILE 010100 SHELL 0 20 COUNTS IN PERIMETER - 100 SPEC-213 SPEC-187 HEIGHT-180 SPEC-180 SPEC-180 SPEC-180-1 00 SPEC-180-1 00</p>  <p>IN 0 L-0 SPEC-180-1 00 SPEC-180-1 00 SPEC-180-1 00 SPEC-180-1 00 SPEC-180-1 00 SPEC-180-1 00 SPEC-180-1 00</p> <p>IN 0 L-0 SPEC-180-1 00 SPEC-180-1 00 SPEC-180-1 00 SPEC-180-1 00 SPEC-180-1 00 SPEC-180-1 00 SPEC-180-1 00</p> <p>2 Polychromatic colorless</p>
<p>FILE 010100 SHELL 0 20 COUNTS IN PERIMETER - 100 SPEC-213 SPEC-187 HEIGHT-180 SPEC-180 SPEC-180 SPEC-180-1 00 SPEC-180-1 00</p>  <p>IN 0 L-0 SPEC-180-1 00 SPEC-180-1 00 SPEC-180-1 00 SPEC-180-1 00 SPEC-180-1 00 SPEC-180-1 00 SPEC-180-1 00</p> <p>IN 0 L-0 SPEC-180-1 00 SPEC-180-1 00 SPEC-180-1 00 SPEC-180-1 00 SPEC-180-1 00 SPEC-180-1 00 SPEC-180-1 00</p> <p>3 Cyclic universe</p>	<p>FILE 010100 SHELL 0 20 COUNTS IN PERIMETER - 100 SPEC-213 SPEC-187 HEIGHT-180 SPEC-180 SPEC-180 SPEC-180-1 00 SPEC-180-1 00</p>  <p>IN 0 L-0 SPEC-180-1 00 SPEC-180-1 00 SPEC-180-1 00 SPEC-180-1 00 SPEC-180-1 00 SPEC-180-1 00 SPEC-180-1 00</p> <p>IN 0 L-0 SPEC-180-1 00 SPEC-180-1 00 SPEC-180-1 00 SPEC-180-1 00 SPEC-180-1 00 SPEC-180-1 00 SPEC-180-1 00</p> <p>4 Cyclic universe colorless</p>

THIS PAGE IS BEST QUALITY PRINT
 FROM COPY OF 100-100-100

Fig A1.2. Sample output from Sam for "species" 5-8.

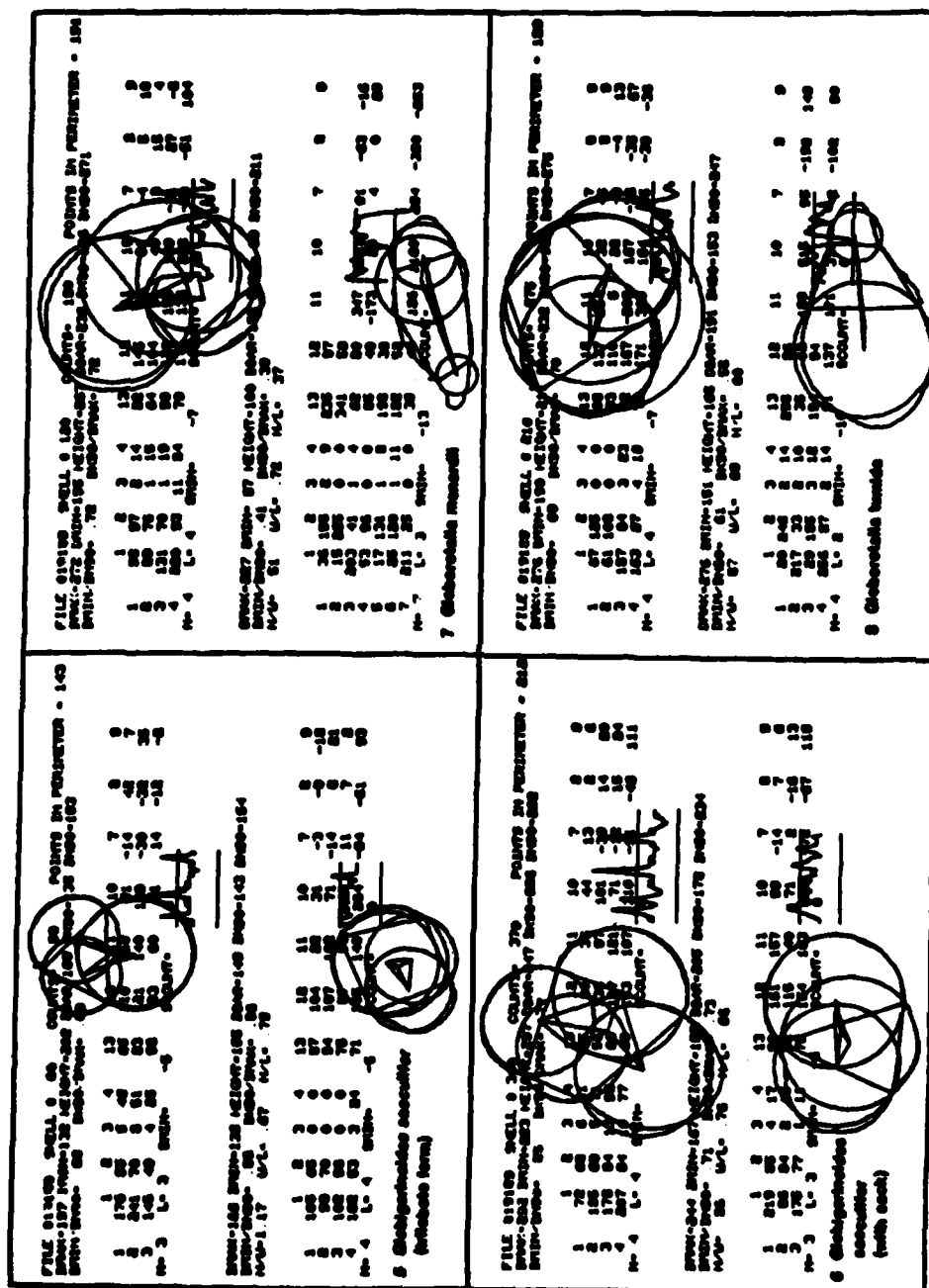


Fig A1.3. Sample output from Sam for "species" 9-13.

10

11

APPENDIX 2

LISTING OF IDENTIFICATION PROGRAM

What follows is a listing of the program which classifies shells on the basis of "traits" passed from the analysis program. The "traits" are essentially the numbers shown in Figs A1.1-A1.3 in Appendix 1. The identification program is written in Algol. Comments in the text of the program explain the logic.

[illegible]

THIS PAGE IS BEST QUALITY PRACTICABLE
FROM COPY FURNISHED TO DDO

THIS PAGE IS OF POOR QUALITY PRACTICABLE FROM COPY FURNISHED TO DDG

```

840 0000 DRITE(11.8*K+1,BLOCK13,IU*8,IU),DISKERROR,
841 0000 END,
842 0000 & NOW OPEN NEW FILE
843 0000 GETUD(066,J),
844 0000 J=J+1, STOWD(066,J),
845 0000 CLOSE(11,IU), DISKERROR,
846 0000 OPEN(11,J,IU,1),DISKERROR,
847 0000 K=30-IU,
848 0000 DRITE(11.1,BLOCKIU*16+13.8*K,IU),DISKERROR,
849 0000 IU=0,
850 0000 END,
851 0000 END,
852 0000 & FILE 11 IS THE HISTORICAL FILE FOR EACH SHELL. THE
853 0000 & PROGRAM RECORDS.
854 0000 & RUN NUMBER.(CUP NUMBER)*100+IDASH.DMAX.DMIN.
855 0000 & HEIGHT.DBAR.DNS0.DX90.ACTUAL SPECIES ID.
856 0000 & SAM'S SPECIES ID. AND SEVERAL PARAMETERS
857 0000 & DEPENDING ON SAM'S SPECIES ID.
858 0000 STOWD(075,K), STOWD(074,IU),
859 0000 END OF INS LOOP,
860 0000 GETUD(063,I), IF I=0 THEN BEGIN
861 0000 RESET(7.1), ALINK(011300), END ELSE EXEC(9.7200),
862 0000 END OF NOT COPYING BLOCK
863 0000 &
864 0000 & FOLLOWING IS WHAT HAPPENS INSTEAD OF PROGRAM
865 0000 & EXECUTION WHEN WORD 060 IS 00 -- NAMELY, PROGRAM
866 0000 & FILES AN IMAGE OF SELF ON DISK FILE 10000
867 0000 ELSE BEGIN
868 0000 OPEN(7.10000,IU,1),DISKERROR,
869 0000 COPY(023000),
870 0000 CLOSE(7,IU),DISKERROR,
871 0000 EXEC(9.2),
872 0000 END OF COPYING BLOCK,
873 0000 ENDS

```